

CZECH TECHNICAL UNIVERSITY IN PRAGUE
Faculty of Mechanical Engineering
DEPARTMENT OF ENERGY ENGINEERING

Dissertation Thesis

Advanced Coatings of Nuclear Fuel Cladding

Jan Škarohlíd

Doctoral Study Program: *Mechanical Engineering*

Study Field: *Power Engineering*

Supervisor: *Doc. Ing. Radek Škoda, Ph.D.*

Supervisor Specialist: *Doc. Ing. Irena Kratochvílová, Ph.D.*

Prague

September, 2018

ČESKÉ VYSOKÉ UČENÍ TECHNICKÉ V PRAZE
Fakulta strojní
Ústav energetiky

Disertační práce

Pokročilé povlaky jaderného paliva

Jan Škarohlíd

Doktorský studijní program: *Strojní inženýrství*

Studijní obor: *Energetické stroje a zařízení*

Školitel: *Doc. Ing. Radek Škoda, Ph.D.*

Školitel specialista: *Doc. Ing. Irena Kratochvílová, Ph.D.*

Praha

září, 2018

Abstract

In this work, a new anticorrosion strategy for Zr nuclear fuel cladding tubes was presented and explained. We used Zr alloy surface coating, which could be beneficial at temperatures above 800 °C (accident tolerant fuel) and at operational conditions at lower temperatures 300 – 400 °C (prolonging fuel operation lifetime). Specially, this work deals with a protection of zirconium (Zr) nuclear fuel cladding material against corrosion in water-cooled nuclear reactors by coating of polycrystalline diamond (PCD) or chromium-aluminum-silicon nitrate (CrAlSiN) layers. It was shown that Zr alloy surfaces can be effectively protected against oxygen and hydrogen uptake at both accident and working temperatures in water-cooled nuclear reactor environments by coating the Zr surface by PCD layer or CrAlSiN each in specific way and for specific purpose. PCD layer consists of two different carbon phases: diamond and sp^2 hybridized carbon. Protective PCD layer is thin 300 – 700 nm and its best application is to reduce Zr nuclear fuel cladding tubes corrosion at operating temperature (typically by 40 %). and thus prolong the lifetime of nuclear cladding and consequently enhance nuclear fuel burn-up. In addition to the fact that PCD layers prevent the surface of Zr alloys from direct interaction with hot water/steam, carbon released from the PCD film enters and changes the physical properties of the underlying Zr surface. On the contrary, CrAlSiN coatings is 2 – 4,5 μm thick one phase layer. CrAlSiN coating serves as a full barrier against oxygen diffusion mainly at high temperature steam around 1000 °C, strongly depending on absence of mechanical defects. Next step of our work will be combinations of both specific anticorrosion strategies of Zr alloy cladding tubes coating: changing of conditions for corrosion process (PCD coating) and preventing physical contact of Zr cladding tubes surface with hot steam/water specially at accident temperatures (CrAlSiN coating).

To summarize, both investigated materials for Zr cladding tubes protective coating have different strategy and protect Zr alloy under different conditions. PCD layer consists of two different carbon phases: diamond and sp^2 hybridized carbon. Protective PCD layer is thin 300 – 700 nm and its best effect is to reduce Zr surface cladding tubes corrosion at nuclear reactor operating temperature (typically by 40%) and thus prolong the lifetime of nuclear cladding and consequently enhance nuclear fuel burn-up. In addition to the fact that PCD layers prevent the surface of Zr alloys cladding tubes from direct interaction with hot water, carbon released from the PCD film enters and changes the physical properties of the underlying Zr surface. On the contrary, CrAlSiN coatings is 2 – 4,5 μm thick homogeneous single phase layer. CrAlSiN coating serves as full barrier against oxygen diffusion mainly at high temperature steam around 1000°C, strongly depending on absence of mechanical defects. Also, oxidation of the primary chromium, aluminium and silicon nitrides leads to creation of highly stable and high temperature resistant alumina and chromium layers.

Abstrakt

V této práci byla představena a vysvětlena nová antikorozní strategie pro zirkoniové (Zr) trubky pokrytí jaderného paliva. Použili jsme povlak ze slitin Zr, který by mohl být přínosný při teplotách nad 800 °C (Accident Tolerant Fuel) a při provozních podmínkách při nižších teplotách 300 – 400 °C (prodloužení životnosti paliva). Tato práce se zabývá především ochranou zirkoniového (Zr) pokrytí jaderného paliva proti korozi ve vodou chlazených jaderných reaktorech povlaky polykrystalického diamantu (PCD) nebo směsného nitridu chromu, hliníku a křemíku (CrAlSiN). Bylo prokázáno, že povrchy slitin Zr mohou být účinně chráněny proti oxidaci při havarijních a pracovních teplotách ve vodou chlazených jaderných reaktorech tím, že ochrání povrch zirkonia vrstvou PCD nebo CrAlSiN každým specifickým způsobem a pro konkrétní účel. PCD vrstva se skládá ze dvou různých uhlíkových fází: diamant a sp^2 hybridizovaný uhlík. Ochranná vrstva PCD je tlustá 300 – 700 nm a její nejlepší využití je snížení koroze Zr slitiny při provozní teplotě (typicky o 40%) čímž prodlužuje životnost pokrytí a následně umožňuje vyšší vyhoření jaderného paliva. Kromě toho, že vrstvy PCD zabraňují přímému kontaktu Zr slitin s horkou vodou resp. párou, uhlík uvolněný z PCD filmu vstupuje a mění fyzikální vlastnosti podkladového povrchu Zr slitiny. Naopak, povlaky CrAlSiN mají tloušťku 2 až 4,5 μm . Povlak CrAlSiN slouží jako plná bariéra proti difúzi kyslíku hlavně při vysoké teplotě páry kolem 1000 °C, silně v závislosti na nepřítomnosti mechanických defektů. Dalším krokem naší práce bude kombinace obou specifických antikorozních strategií pokovování plášťů ze slitin Zr: změna podmínek pro proces koroze (PCD povlak) a zabránění fyzickému kontaktu povrchu Zr plášťových trubek s horkou párou / vodou zvláště při nehodových teplotách (CrAlSiN povlak).

Shrnuto, oba zkoumané materiály pro ochranný povlak Zr plášťových plášťů mají odlišnou strategii a chrání slitinu Zr za různých podmínek. PCD vrstva se skládá ze dvou různých uhlíkových fází: diamant a sp^2 hybridizovaný uhlík. Ochranná vrstva PCD je tenká 300 - 700 nm a její nejlepší účinek je snížit korozi povrchu Zr plášťových plášťů při provozní teplotě jaderného reaktoru (typicky o 40%) a tím prodloužit teoretickou životnost pokrytí. Navíc k tomu, že vrstvy PCD zabraňují kontaktu Zr slitiny s vodou, uhlík uvolněný z PCD filmu vstupuje a mění fyzikální vlastnosti podkladové slitiny. Naopak, povlaky CrAlSiN jsou homogenní jednofázové vrstvy o tloušťce 2 - 4,5 μm . Povlak CrAlSiN slouží jako plná bariéra proti difúzi kyslíku hlavně při vysoké teplotě páry kolem 1000 °C, silně v závislosti na nepřítomnosti mechanických defektů. Také oxidace primárních chromových, hliníkových a křemíkových nitridů vede k tvorbě vysoce stabilních a vysoce teplotně odolných oxidů hliníku a chromu.

Declaration

I declare that I carried out this doctoral thesis independently, and only with the cited sources, literature and other professional sources.

I hereby declare that I have prepared my dissertation work independently using professional literature, documents, on the basis of consultations and under the guidance of my supervisor Dr. Radek Škoda

In....., date

signature

Acknowledgements

Given the specific scope of this work, its completion wouldn't be possible without the generous help, cooperation and support of a number of people. First and foremost, I would like to thank my supervisor Dr. Škoda and my specialist supervisor Dr. Kratochvílová for their exemplary leadership, involvement, inspiration and increasing pressure to finish this work, which were essential for achieving results presented in this work.

My sincere thanks also goes to Karlsruhe Institute of Technology namely to Dr. Steinbrück and Dr. Grosse and other colleagues from "QUENCH" team (IAM-AWP).

I would like to express deep gratitude to Dr. František Fendrych, Dr. Petr Ashcheulov and Andrew Taylor from the Institute of Physics Czech Academy of Sciences whose expertise, cooperation and facilities were crucial for big part of this work.

Last but not the least, I would like to thank my family: my parents, my wife Hana and my son Victor.

Index

1 Introduction.....	6
2 Zirconium alloys in nuclear reactors.....	7
2.1 Zirconium cladding and structural components in nuclear reactors.....	7
2.2 Zirconium alloy surface corrosion.....	11
2.3 Kinetics of zirconium alloy oxidation.....	13
Diffusion and Parabolic Law of Oxide Growth.....	14
Oxidation kinetics model.....	14
Law of linear growth of oxide.....	15
Hydrogen Uptake.....	15
3 Protective coatings on Zr cladding tubes.....	18
4 Thesis tasks and goals.....	20
5 Instrumentation and methods.....	21
5.1 Coating preparation.....	21
PELAM CVD – preparation of PCD coatings.....	21
Physical Vapor Deposition (PVD) – preparation of CrAlSiN coatings.....	22
5.2 Coating preparation.....	22
Long-Term Exposure in Reactor Operation Conditions.....	22
High-Temp exposure.....	22
Thermogravimetry.....	22
Off-gas analysis.....	23
Ion Beam Irradiation.....	23
5.3 Coated Zr cladding tests after steam / water exposures.....	24
Optical microscopy of the metallographic cross sections of samples.....	24
Scanning Electron Microscopy (SEM) and Energy Dispersive X-Ray Spectroscopy (EDS).....	24
Raman spectroscopy.....	24
Inert gas fusion (IGF) – Hydrogen concentration measurements.....	24
X-ray Photoelectron Spectroscopy (XPS) analysis.....	25
Secondary ion mass spectrometry (SIMS).....	25
XPS, UPS and work function analysis with a NanoESCA system.....	25
6 Results and discussion.....	27
6.1 Protective PCD coating on Zr alloy.....	27
PCD Long-Term Exposure in Reactor Operation Conditions.....	27
PCD Ion Beam Irradiation.....	28
PCD Thermogravimetry and hydrogen production measurement.....	29
PCD Carbon monoxide and carbon dioxide measurement.....	32
PCD High-temperature exposures.....	33
PCD Optical appearance of the samples.....	33
PCD Raman spectroscopy.....	33
PCD Optical microscopy.....	35
PCD Hydrogen concentration in Zr metal measured by IGF.....	37
PCD SEM observations.....	38
PCD X-ray photoelectron spectroscopy.....	38

PCD Secondary ion mass spectrometry (SIMS).....	39
PCD Capacitance measurements.....	40
6.2 Protective coatings based on Cr – Al – Si nitrides.....	40
CrAlSiN coating preparation.....	40
CrAlSiN Long-Term Exposure in Reactor Operation Conditions.....	40
CrAlSiN Thermogravimetry and hydrogen production measurement.....	41
CrAlSiN High-temperature exposures.....	42
CrAlSiN Optical microscopy.....	43
CrAlSiN Hydrogen concentration in Zr metal measured by IGF.....	46
CrAlSiN EDS and SEM observations.....	47
7 Published papers.....	52
7.1 Nanosized polycrystalline diamond cladding for surface protection of zirconium nuclear fuel tubes.....	52
7.2 Thin polycrystalline diamond films protecting zirconium alloys surfaces: From technology to layer analysis and application in nuclear facilities.....	52
7.3 High temperature oxidation of polycrystalline diamond coated zirconium alloys.....	53
7.4 Nanocrystalline diamond protects Zr cladding surface against oxygen and hydrogen uptake: Nuclear fuel durability enhancement.....	53
8 Comments and Outlook.....	55
9 Conclusions.....	57
10 References.....	60
10.1 Autor references.....	60
10.2 Other references.....	60
11 Supplementary.....	63
PUBLISHED PAPERS.....	66

1 Introduction

Currently, zirconium (Zr) alloys are utilized in all commercially operated power producing light-water (PWR, BWR and VVER) and heavy-water (CANDU) nuclear reactors [1], [2]. In particular, Zr alloys are used as a construction material for nuclear fuel cladding rods and for other structural elements in fuel assemblies and the core internals of nuclear reactors, such as spacer grids or complete pressure channels [3]. The main reason for their use is the low parasitic absorption of neutrons and high resistance against radiation damage. Zr alloys also possess very good mechanical properties, high melting temperature and chemical stability [1], which are maintained during long-term exposure to the extreme conditions in nuclear reactors, i.e. high neutron flux and high pressures.

Zirconium alloys are its use is accompanied with several negative aspects and processes as Pellet Cladding Interaction (PCI), Irradiation Assisted Stress Corrosion Cracking (IASCC), Hydrogen Uptake (HU) leading to Delayed Hydride Cracking (DHC) and High-temperature Oxidation (HTO) [2], [4], [5]. High temperature oxidation of zirconium alloy surface should be avoided, i.e. to limit the reaction between the surface of the alloy and the steam. High-temperature oxidation is strongly exothermic reaction between zirconium and water, which occurs at temperatures above 800 °C¹ [6]. Hydrogen and considerable amount of heat is released during this reaction. Degradation of the cladding tube will lead to the contamination of primary circuit with radiotoxic isotopes of nuclear fuel, fission products and transuranics, and potential radioactivity release. Arisen hydrogen, which as a combustible gas, impose a serious risk in the case of a severe accident conditions. Arisen hydrogen could explode and caused several damage of reactor vessel, primary circuit, containment, and reactor building [7]. Released heat will strongly contribute to the potential core melting. All these we can saw during Fukushima-Daichi accident in 2011 [8], [A1].

HTO is a surface related effect – the chemical reactions or the physical interactions are initiated at the surface of the Zr alloy. A solution to the problem, is to cover the surface with a thin layer of a protective substance. Actual research effort heads for development of technologies, which prevent or diminish high temperature oxidation, by using protective coating layer or by using completely different material [9], [10], [11].

As nuclear accidents with core temperatures higher than 800 °C are highly unlikely, the potential coating should be not only safety benefit but economical and plant operational benefit too. So, aim of this work is not only look for Zr alloy surface modifications, which could be beneficial at temperatures above 800 °C (Accident Tolerant Fuel – ATF), but also on materials and their performance at operational conditions at lower temperatures 300 – 400 °C [12], [13]. Specially, this work deals with a protection of zirconium (Zr) nuclear fuel cladding material against corrosion in water-cooled nuclear reactors by coating of polycrystalline diamond (PCD) or chromium-aluminum-silicon nitrate layers (CrAlSiN). It is shown that Zr alloy surfaces can be effectively protected against oxygen and hydrogen uptake at both accident and operational temperatures in

1 Temperature value is different in different references, as the transition temperature depends on several factors.

water-cooled nuclear reactor environments by coating the Zr surface by PCD layer or aluminum-silicon nitrate each in specific way and for specific purpose. Several types of measurements were performed to describe and properly interpret high temperature oxidation of coated Zr nuclear fuel cladding material: online thermogravimetry (TG) (measurement of the mass changes caused by mass increase during oxidation), mass spectrometry analysis of the off-gas released during high-temperature steam exposition, X-ray photoelectron spectroscopy (XRD), Raman spectroscopy, scanning electron microscopy (SEM), secondary ion mass spectrometry (SIMS), capacitance measurements and XPS [A2].

2 Zirconium alloys in nuclear reactors

2.1 Zirconium cladding and structural components in nuclear reactors

Zirconium alloys are present in both most common types of LWRs (Light Water Reactors): BWR (Boiling Water Reactor), PWR (Pressurized Water Reactor) and VVER (Vodo-vodnyj energetičeskij reaktor)². Zirconium alloys are construction material for cladding tubes and structural components fuel assemblies (Fig. 1) and inner parts of Reactor Pressure Vessel (RPV).

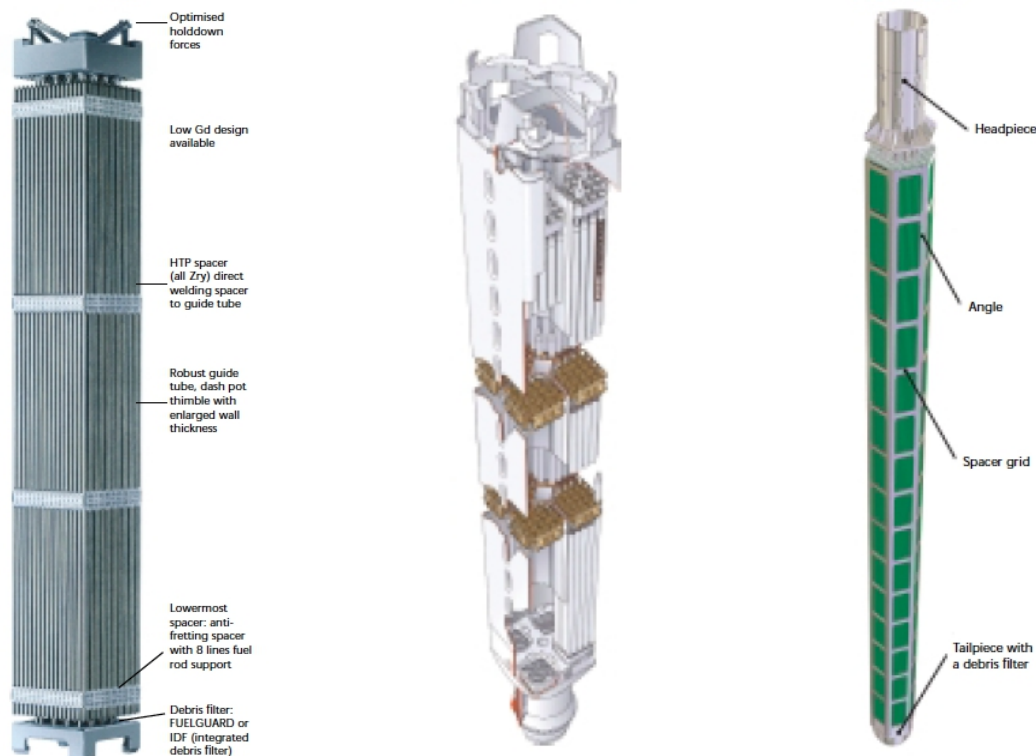


Fig. 1: Fuel Assemblies for PWR (Framatome HTP), BWR (Westinghouse Sweden SVEA-96 Optima 2) and VVER (Mashinostroitelny zavod 1000A) [3].

2 Zirconium alloys are also used in other types reactors, but are not mentioned and considered in this work as 1) amount of zirconium is not significant for LOCA (fuel channels in RBMK) or 2) corrosion conditions and construction are notably different from most common LWRs (CANDU reactors).

Five mechanism of cladding failure has been described and corresponding criteria has been created (Table 1).

Table 1: Cladding failure criteria [14]

MECHANISM	FAILURE CRITERION ADOPTED
Departure from Nucleate Boiling (DNB)	Ratio of average heat flux necessary to cause DNB to the heat flux predicted to exist in the fuel rod less then or equal to 1,3
High cladding stresses	Effective stress in the cladding greater than or equal to cladding material yield stress
Fuel melting	Fuel rating greater than or equal to 59 kW.m^{-1} , fuel rating at which fuel melting is calculated to start, using conservative calculation route
Pellet-Cladding Interaction (PCI)	Calculated cladding hoop stress exceeds specified values
Fast power shocks	Radial average peak fuel enthalpy greater than or equal to 586 J.g^{-1}

Additionally fuel design should include such items as maximum fuel and cladding temperatures, clad-to-fuel gap conductance as a function of burn-up and operating conditions, and fuel cladding integrity criteria.

Hence fuel cladding is one on most important barriers keeping radioactive and radiotoxic material (plutonium, fission products,...) separated from cooling water is necessary to operate not only in conditions that occur regularly in normal operation (Cat. 1. with frequency $\sim 10^3$) and during faults that are expected during the life of the power plant, and which requires safety response (Cat 2. with frequency ~ 1). Even more, fuel cladding has to withstand conditions caused by faults which are not expected during a life of a particular plant (Cat 3. with occurrence $\sim 10^{-2}$) and as the design considered conditions are taken improbable events, which are not expected to occur in nuclear industry (Cat. 4. with probability $\sim 10^{-4}$). Design Based Accident (DBA) which is defined as:

- A double-ended rupture of one cold leg of primary coolant loop (for PWR)
- A double-ended rupture of recirculation loop (for BWR)

More details for DBA assumptions are in Supplementary 2. No fuel failure is expected during DBA. Following criteria has to be kept by design to prevent fuel failure during large LOCA DBA [14]:

1. Peak Cladding Temperature – Maximal cladding temperature can not overreach $1204 \text{ }^\circ\text{C}$.
2. Maximum Cladding Oxidation (ECR17) – Maximal level of oxidation can not overreach 17% of cladding thickness.
3. Maximum Hydrogen Generation – The total amount of hydrogen generated by the chemical reaction between the coating and the water or water vapor must not exceed 0.01 times the theoretical amount that would arise if all the coverage of the nuclear fuel had reacted
4. Cool-able Geometry – Changes in core geometry enabling core cooling

3 For more details about Event Categories see Supplementary 3

5. Long-Term Cooling – After successful ECCS intervention, the core temperature must be maintained at an acceptably low temperature and the decay heat must be discharged over the lifetime of long-lived radioisotopes in core.

Typical temperatures for cladding and fuel LOCA cladding temperature transient is on Fig. 2.

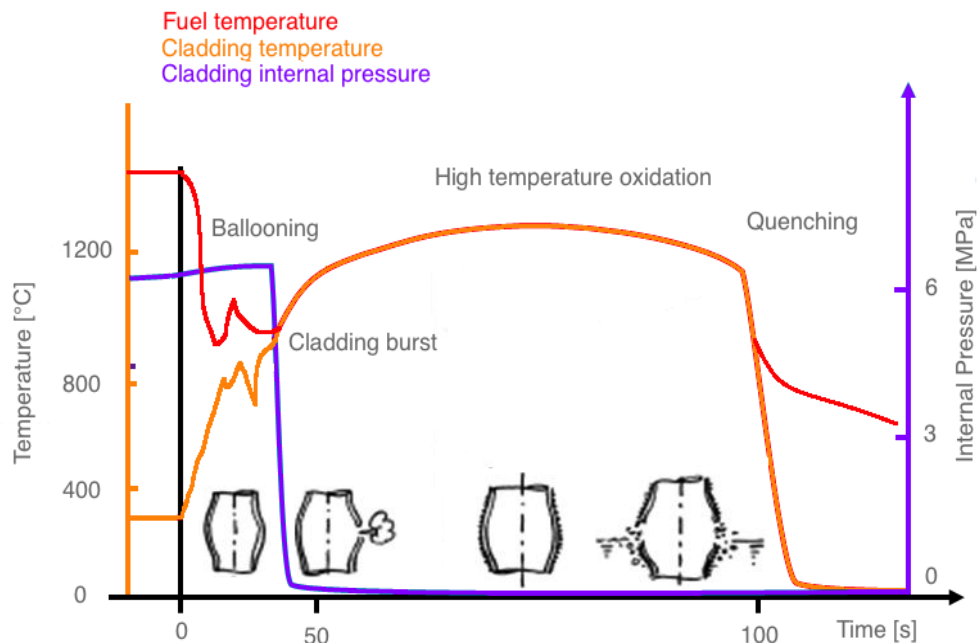


Fig. 2: Typical LOCA temperature transient

Typical LOCA transient can be described in four stages [14].

1. Blown down – depressurization and emptying of primary circuit, caused not only by outflow through the rupture, but also by boil-off caused by overheated reactor core. First temperature peak is achieved. Core cooling is lost, emergency core cooling is provided by passive ECCS – hydroaccumulators. Start of active ECCS. Reversal of upward coolant flow-rate to downward coolant flow-rate. These effects leads to core uncover. In case of ECCS failure heating of the uncovered core continues leading to Severe Accident (SA), where oxidation of cladding releases additional heat and produces hydrogen. Fuel cladding changes it's geometry (so called ballooning) and loses it's integrity. Finally core collapses and falls down, creating melted corium⁴ pool at the reactor bottom lid.
2. Refill – Filling of lower plenum of reactor pressure vessel with cooling water. Downcomer is filled with water, core itself is cooled only by steam. Cladd ballooning is possible with burst opening. Leading to obstacles in coolant flow and partial release of FP. Core is heating up.
3. Reflood – reflooding of reactor's core and quenching of fuel cladding. This stage is most demanding for overheated fuel cladding, while oxidation kinetics is the highest, releasing

⁴ Corrium is term form melted zirconium, steel, uranium, control rod materials (boron, gadolinium, etc...) and their oxides together with melted concrete (after pressure vessel failure)

ten times more heat⁵ and hydrogen. According new rules – steam flow of 1 gram of steam per rod per second is sufficient to cool the core adequately and partial core reflooding is ineligible. Possible release of FP from damaged fuel rods.

4. Long term reactor cooling, residual heat removal. RPV is depressurized (in case of BWR is depressurization triggered automatically during initial accident phase). Water circulation is maintained by RHRS (Residual Heat Removal System), operation of RHRS requires electricity and additional water, which has to be provided off site.

Zirconium alloys undoubtedly the most important alloy used in nuclear industry. Hence having very low neutron capture, while keeping optimal engineering properties and chemical resistance, are zirconium alloys used for almost all reactor core internals. Although zirconium alloys are used in nuclear industry since it's beginning are there still areas, which are not described and understood properly (hydride orientation in atmospheres with high hydrogen concentration, high temperature oxidation in air,...). Several zirconium alloys was developed and slightly which differ in alloying elements concentration. We can distinguish between sponge based alloys⁶ (eg. Zr1Nb by Russian TVEL) and non sponge based alloys⁷ (eg. Zirlo by Westinghouse, M5 by Areva). Sponge based alloys contain high concentration of niobium, non sponge alloys are niobium free (except M5, where alloying niobium is add artificially. Composition of most common zirconium alloys in Table 2. In this work Zirlo and Zircaloy-2 was used, as they were kindly provided by Westinghouse.

Table 2: Composition of the Zr alloys of industrial use (concentration in wt% or ppm) [1]

Alloy	Alloying Element						
	Sn	Nb	Fe	Cr	Ni	O	S
Zircaloy-2	1,2 – 1,5		0,07 – 0,2	0,1	0,05	0,12	
Zircaloy-4	1,2 – 1,7		0,18 – 0,24	0,1		0,1 – 0,16	
M5		0,8 – 0,12	<500 ppm				10 – 35 ppm
E110		1	100 ppm			0,05 – 0,07	
Zirlo	1	1	0,1			0,09 – 0,12	

Below 865 °C, pure Zr has an hcp (hexagonal close packing) structure, with a c/a ratio of 1,593. The lattice parameters are a. 0,323 nm and c. 0,515nm (Zr α phase). At 865 °C, Zr undergoes an allotropic transformation from the low temperature hcp α phase to the high temperature bcc (body centered cubic) β phase. On cooling, the transformation is usually bainitic. The melting temperature of pure Zr is 1860 °C [1].

5 Paradoxically adding more water could increase core temperature.

6 Reduction of the ZrO₂ obtained by the MIBK process is often performed by electrolysis. It is realized with the mixed salt K₂ZrF₆ dissolved in NaCl or KCl at 850 °C under inert gas, with stainless steel cathode on which Zr is deposited, and chlorine evolution at the graphite anode.

7 The Kroll process, the Zr metal is obtained by the reduction of ZrCl₄ in gaseous form by liquid magnesium, at about 850 °C in an oxygen-free environment.

2.2 Zirconium alloy surface corrosion

Large quantities of heat could be released during Zr reaction with hot steam. Finally, the degradation of the fuel cladding, may lead to its failure and subsequent leakage of highly radioactive fission products from the nuclear fuel into the primary circuit. In the case of flooding of the superheated active zone with water, which is one of the functions of the safety systems in nuclear reactors, quenching of a zirconium alloy occurs. Production of hydrogen in this case is ten times higher compared to when cladding reacts only with steam. Temperature is the most important factor affecting high-temperature corrosion – reaction kinetics increases with increasing temperature. Other influencing factors are: exposure time of heated zirconium alloy in air, the initial oxidation of the zirconium alloy and the presence of other materials in the melting core [15], [1].

Oxidation of Zr alloys have been under study for a long period of time and a fairly good understanding of the phenomenology of the processes for high-temperature conditions in oxidizing media: hydrogen, vapor and liquid, has been achieved. Oxidation process can be subdivided into three stages [15]:

1. At the initial stage the oxide layer is formed rather quickly under normal conditions in the air (i.e. the initial state of Zr products) and consists of a small number of monoatomic layers. These layers are unordered and consist of non-stoichiometric Zr oxide.

2. The next stage of oxidation is pre-transition stage which takes place at temperatures from 200 °C and above. At this stage oxide layer growth takes place by cubic or parabolic laws up to oxide thickness of 2-3 μm . The inner region of the layer is non-stoichiometric, the outer region is close to stoichiometric composition. Further on with the growth of an oxide layer, an increase in mechanical stresses at the metal/oxide boundary takes place and crack formation occurs at certain thicknesses.

3. With further growth of the oxide layer, over 2-3 μm , kinetics of growth changes for quasilinear dependence of oxidation. This stage of oxide layer growth is characterized by a large number of defects in the oxide layer such as cracks and pores.

The basic physical processes occurring in Zr alloy, which affect corrosion kinetics are as follows: transport of atoms of oxygen, hydrogen, alloying elements as well as evolution of inclusions of the secondary phases. The variation of spatial distribution of oxygen concentration versus time in metal affects the rate of growth of oxide layers. Evolution of the distribution of oxygen concentration in the metal also affects coefficients of transport of hydrogen and dissolved mixture atoms in metal. Therefore, alongside diffusion, thermal and pressure diffusion (in temperature and pressure gradients) processes and processes of atom drift in chemical potential gradients can play an important role [1], [16].

Metal/oxide interface can critically affect the rate of regimes of corrosion of Zr alloys. This influence is related to a series of physical effects.

Firstly, the metal/oxide boundary is a contact between metal and semiconductor. As a rule, the

work function of electron emission from metal does not coincide with the work function of emission from a semiconductor. For establishing a balance between a metal and a semiconductor there should not be an electrochemical potential difference, i.e. Fermi levels should coincide in semiconductor and metal. If there is no contact, electrochemical potentials of metals and semiconductors are different than at the first moment after the contact diffusion electrical current will flow through the boundary. Flowing will continue until such a difference of charges between the metal and semiconductor is established and such an electric field is created so that further current flow is ceased [A2]. Schemes of creation of an electrochemical balance under contact between metal and semiconductors of n-type and p-type are shown in Fig. 3 and Fig. 4.

In the area of contact between metal and oxide, potential difference, caused by redistribution of charges, which is equal to difference of chemical potentials of metal and semiconductor, occurs.

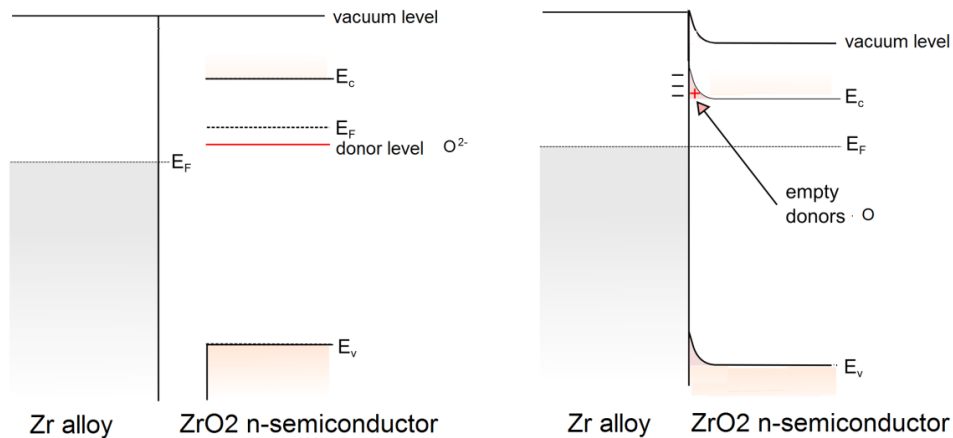


Fig. 3: Band structure of a metal (Zr alloy) and n-type semiconductor (ZrO₂) interface before (left, A) and after metal and semiconductor connection (right) [A2].

The created electric field can markedly affect ion transport (of oxygen, hydrogen and impurity atoms) through the oxide/metal interface. It should be noted that the presence of impurity atoms in the oxide field affect not only the type of conduction – electronic or hole – but also the difference in chemical potentials and distribution of the electric field in close contact to the oxide layer.

Secondly, there is a difference in specific volumes per Zr atom in oxide and metal. Therefore, the crystal lattice of the metal is subjected to the effects of tensile stresses. The highest tensile stresses arise near the oxide/metal contact. The oxide layer, in its turn, is subjected by the action of compression stresses and with sufficient values of stress, a transformation of the crystal lattice of the oxide (from monoclinic to tetragonal) is observed. It is supposed that centers of nucleation of the tetragonal phase are inclusions of intermetallides and the increase in mechanical stresses, which takes place near to them. Thirdly, accumulation of hydrogen coming through the oxide layer occurs because of the pressure diffusion effect on the oxide/metal interface. With rather high hydrogen fluxes, the formation of Zr hydrides at the interface is possible. Such a process can be one of the physical mechanisms, which are responsible for appearance of nodular corrosion

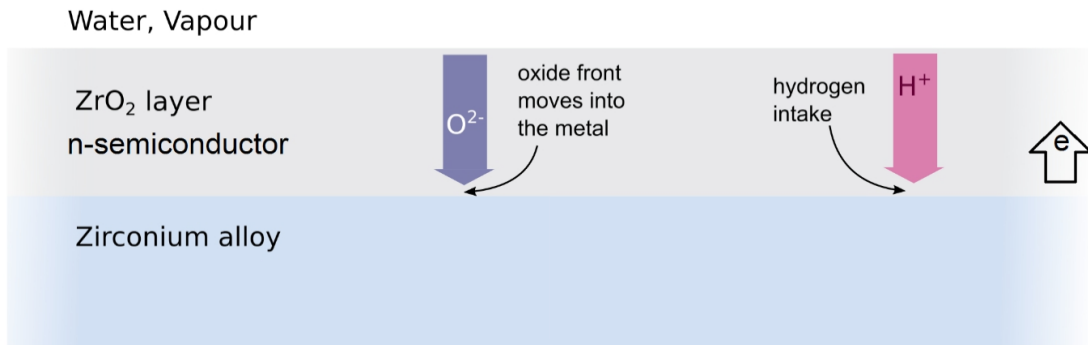


Fig. 4: Schematic showing the transport of H and O from the surface and into the bulk of Zr alloy during hot water/steam exposure for uncoated ZIRLO, which is mainly chemically composed of ZrO_2 , implying a large uptake of oxygen forming an n-type semiconductor [A2].

2.3 Kinetics of zirconium alloy oxidation

The kinetics of oxidation of most common metals and alloys can be described by three laws of growth of oxide layers: parabolic, linear and logarithmic. The amount of oxygen reacted in surface oxide formation could be measured by weight gain per unit area. The weight gain during oxidation is directly proportional to the oxide thickness.

Generally five types of oxidation kinetics are known [17]:

1. The oxidation control mechanism is the creeping of cations from metal to oxide – Logarithmic law;
2. Oxidation is controlled by the passage of electrons through oxide layer – Logarithmic law;
3. Oxidation causes ion diffusion by strong oxide layer – Parabolic law;
4. Strong oxide layers crack and peel off; the layers contain obstacles that hamper diffusion (eg grain roughing during grain boundary diffusion) – Cubic law;
5. Metal is in direct contact with the atmosphere (steam) – Linear law.

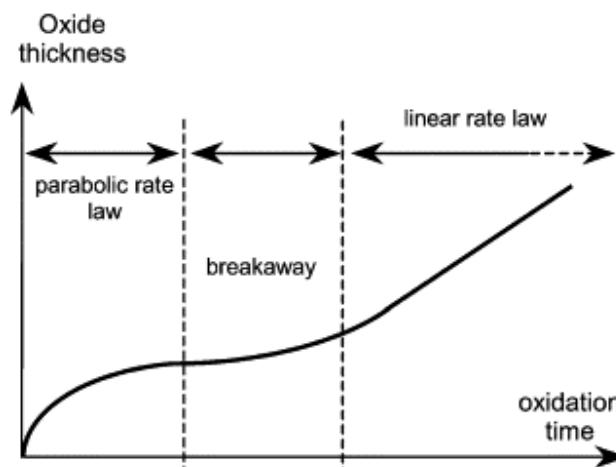


Fig. 5: Oxidation kinetics for zirconium [15]

Parabolic and linear growth of oxide are typical for zirconium oxidation (see Fig. 5).

Diffusion and Parabolic Law of Oxide Growth

The law of parabolic growth of the oxide layer is the standard for high temperature oxidation kinetics analysis in which the reaction kinetics are controlled by diffusion across relatively thick oxide layers. Diffusion is a process in which atoms or ions are moved to a distance between the chemical potential and the inter-atomic distance due to the equalization of the chemical potential difference [15]. The parabolic mechanism increases the penetration of ions (for example, oxygen anions) into a coherent and perfectly sticky oxide layer. The ionic concentration of the reactants at the oxide / metal and oxide / water (vapor) interfaces and the across the oxide coating can be considered constant at steady state.

The diffusion coefficient (Table 3) is thus directly proportional to the diffusivity velocity of the control type ion of the surface, electrically conductive, oxide coating. The mass increment, is directly proportional to the thickness of the coating.

The amount of oxygen that reacts with fuel cladding as a whole does not convert to oxide, but partly produces the basement metal of the cladding wall. The measured mass gain thus represents not only the increase in oxide (ZrO_2) but also the oxygen atoms that have reached the $Zr(O)$ of the parent metal layer [2].

Table 3: Diffusion coefficients for different Zr phases [18]

Material	Diffusion coefficient -correlation	Diffusion coeff. - value at 865 °C
Zr α	$D_{\alpha} = 3,923 e^{\frac{-51,000}{R \cdot T}}$	$D_{\alpha} = 3,9019 \text{ cm}^2 \cdot \text{s}^{-1}$
Zr β	$D_{\beta} = 0,0263 e^{\frac{-28,200}{R \cdot T}}$	$D_{\beta} = 0,026222 \text{ cm}^2 \cdot \text{s}^{-1}$
ZrO_2	$D_{ox} = 0,1387 e^{\frac{-34,680}{R \cdot T}}$	$D_{ox} = 0,13819 \text{ cm}^2 \cdot \text{s}^{-1}$

Diffusion coefficients (D_{α} , D_{β} , D_{ox}) for Zr alpha and beta phases and for Zr oxide in square centimeters per second calculated according [18] correlations, where R is universal gas constant ($R = 1,987 \text{ kcal} \cdot \text{K}^{-1} \cdot \text{mol}^{-1}$) and T is thermodynamic temperature in Kelvins.

Oxidation kinetics model

Several oxidation kinetics model has been developed to predict oxidation rate of zirconium alloy. Weigh gains and ECR, which is one of fuel criterions are calculated. Two main correlations are used: Carthcart-Pawel correlation [18]:

$$w_0 = 0,60183 \cdot t^{0,5} e^{\frac{-19970}{R \cdot T}} \quad [g \cdot cm^{-2}]$$

and Baker-Just correlation [19]:

$$w_0 = 2,0248 \cdot t^{0,5} e^{\frac{-22750}{R \cdot T}} \quad [g \cdot cm^{-2}]$$

where t is oxidation time in seconds, T is thermodynamic temperature in kelvins and R is universal gas constant ($R = 1,987 \text{ kcal.K}^{-1}.\text{mol}^{-1}$).

$$ECR(\text{fraction}) = \frac{2,85 \cdot w_0}{\rho_{Zr} \cdot h_r} = \frac{w}{\rho_{Zr} \cdot h_r}$$

where w is weight per sample area and w_0 is weight gain per surface area both in grams per centimeter squared ρ_{Zr} is density of zirconium ($\rho_{Zr} = 6,50 \text{ g.cm}^{-2}$) and h_r is cladding thickness in centimeters.

$$ECR(\text{fraction}) = \frac{2,85 \cdot w_0 \cdot 2}{\rho_{Zr} \cdot h_r}$$

for both side oxidation [14].

Law of linear growth of oxide

The law of linear oxide growth occurs when the rate of oxide growth controls the oxidation reaction at the oxide / metal interface. Any oxide coatings found on this phase interface can not protect the parent metal. In the early stages of oxidation this phenomenon may occur because the thickness of the oxide coating is not strong enough. With it's growth, there is often a transition to parabolic law. However, in the case of a strong oxidation coating, its thickness may increase with micro-cracking and porosity, reduce the protective function of the oxide and fail the parabolic oxide growth law. After a certain time from the onset of such a reaction, the rate of growth of the oxide coating can be brought closer to linearity. Breakaway oxidation – loss of protective properties of oxide scale through it's mechanical failure [16], [18].

Phase change in zirconium dioxide occurs at temperature 1100 °C. At this temperature zirconium dioxide changes it's tetragonal structure to monoclinic structure, which result in a volume increase [1]. Phase change in zirconium dioxide is one of the most important factors contributing to breakaway transition (and also this is the reason we don't see break-way oxidation transition during steam exposures above 1100 °C). Other main factors are:

- accumulation of compressive stresses in the oxide from imperfect accommodation of the volume expansion during oxide formation,
- porosity formed in the oxide reaches allows an easy access of the coolant to the underlying metal.

After the protective surface oxidation coating breaks on a continuously increasing number of sites, the oxidation rate increases [16], [1]. This phenomenon leads to a rapid embrittlement of fuel cladding due to the absorption of hydrogen through the cracks. Compact oxide coatings prevent this behavior and maintain the toughness of the cladding up to a high degree of oxidation [4].

Hydrogen Uptake

Several sources of hydrogen dissolved in primary circuit coolant has been identified [1]:

- water radiolysis
- reduction of water molecules at the coolant-oxide interface
- residual moisture present inside nuclear fuel / nuclear fuel rods
- hydrogen coming from decay of some fission products

Usually most of the hydrogen atom radicals recombine, creating hydrogen molecules, that are subsequently dissolved in the coolant. Some amount of H radicals ingress the zirconium alloy. Hydrogen can migrate through metallic matrix or react with Zr to form hydrides.

The fraction of the hydrogen that is trapped in the Zr alloy is called the hydrogen pick-up fraction (HPUF). For Zry-2, it is in the range of 30–60%, and for Zry-4 a lower HPUF is observed (15–25%), while the Zr–Nb alloys show the lowest one (4–10%) [1].

Hydrogen solubility in zirconium decreases rapidly with temperature. After cladding cool down precipitates of zirconium hydrides are formed at grain boundaries (at lower hydrogen concentrations) or trans-crystallic (at higher hydrogen concentrations) [20].

High temperature HU involves the ingress of hydrogen into a Zr metal, its migration up the stress and thermal gradients, and concentration of hydrogen in the regions of low temperature or higher tensile stress. When the local concentration exceeds the terminal solid solubility, the hydride phase precipitates (see Fig. 6). A slight increase in temperature would make the hydrides ductile and the mechanical behavior of the claddings returns to normal above 200 °C. [21], [1].

Hydrogen in the cladding is also increases the corrosion rate due and to deteriorates the behavior of the cladding during accident scenarios, such as reactivity-induced accident (RIA), in which brittle hydrides drastically reduce the strain to failure or loss of coolant accident (LOCA), where the cladding that is softened by hydrogen creeps faster and fails at lower temperatures. One of the consequences of hydrogen ingress into Zr is the delayed hydride cracking (DHC) [1].

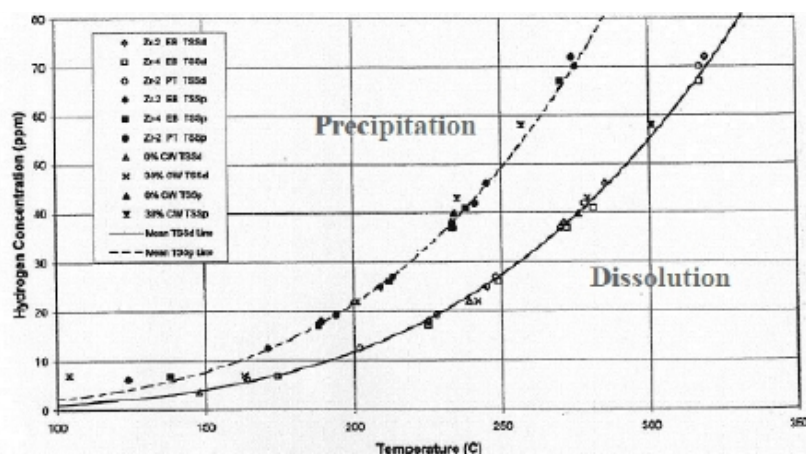


Fig. 6: Solubility of hydrogen in Zircaloy observed using differential scanning calorimetry [22].

The amount of absorbed hydrogen is variable as a function of oxide thickness. In [4] has been

shown that for Zircaloy-2, an initially high hydrogen absorption rate decreases as the oxide thickness increases, but then rises up again after break-way transition linear oxidation kinetics [1].

Sieverts's law is used for prediction of gas solubility in metals:

$$\frac{H}{Zr} = u_s \cdot \sqrt{p_{H_2}}$$

where H/Zr is hydrogen concentration in Zr alloy, p_{H_2} is partial pressure of hydrogen over Zr surface.

3 Protective coatings on Zr cladding tubes

One of the way how to protect Zr nuclear fuel cladding material against corrosion in water-cooled nuclear reactors is coating Zr nuclear fuel cladding surface by polycrystalline diamond and chromium-aluminium-silicon nitrate layers.

Layer thickness is one of the most important technological coating properties. Optimal thickness usually balances between thick robust layer with thickness in tens of micrometers providing adequate protection against oxygen and hydrogen but with higher tendency to cracking and peeling and thin layers (with thickness in hundreds of nanometers), which provides less protection but have much better layer adhesively with low tendency to peeling.

Layer adhesivity is complex phenomena combining several properties and effects. Generally with increase of the coating thickness the difference between Young's modulus is more significant and the coating is less able to compensate hoop stress of the cladding. This effect leads to cracking and peeling of the coating.

Protective coating of zirconium fuel cladding can:

- provide additional time by delaying heat released from zirconium oxidation, this time could allow ECCS to handle the coolant loss in the core sooner, without start of cladding oxidation. Some preliminary analyses [9], [10], [23] shows that even delay in tens of minutes before breakaway oxidation can have significant impact on work of ECCSs.

- avoid zirconium alloy oxidation during core dry out and keep fuel rods intact and without changes in geometry, until low pressure ECCS and RHRS refloods the core.

- minimize size of the burst opening and decrease amount of released FP (Fission Products) to primary circuit [24]

Both this situations are DBA or post DBA with probabilities around $10^{-4} - 10^{-6}$, thus is more than reasonable to look for other advantages, which will not only increase safety but also bring some benefits for vendors, fuel manufacturers and plant operators. These benefits can be:

- decreasing cladding surface oxidation and hydrogen uptake
- lower CRUD formation
- higher fretting resistance⁸
- benefits to heat transfer and neutron moderation / absorption – not necessarily better, but certainly not worse!
- longer lifetime of nuclear cladding and consequently enhancing nuclear fuel burnup.

8 E.g. Titanium nitride coating for fretting resistance [25]

This work deals with a protection of Zr nuclear fuel cladding material against corrosion in water-cooled nuclear reactors by coating of polycrystalline diamond or chromium-aluminum-silicon nitrate layers.

Polycrystalline diamond layer withstands very high temperatures, has excellent thermal conductivity and low chemical reactivity, it does not degrade over time and it has good neutron cross-section. Moreover, polycrystalline diamond layers consisting of crystalline (sp^3) and amorphous (sp^2) carbon phases could have suitable thermal expansion. Polycrystalline diamond coating is a promising possibility for prevention, or reduction of high temperature oxidation of zirconium alloy. Published data [26] of high-temperature stability and oxidation of polycrystalline diamond films and bulk PCD material shows initial oxidation at temperatures above 650 °C. Oxidation was measured in air at elevated temperatures in range 500 – 1300 °C. Neither PCD coatings nor PCD bulk material shows any weight changes in nitrogen atmosphere till 1300 °C [A3] and [A4].

Maximal solubility of aluminium in $Cr_{1-x}Al_xN$ structure is usually limited to the value of 0,6 – 0,8 before the wurtzite-type aluminium nitride is formed. Alloying of CrAlN structure with silicon affects significantly the grain size and mechanical properties. In this quaternary CrAlSiN structure, silicon tends to segregate as amorphous Si_xN_y along the grain boundaries. This effect leads to a nano-composite structure assuring improved oxidation resistance. Oxidation resistance of CrAlSiN coatings was found excellent typically outperforming that of CrAlN [27]. AlCrSiN has excellent thermal stability with cubic nitrides observed up to 1300 °C. Due to the nature of the surface oxide layer, it limits the inward diffusion of oxygen, leading to a lower mass gain during the isothermal test [28],[29].

4 Thesis tasks and goals

In this thesis two materials were selected, applied and investigated as newly introduced anticorrosion coatings for nuclear fuel claddings. Main thesis goals were:

1. Preparation of coated samples, which involved this tasks:
 - x selection of candidate coatings, with perspective properties and suitable methods for coatings deployment and acquisition of suitable substrate material – zirconium alloy
 - x preliminary testing of coated cladding samples (optical appearance after high temperature, adhesion of coatings)
2. Exposure to conditions simulating conditions during LOCA
 - x experimental setup for simulation of LOCA conditions (temperature, pressure)
 - x preparation of exposed coated samples at operation a LOCA conditions.
3. Evaluation of exposed samples using enhanced analytical methods and description of anticorrosive principles.

During first goal substrate materials were kindly provided by Westinghouse Electric (Zry-2 in the beginning of the co-operation and Zirlo in later phases). Several coating were tested, with unsatisfying results. Two best candidates were CrAlSiN and PCD. Special experimental setup was build to test coated samples in steam environment at high temperatures (Fig. 7).



Fig. 7: Experimental setup for high temperature steam exposure in CTU laboratories

In order to get more precise data long-term exposures (simulating reactor operation conditions) were performed in Westinghouse's laboratories in Pittsburgh, as there are no other suitable and available facilities. High-temp exposures and thermogravimetry were realized in Karlsruhe Institute of Technology during short scientific internship.

5 Instrumentation and methods

5.1 Coating preparation

PELAM CVD – preparation of PCD coatings

Samples of fuel cladding tubes (25 mm in length and 10 mm in diameter) and plates (20 mm x 20 mm x 0.1 mm) were immersed (covering the internal and external surfaces of the tubes and both sides of the plates) in a colloidal solution of diamond nanoparticles. The diamond nanoparticles acted as seeds and therefore as nucleation sites for PCD layer growth. Each Zr alloy sample was then coated with a homogeneous PCD layer grown using an MW-LA-PECVD apparatus [30] under the following conditions: a gas mixture of $H_2 + CH_4 + CO_2$, a process pressure of less than 1 mbar, a microwave power of 2×3 kW, and a temperature of approximately 600 °C. Because of the diffuse nature of plasma at low process pressures, the growth of PCD layers was achieved over the entire outer circumference of sample tubes mounted horizontally in the deposition chamber. However, the inner surfaces were only partially coated (Fig. 8).

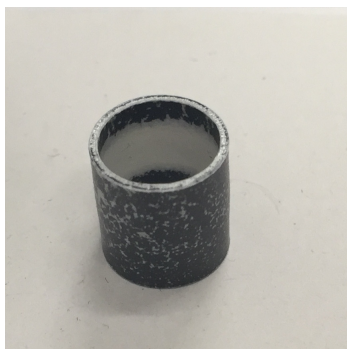


Fig. 8: Partial coating on inner surface is visible on, where different types of oxide developed during oxidation in air-steam environment.

This lack of internal coverage is further discussed above with respect to the interpretation of the results. In the case of sample plates mounted vertically in the deposition chamber, both surfaces were covered with PCD layers. PCD layers of 200-300 nm (labeled as 300 nm), 400-500 nm (labeled as 500 nm) and 600-700 nm (labeled as 700 nm) were produced [A3], [A2]. Notably, the MW-LA-PECVD apparatus could be scaled up such that it would be capable of coating the full lengths of nuclear rods. The temperature of the Zr samples was measured during the diamond deposition by a Williamson Pro 92-38 infrared thermometer capable of measurements in the 450–1000 °C range. The diffuse nature of the plasma in the MW-LA-PECVD system enables control of the substrate temperature, i.e. the substrate is isolated to some extent from heating from the plasma, which enables diamond growth at temperatures compatible with the substrate, e.g. well below the temperature for α phase to β phase transition in Zr.

Since the PELAMWCVD apparatus is not adjusted to deposit PCD coatings inside more complex geometry, as inner surface of small tube can be considered, it was presumed that inner surface of

tubular samples was coated only partly. This was considered during cross-section microscopic evaluations and oxide thickness measurements, where all cross-sections were edges of exposed samples were brushed out and samples were polished at it's middle sections.

Physical Vapor Deposition (PVD) – preparation of CrAlSiN coatings

CrAlSiN was deposited on Zircaloy-2 zirconium alloy using standard commercially available method of Physical Vapor Deposition (PVD). Composition of nitrides in coating is: 36,5 % (Al), 4,8 % (Si), 58,7 (Cr). Thickness of the coating varies between 2 – 4,5 μm . Samples were coated only on outer surface.

5.2 Coating preparation

Long-Term Exposure in Reactor Operation Conditions

To simulate the long-term protective capabilities of both coatings under normal conditions in a nuclear reactor, PCD-coated and reference uncoated samples were subjected to a series of high-temperature autoclave water tests. In accordance with ASTM standard procedures [31], the samples were exposed for 3 and 6 days in hot steam environment (400 °C and 11,6 MPa) and 6, 15, 20, 30, 40, 90, 120, 150, 170 and 195 days in hot water (360 °C, 16 MPa), close to the conditions found in the primary circuit of a PWR. Both exposures were carried out according ASTM [31] methodology and procedures. Exposures in steam were performed at VSCHT laboratories and water exposures at the Westinghouse facilities in Pittsburgh, USA. No additional chemicals were used in both tests.

High-Temp exposure

To simulate the protective capabilities of PCD and CrAlSiN layers against hot steam under accident conditions in a nuclear reactor, coated and reference uncoated samples were subjected to a series of high-temperature steam tests. The samples (tubes or plates) were placed in a silica glass tube reactor, which was placed inside a furnace. The samples introduced in the pre-heated furnace to the required temperature and for the required duration (900, 1000, 1100 °C) in an inert argon atmosphere at atmospheric pressure. (900 °C/1 h, 1000 °C/1h 1100 °C/1 h). All steam exposures were performed isothermally. After hot steam processing, the steam/water flow was switched off after the required time, and the sample was slowly cooled down under an argon atmosphere. Special furnace with silica glass reactor and accessories for steam generation, argon management and measurement was built for this purpose at CTU. For steam exposures at temperatures above 1100 and higher (up to 1400 °C) BOX⁹ furnace at KIT was used. These exposures were coupled with online analysis of the outgoing gas.

Thermogravimetry

Thermogravimetry measurements were performed at elevated temperatures between 900 and 1100 °C. The samples were placed on an alumina holder in a NETZSCH thermobalance (model

⁹ BOX furnace = Boron Oxide oxidation refers to former purpose of used equipment, now used for Zr alloy oxidation research

STA 409). Argon was used as an inert cover gas. Steam exposures were performed isothermally, without any changes in the steam or cover gas flow rates. All high-temperature oxidations were performed under an argon flow rate of 3 liters per hour and a steam flow rate of 3 grams per hour. The overall weight gain (w_g), which is a commonly used quantity to describe the corrosion of a zirconium alloy in a water-steam environment, was determined by measuring the sample's weight before and after oxidation. This weight was normalized with respect to the total exposed surface area of the sample to compensate for different sample sizes. The units used: $mg.dm^{-2}$ or $g.dm^{-2}$ are commonly used in engineering practice and calculations. The sample surface area was calculated from the sample dimensions (length and inner and outer diameters) measured before steam exposure. The equivalent cladding reacted (ECR) (in %) for two-sided oxidation was calculated using the following formula [14]:

$$ECR = \frac{87,8 \cdot w_g}{s}$$

where s is the thickness of the sample and w_g is the weight gain over the entire surface area.

Off-gas analysis

Outgoing gas analysis was performed with a Balzers GAM 300 quadrupole mass spectrometer during high-temperature exposures in BOX furnace and during TG measurements. Concentration of hydrogen (produced by HTO of Zr alloy), unreacted steam and oxygen, nitrogen (air contamination), argon (cover and process gas), CO and CO₂ (eventual decomposition of PCD and carbon release) were measured. The hydrogen flow rate was calculated using the measured concentrations of argon and hydrogen and the argon flow rate using formula:

$$m_H(t) = \frac{c_H(t)}{c_{Ar}(t)} \cdot m_{Ar}$$

Where m_H and m_{Ar} are volumetric flow-rates of hydrogen and argon and c_H and c_{Ar} are mass concentrations of hydrogen and argon measured in outgoing gas by mass spectrometer.

Argon flow-rate was measured with a precise volumetric flowmeter. Overall hydrogen production was then calculated as the integral of the hydrogen flow rate.

$$H = \int_{t_0}^{t_n} m_H(t) dt$$

Hydrogen production was finally normalized to the sample surface area to compensate for different sample sizes. CO and CO₂ concentration was measured to see any decomposition of PCD layer in two special experiments with high temperature preheating phase in inert atmosphere.

Ion Beam Irradiation

Ion beam irradiation tests were done at Texas A&M University (TAMU). Samples were irradiated by Fe⁺ ions at room temperature. To achieve a damage level of 10 dpa (typical irradiation damage for nuclear fuel rods), the samples were irradiated by 3 MeV Fe⁺ ions to a fluency of $1,95 \times 10^{16} \text{ cm}^{-2}$.

The ion implantation working temperature was estimated as 800 – 900 °C. The irradiation was performed at room temperature that is different from working power reactor environments. The projected range of Fe⁺ ions is about 1,1 μm and the coating thickness is about 300 nm. Therefore Fe⁺ ion penetration is deep enough to pass through the coating/substate interface [A3].

5.3 Coated Zr cladding tests after steam / water exposures

Optical microscopy of the metallographic cross sections of samples

Cross sections were acquired from the central parts of samples processed under 1000 °C hot steam by using an optical microscope. The samples were hot pressed into electrically conductive transparent resin (Bakelite), which is suitable for sample analyses via optical microscopy. The samples were ground using an automatic polishing device with a polishing head with individual contact pressure. The contact pressures were chosen according to the temperature at which each sample was exposed. Polishing was performed by using the same polishing device with an individual contact pressure of 35 N for all types of exposures. A classic canvas and a colloidal mixture of SiC (Colloidal Silica Polishing Suspension) from MasterMet™ were used for polishing. The samples were observed using an optical microscope after each polish.

Scanning Electron Microscopy (SEM) and Energy Dispersive X-Ray Spectroscopy (EDS)

The surface morphologies of the PCD coatings and surface morphologies and composition of CrAlSiN coatings were analyzed by using a Tescan FERA 3 scanning electron microscope. To minimize the interaction volume during imaging, the accelerating voltage in high-resolution mode was kept in the range of 2-5 kV. EDS composition analysis was performed using an EDAX Octane Super 60 mm² detector with an acceleration voltage of 5 kV for elemental analysis. The structures were opened using a Xe-FIB.

Raman spectroscopy

To determine the PCD layer composition (sp² and sp³-hybridized carbon), the deposited layers were characterized with Raman spectroscopy performed at room temperature using a Renishaw InVia Raman Microscope under the following conditions: a laser excitation wavelength of 488 nm (25 mW), ×50 Olympus objective, 65 μm slits, spot focus, and a grating of 2400 lines/mm. Spectra were acquired at various points across the samples to probe the homogeneity of the deposited PCD layers.

Inert gas fusion (IGF) – Hydrogen concentration measurements

The amount of hydrogen dissolved in the zirconium alloy after steam exposure (at either a low temperature simulating operating conditions or a high temperature simulating accident conditions) was determined with a G8 GALILEO analyzer. This analyzer operates on the basis of the inert gas fusion principle, which requires the fusion of the sample material in a graphite crucible at high temperatures. The concentration of the outgoing hydrogen is subsequently measured with a mass spectrometer. No correction for an oxide layer was applied; consequently, for heavily oxidized

samples from thermogravimetric experiments, the measured value of the hydrogen concentration does not exactly reflect the actual concentration in the sample.

X-ray Photoelectron Spectroscopy (XPS) analysis

XPS measurements were performed using an ESCA Probe P (Omicron Nanotechnology) with a primary X-ray source of monochromatized radiation from an Al anode (1486,7 eV). The constant analyzer energy (CAE) mode was used, at pass energies of 50 eV for overview spectra and 30 or 20 eV for detailed spectra. Charge compensation was achieved by using an electron gun at very low electron energies (between 1 eV and 2,5 eV) to protect the sample. Measurements of copper and calibration constants derived from these spectra were used for intensity calibration. The full widths at half maximum of the components used for the analysis of line details were based on experimental experience with the spectra of carbon and silver and were consistent with the capabilities of the instruments used. Spectral evaluation was conducted using CASA XPS software; the area of the peaks after calibration and a database of relative sensitivity factors were used for the determination of elemental concentrations. Chemical species were identified using XPS databanks. An ion gun (ISE5) connected to the preparation chamber was operated with argon ions, typically at an energy of 5 keV.

Secondary ion mass spectrometry (SIMS)

SIMS measurements were performed in depth profiling mode with a Cameca IMS 7f magnetic sector instrument. A Cs⁺ primary ion beam with an impact energy of 15 keV, a current of 20 nA and an impact angle of ~23° from the surface normal was raster scanned over an area of 100 μm x 100 μm, thus resulting in a sputter rate of ~1,4 nm/s. The depth scale of the SIMS craters was calibrated using a stylus profilometer. The instrument was operated at a low mass resolving power of $M/\Delta M \sim 400$. Standard precautions were taken to limit the distortions of the SIMS depth profile data caused by crater edge effects. Secondary ions were detected in single-ion counting mode using an electron multiplier or, for high count rates, using a Faraday cup and an electrometer amplifier. An electron beam in self-compensation mode was used for charge compensation during the analysis. The vacuum pressure in the analysis chamber during the measurement was approximately 1×10^{-9} mbar. Negatively charged secondary ions were monitored [A2].

XPS, UPS and work function analysis with a NanoESCA system

Uncoated and PCD-coated Zr alloy samples after hot steam tests were subjected to analyses of their work functions and surface potentials. For this purpose, a NanoESCA (Oxford Instruments Omicron Nanoscience) photoemission spectrometer based on a Photoelectron Emission Microscopy (PEEM) column and a double hemispherical imaging energy filter was used. This apparatus enables XPS, UPS and PEEM measurements and analyses using various excitation sources: monochromatic Al K $\alpha_{1,2}$ X-rays, a He discharge lamp (FOCUS HIS 13) and a Hg lamp. The valence band spectra for the determination of the Fermi level and the valence band maximum were acquired via XPS. Work function mapping was performed via PEEM using a Hg lamp. Furthermore, the work function values were also probed by obtaining UPS spectra. The work

function of each sample was extracted from the low-kinetic-energy cut-off of the UPS spectrum. The samples were briefly Ar sputtered to remove surface contamination [A2].

6 Results and discussion

6.1 Protective PCD coating on Zr alloy

PCD Long-Term Exposure in Reactor Operation Conditions

Long-term exposures were performed according ASMT G2 [31] at VSCHT (steam environment 400 °C) and Westinghouse Churchill Site in Pittsburgh (water environment 360 °C). According ASMT G2 are this two environments (steam 400 °C and water 360 °C) comparable. The autoclave tests were performed consistent with procedures used for testing zirconium alloys. All of the autoclave samples were measured and cleaned per [31]. PCD samples were tested in a 3,8 l stainless steel autoclave under static pure water conditions at 360 °C / saturation pressure (18,7 MPa). Dot peening was performed in lieu of engraving to mark each sample with unique identifications. This method was used to maintain control of sample identity while causing limited to no damage to the surface coating. Specimens were tested for a maximum of 195 days with specimen weight gains obtained at intermediate times and upon completion of the tests [A2]. In addition, specimens were visually inspected and photographed throughout the corrosion experiments. In Table 4 and Fig. 9 are displayed weight gains measured after long term exposure in water environment of PCD coated Zr samples and uncoated reference Zr samples, in all cases the PCD coated Zr samples have a lower weight gain than uncoated samples. Similar results were observed after exposure in steam environment (400 °C) for 4 days. In this case the weight gain for a 300 nm PCD layer coated Zr sample was 7,8 mg.dm⁻², whereas the weight gain for an uncoated Zr sample was 13,2 mg.dm⁻².

Table 4: Weight gains (mg/dm²) (corresponding to oxidation level) measured after autoclave tests of coated samples.[A2]

Geometry	PCD thick. [nm]	Weight gain [mg.dm ⁻²]							
		6 days	15 days	30 days	90 days	120 days	150 days	170 days	195 days
Tube	300	9,4	15,5	19,6	33,3	31	30	41	-
Tube	500	7,7	13,6	19,1	31,5	-	-	-	-
Plate	300	5,4	9,3	14,1	27,1	29	38	40	52
Plate	500	4,8	5,4	9,4	20,6	-	-	-	-
Tube	0	15,1	20,6	26,2	40,3	52	66	68	-
Plate	0	13,0	18,1	23,7	37,3	52	65	70	79

Tube samples and strip samples are from different materials, while tubular samples are from Zirlo and strip samples were low tin Zirlo. Only partial coverage with PCD layer is expected at inner surface of tubular samples.

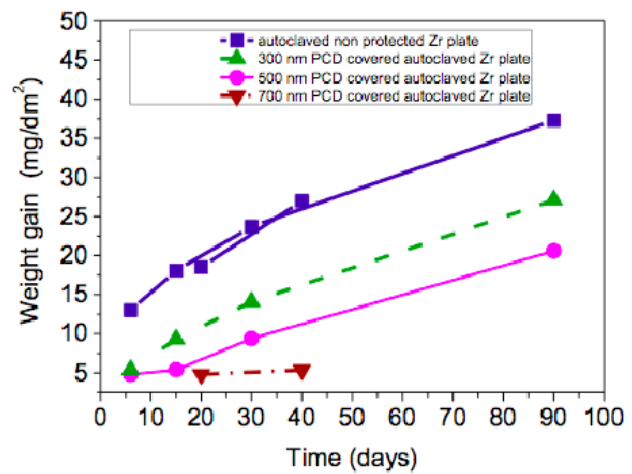
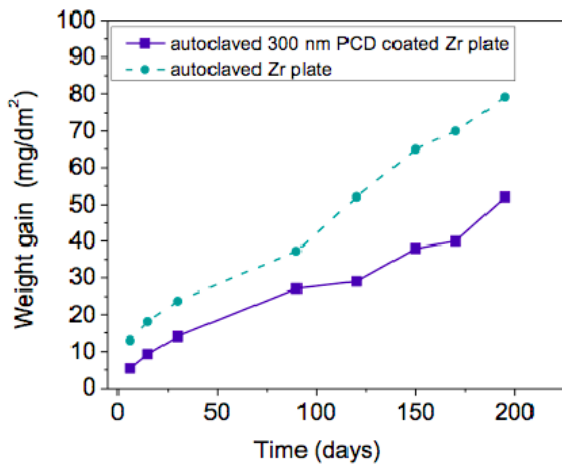


Fig. 9: (left) weight gains ($\text{mg}\cdot\text{dm}^{-2}$) measured after 6, 15, 30, 90, 120, 150, 170 and 195 days of exposure in water environment ($360\text{ }^\circ\text{C}$) for uncoated and 300 nm PCD-coated plate samples. (right) weight gains ($\text{mg}\cdot\text{dm}^{-2}$) measured after 6, 15, 20, 30, 40 and 90 days of exposure in water environment ($360\text{ }^\circ\text{C}$) for uncoated, 300 nm PCD-coated, 500 nm PCD-coated and 700 nm PCD-coated ZIRLO plate samples. Thicker PCD layers provide stronger protection against oxidation than thinner layers [A2].

The MW-LA-PECVD apparatus setting is extremely important: The best protective effect was achieved by a 700 nm PCD coating on Zr alloy plates, following hot water processing ($360\text{ }^\circ\text{C}$, 20 – 40 days) surface oxidation was reduced by more than 50 %. The apparent higher PCD protection effectivity of plate samples compared to tubular samples is caused by non-coverage on the inner surfaces of tubes compared with complete coverage of plate samples.

PCD Ion Beam Irradiation

Prepared samples (Fig. 10) covered with polycrystalline diamond layer were tested at the Texas A&M University Ion Beam Laboratory. Irradiation tests were performed in order to simulate the neutron flux in nuclear reactor.

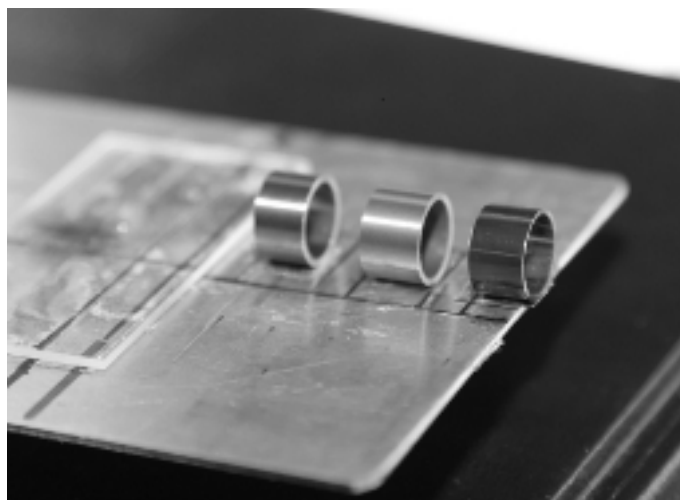


Fig. 10: Samples with PCD coating prepared on holder for Ion Beam Irradiation

To achieve a damage level of 10 dpa, the sample was irradiated by 3 MeV Fe⁺ ions to a fluence of 1,95×10¹⁶ cm⁻². As shown in Fig. 11, SRIM calculations predicted a peak damage of 0,9 displacement per Å·ion at a depth of 1 μm in the diamond layer. The simulation considered normal incidence of the Fe⁺ ions into a flat surface. In reality, the cylindrical surface of the sample will lead to variance of incidence angles. We therefore characterized the sample region locally normal to the ion beams.

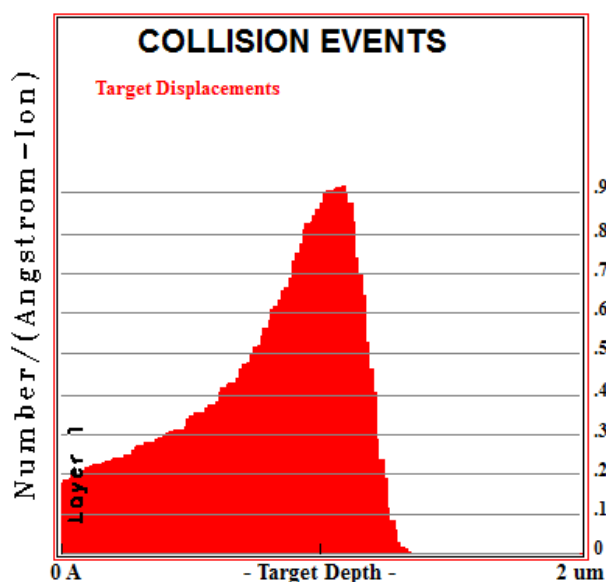


Fig. 11: SRIM calculated distribution of target displacements as a function of depth into the surface of the sample. [A5]

The projected range of Fe ions is about 1,1 μm and the PCD layer thickness is about 300 nm. Therefore, the Fe ion penetration is deep enough to pass through the PCD/Zr interface. After the Ion Irradiation test the Raman spectra of the PCD film showed an increase in the intensity of the graphite related peak (~1600 cm⁻¹) and the diamond film still shows satisfactory structural integrity with both sp³ and sp² carbon phases. This can be the effect of sp³ carbon chemical bonds breaking and conversion into sp² carbon as inclusions in film due displacement of carbon atoms. Scanning Electron Microscopy was employed to evaluate coverage, crystal size, crystal shape and growth rates on all grown layers. Coverage of seeded areas was found to be with no pinholes for all layers. No change in the polycrystalline diamond layer after ion beam irradiation was detected [A5].

PCD Thermogravimetry and hydrogen production measurement

Thermogravimetry experiments were performed at NETZSCH thermo-balance, using argon as a cover gas. Simple alumina holder was used as sample support. All steam expositions were isothermal without any changes in steam or cover gas flow-rate. All oxidations were realized with argon flow-rate of 3 l per hour and with steam flow-rate of 3 g per hour. Measured TG data were smoothed using moving average filter, in order to eliminate oscillations of thermo-balance mechanism. Temperatures 900 °C, 1000 °C, 1100 °C and 1200 °C were chosen for thermogravimetric measurements.

Weight gain time dependences of PCD coated samples, measured by NETZCH thermo-balance at different temperatures from 900 °C to 1200°C are on Fig. 12 and hydrogen concentration outgoing gas is on Fig. 13.

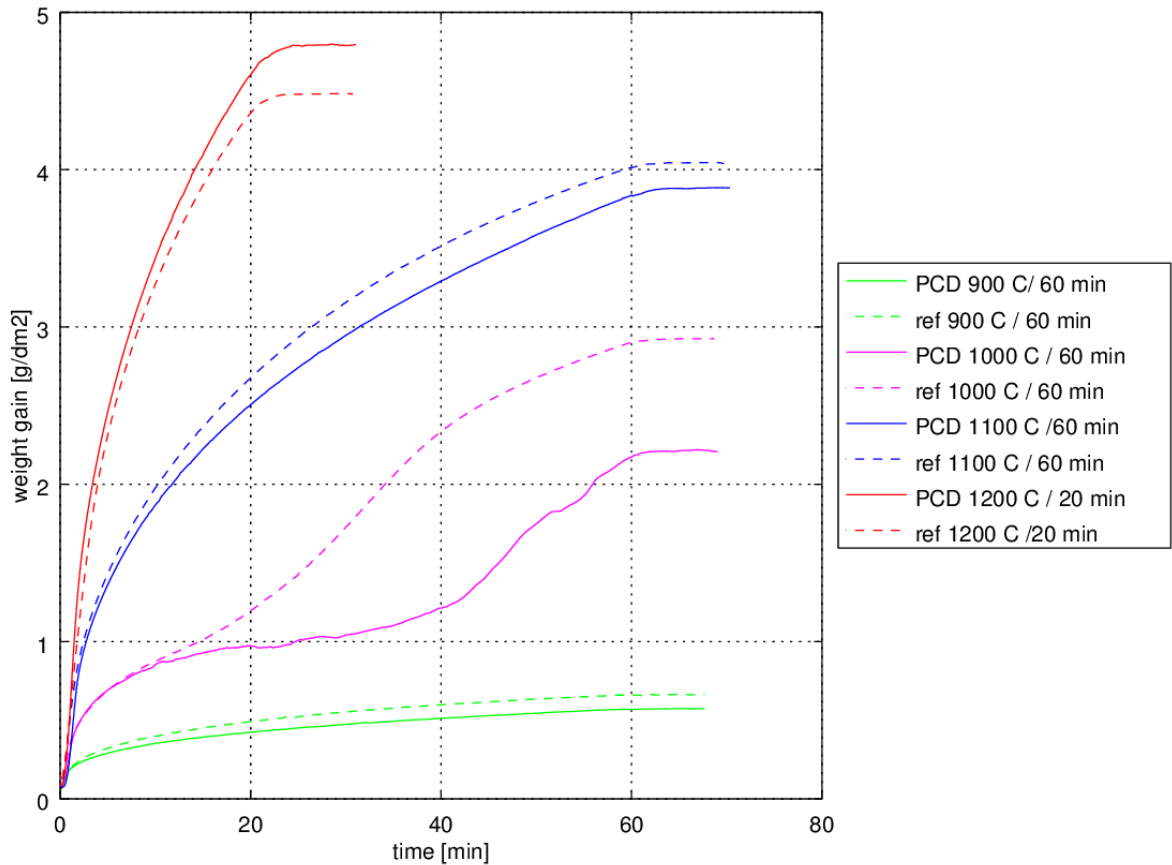


Fig. 12: Thermogravimetry of PCD coated Zirlo

Oxidation kinetics of PCD coated samples is similar to kinetics of uncoated samples at almost all temperatures, but with lower hydrogen production and lower weight gains. Most important difference is in later beginning of breakaway oxidation at 1000 °C, when breakaway oxidation starts on PCD coated sample 15 minutes later.

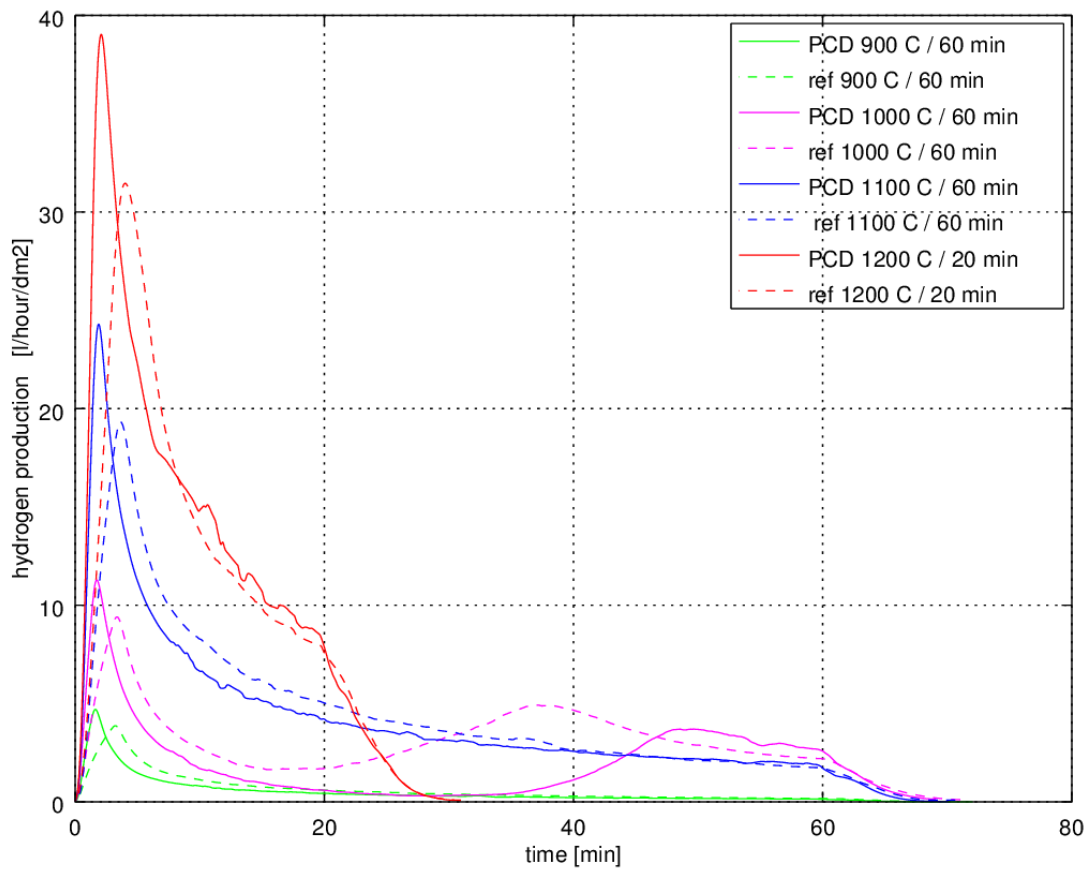


Fig. 13: Hydrogen production during TG exposures of PCD coated Zirlo

Special test with sample pre-oxidation was performed in order to see any changes (if they occur) in structure of PCD layer at temperatures below 800 °C. Pre-oxidation phase at 500 °C and 700 °C for 20 minutes was chosen, before exposing the sample to steam at 1000 °C. No steam was introduced to the furnace during transition heating phases. Sample with higher (700 °C) temperature of pre-oxidation phase has lower weight gain and hydrogen release in main oxidation phase, what is probably caused by thicker oxide layer developed during pre-oxidation phase. No failure of PCD layer was observed during pre-oxidation phase [A6].

Measures overall weight gain and measured overall hydrogen production with calculated ECR summarized in Table 5.

Table 5: Overall TG weight gain and hydrogen production [A2]

Temp. [°C]	Time [min]	Weight gain [g.dm ⁻²]		ECR [%]		Hydrogen produced [l.dm ⁻²]	
		Coated	Reference	Coated	Reference	Coated	Reference
PCD coatings on Zirlo							
900	60	0,55 ± 0,01	0,64 ± 0,01	8,5	9,9	0,56	0,69
1000	60	2,14 ± 0,01	2,87 ± 0,01	33,0	44,2	2,20	3,44
1100	60	3,83 ± 0,01	3,98 ± 0,01	59,1	61,4	4,69	4,96
1200	20	4,73 ± 0,01	4,41 ± 0,01	72,9	68,0	5,81	5,28

PCD Carbon monoxide and carbon dioxide measurement

Concentration of CO and CO₂ in outgoing gas from high temperature oxidation was measured in order to see any decomposition PCD layer during heating and steam exposure phases. Measured data are visualized on Fig. 14. Measured data were strongly filtered with moving average filter to reveal any increasing or decreasing trends, as primary data were too noisy. CO and CO₂ concentrations has to normalized with its maximal values because relatively low concentration.

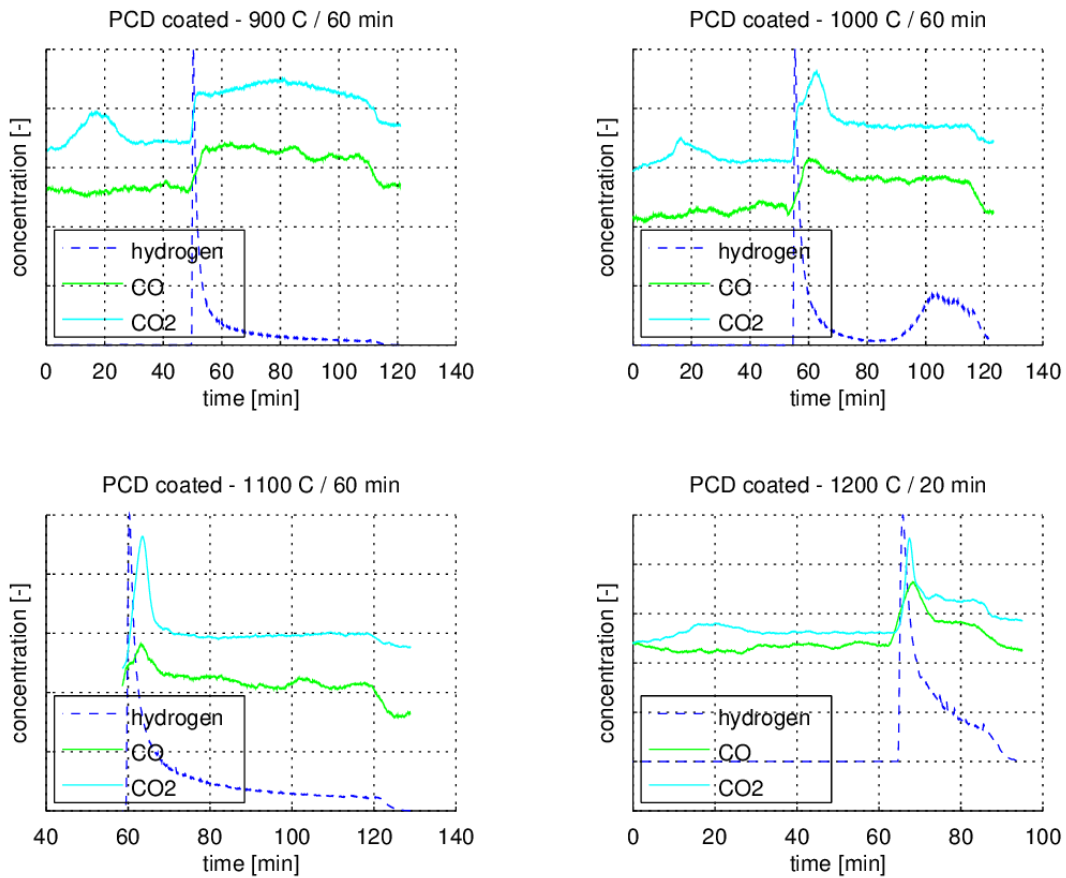


Fig. 14: CO and CO₂ relative concentration in outgoing gas (hydrogen data are here only to show time when steam valve was open and oxidation of Zr sample begins)

PCD High-temperature exposures

BOX furnace allows steam exposition of coated samples at very high temperatures (up to 1600 °C) at steam flow-rates around 30 kg/hour. Outgoing gas was analyzed by GAM 300 quadrupole mass spectrometer with interest especially in hydrogen, steam, and argon concentrations. Special interest was in CO and CO₂ measurements on PCD coated samples in order to observe any changes in PCD structure at high temperatures.

Very high temperature test was performed in BOX furnace. Exposition parameters were set as follows: temperature – 1400 °C, time – 6 min., argon flow-rate – 30 l/hour, steam flow-rate – 40 g/hour. Time was determined after previous calculation using Carthcarth – Pawel correlation in order to avoid complete oxidation of the sample. Data are summarized in Table 6.

Table 6: Overall weight gains and hydrogen productions from high temperature exposures

Temp. [°C]	Time [min]	Weight gain [g.dm ⁻²]		ECR [%]		Hydrogen produced [l.dm ⁻²]	
		Coated	Reference	Coated	Reference	Coated	Reference
PCD coatings on Zry-2							
1200*	30	3,41 ± 0,01	3,56 ± 0,01	48,72	50,75	-na-	-na-
1200*	60	5,45 ± 0,01	5,48 ± 0,01	77,82	78,29	5,99	7,42
PCD coatings on Zirlo							
1400	6	4,91 ± 0,01	3,13 ± 0,01	75,55	48,21	3,95	2,59

PCD Optical appearance of the samples

Optical appearance of PCD coated samples did not change during long term exposure in autoclave (see Fig. 15).

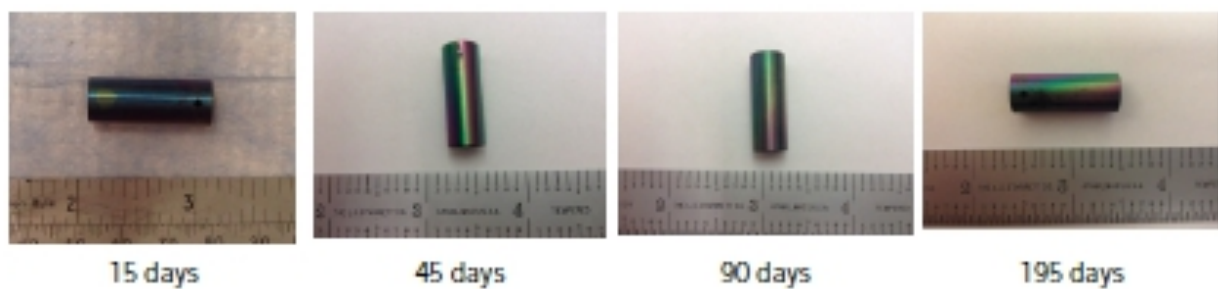


Fig. 15: Optical appearance of PCD coated samples after long term exposure (photo: Westinghouse)

PCD Raman spectroscopy

Polycrystalline diamond films quality was investigated using Raman spectroscopy. Raman spectroscopy was performed on all tube samples coated with polycrystalline diamond (PCD) film prior and after each testing (Long-term corrosion testing, high temperature oxidation tests and ion beam irradiation) to gain insight on diamond layer changes during oxidation. All measurements

were carried out at room temperature using a Renishaw InVia Raman Microscope.

Raman spectroscopy measurements on the PCD coated samples before testing exposures revealed the existence of peaks related to sp^3 diamond (1332 cm^{-1}) and sp^2 – containing graphitic carbon (1600 cm^{-1}) phases. Measurements taken at positions over the entire surface of the cladding tube showed diamond growth and incorporation of amorphous carbon and graphite.

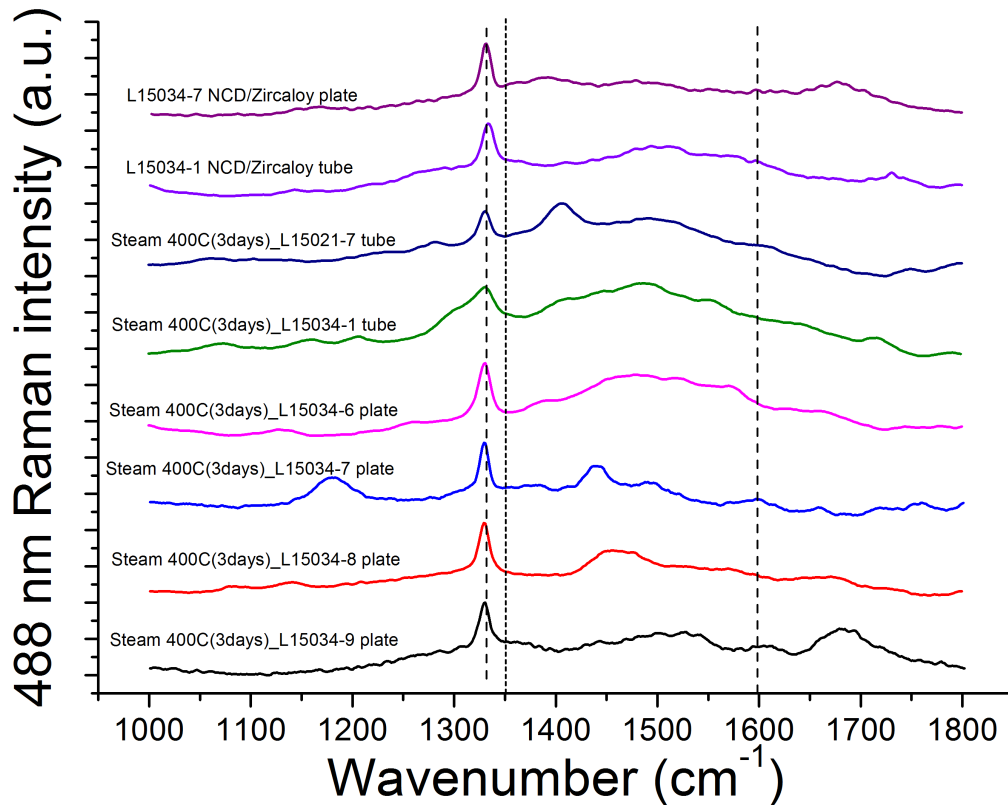


Fig. 16: Raman spectroscopy - samples after low-temp, long-term test [A2]

No change in PCD layer was observed after long-term exposure (Fig. 16). After oxidation at $900\text{ }^{\circ}\text{C}$, $1000\text{ }^{\circ}\text{C}$ and $1100\text{ }^{\circ}\text{C}$ a mixture of sp^2 carbon, sp^3 carbon (diamond) and graphite-related features are visible. At $1200\text{ }^{\circ}\text{C}$ steam exposed sample a complete transition to the graphite-related content is evident by a narrowing of the peak widths. A weak signal sample at $1400\text{ }^{\circ}\text{C}$ suggests the rapid transition of the diamond coating to various carbon phases (Fig. 17).

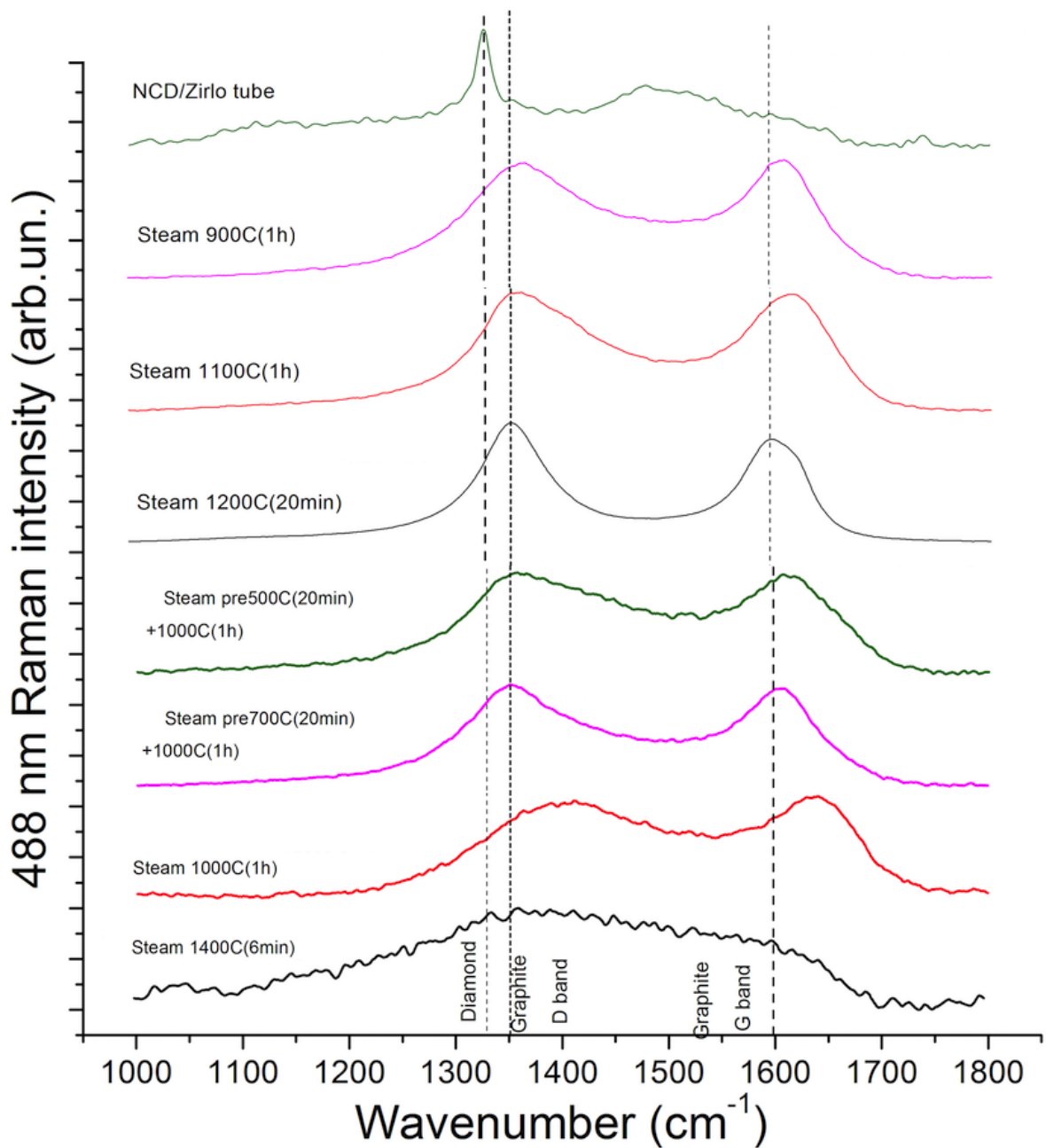


Fig. 17: Raman spectroscopy - PCD samples after high temp exposures [A2]

PCD Optical microscopy

Different polishing and etching techniques was used for sample preparations, that resulted in slightly different look of metallographs. Furthermore, different types of metallographical microscopes at different laboratories (KIT, CTU) were used, so enlightening is also different. Cross-section metallographic results are discussed in Table 7, Table 8 and Table 9.

Table 7: PCD coated samples after 400 °C / 3 days exposure - Optical microscopy

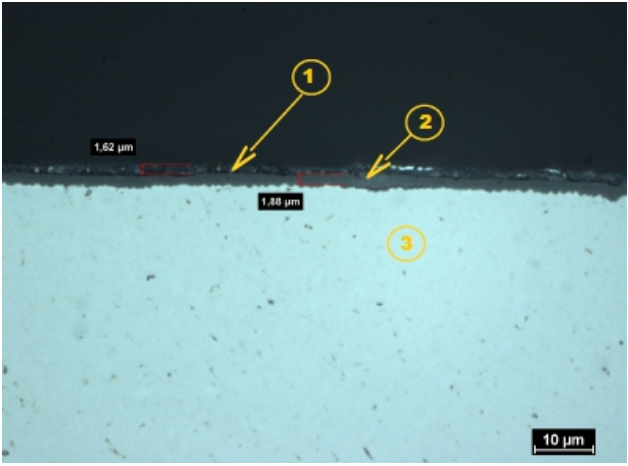
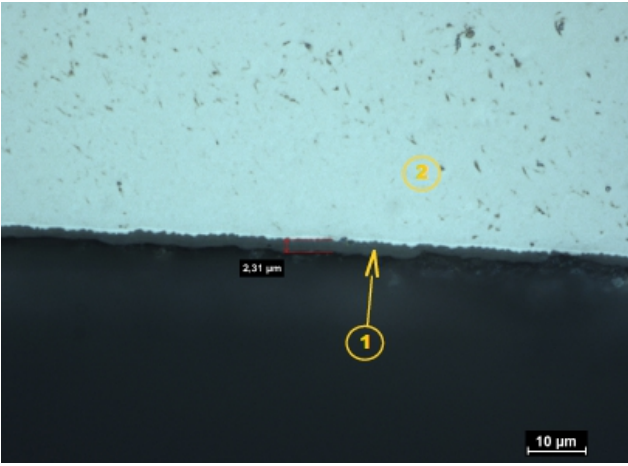
PCD (Zirlo) – 400 °C, 3 days	
	
<p>OUTER SURFACE</p> <ul style="list-style-type: none"> (1) Surface layer containing PCD protective coating - with thickness 1,62 μm. (2) Oxide layer (ZrO₂), thickness 1,88 μm (3) Substrate material – no prior β-Zr phase is present, as the sample has not reached α-Zr to β-Zr transition temperature. 	<p>INNER SURFACE</p> <ul style="list-style-type: none"> (1) Oxide layer (ZrO₂), thickness 2,31 μm (2) Substrate material – no prior β-Zr phase is present, as the sample has not reached alpha to beta transition temperature.

Table 8: PCD coated samples after 900 °C / 60 minutes exposure - Optical microscopy

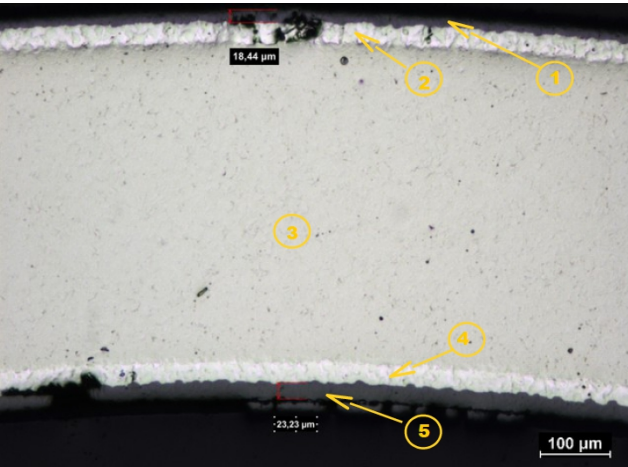
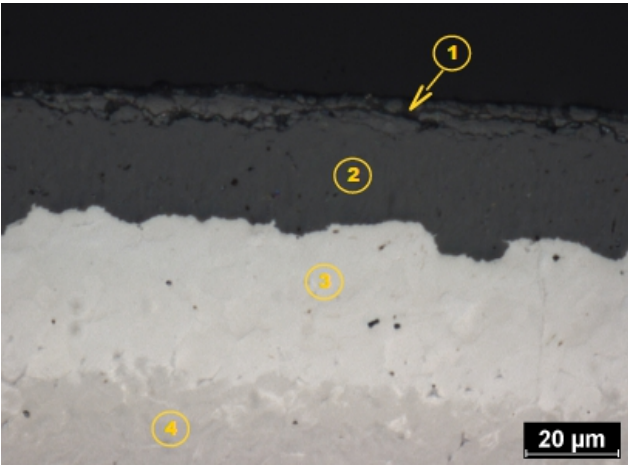
PCD (Zirlo) – 900 °C, 60 min	
	
<ul style="list-style-type: none"> (1) Oxide layer of ZrO₂, layer (2) Oxygen stabilized α-Zr phase (3) prior β-Zr phase (4) Oxygen stabilized α-Zr phase (5) Oxide layer of ZrO₂ with initial breakaway oxidation and partial oxide spallation 	<p>OUTER SURFACE DETAIL</p> <ul style="list-style-type: none"> (1) Non-homogeneous outer oxide layer (2) Homogeneous Zr oxide layer (3) Oxygen stabilized α-Zr phase (4) prior β-Zr phase
<ul style="list-style-type: none"> • Outer oxide thickness: 18,44 μm • Inner oxide thickness: 23,23 μm 	

Table 9: PCD coated samples after 1000 °C / 60 minutes exposure - Optical microscopy

PCD (Zirlo) – 1000 °C, 60 min	
<p>(1) Oxide layer of ZrO₂ with initial breakaway oxidation (2) Oxygen stabilized α-Zr phase (3) prior β-Zr phase (4) Oxygen stabilized α-Zr phase (5) Oxide layer of ZrO₂ with initial breakaway oxidation</p>	<p>OUTER SURFACE DETAIL (1) Oxide layer of ZrO₂ with initial breakaway oxidation (2) Oxygen stabilized α-Zr phase (3) prior β-Zr phase</p>
<ul style="list-style-type: none"> • Outer oxide thickness: 90,80 μm • Inner oxide thickness: 125,02 μm 	

Optical microscopy reveals oxide grows below PCD layer on outer surface. Oxidation rate is lower on the outer tube surface which was protected by thin PCD layer, then on the inner unprotected surface.

PCD Hydrogen concentration in Zr metal measured by IGF

The samples were taken from the center of each piece to avoid edge effects. The PCD coating was not removed prior to the analysis. Knowing the area, initial weight and final weight of each sample, along with the bulk hydrogen concentration, the hydrogen pickup fraction was calculated. The initial hydrogen concentration of 8 ppm was used in the hydrogen pickup calculations. Measured values are summarized in Table 10.

Table 10: Hydrogen concentrations measured by IGF [A2]

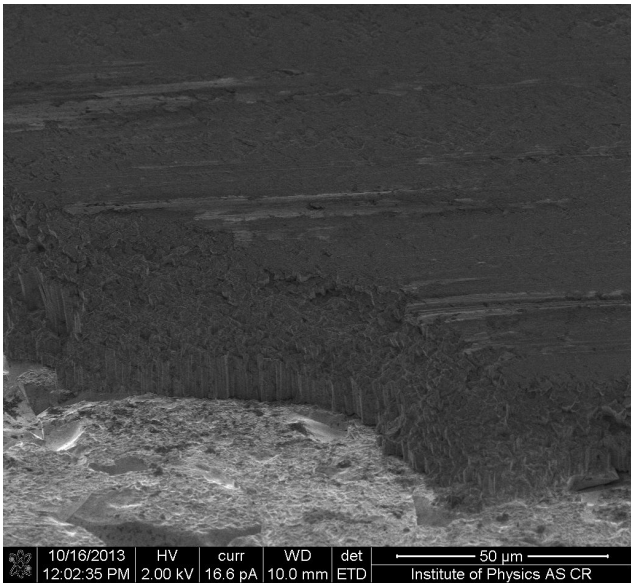
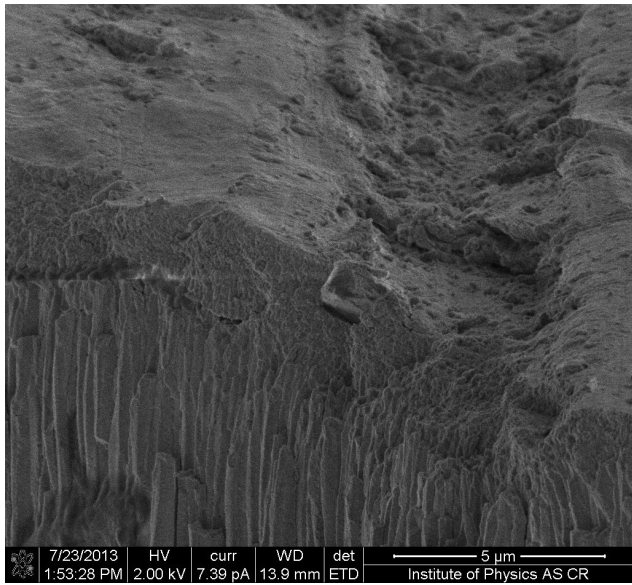
Temp. [°C]	Time [min]	Hydrogen concentration [ppm]	
		Coated	Reference
PCD coatings on Zirlo			
1200	2 x 30	63,35	520,8
1100	60	51,33	571,4
400	3 days	25,6	17,8

PCD on Zry-2			
1200	2x30	69,17	62,3
PCD on low Sn Zr			
400	3 days	21,85	16,6

PCD SEM observations

SEM imaging (Table 11) was performed on partly scratched surface of oxidized sample (1000 °C, 1 hour) – scratch was made intentionally in order to see oxide and PCD coating structure. SEM reveals relatively homogeneous PCD layer even on top of the zirconium dioxide.

Table 11: SEM detail of PCD – substrate interface

PCD (Zirlo) – 1000 °C, 60 min	
	
<p>OUTER SURFACE</p> <ul style="list-style-type: none"> (1) Metal (2) Columnar structure of ZrO₂ (3) PCD layer 	<p>DETAIL OF PCD LAYER</p>

PCD X-ray photoelectron spectroscopy

The protective capabilities of the PCD layers were further evidenced by XPS data acquired from the PCD-coated (300 nm) and uncoated Zirlo tubes before and after steam exposure (in an autoclave for 4 days at 400 °C). The XPS spectra were obtained from cross sections of the samples.

Regarding the analysis of the carbon states, the presence of carbides and forms of carbon with a binding energy near 285 eV was determined from the detailed spectra of the C1s peak (Fig. 18).

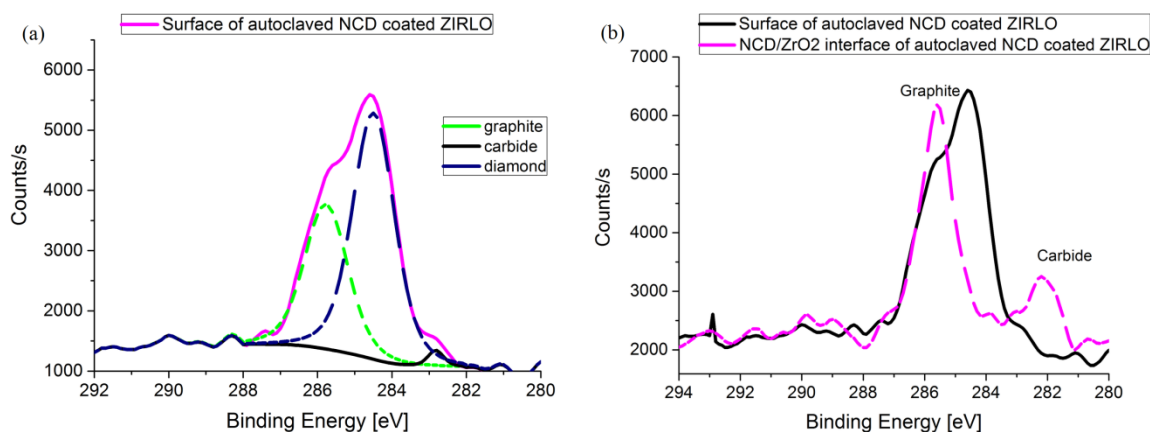


Fig. 18: C1s lines of Zirlo coated with PCD after calibration on the basis of the Zr 3d5/2 line. The areas analyzed were on the PCD surface and at the PCD/ZrO₂ interface after hot steam exposure (400 °C, 4 days). Four different states of carbon are evident (left): graphite, with a binding energy of 285,4 eV; diamond, with a binding energy of 284,2 eV; carbon in a single bond with oxygen, with a binding energy of 286.1 eV; and carbide, with a binding energy of 282 eV. Carbides were also present below the PCD layer (right). [A2]

PCD Secondary ion mass spectrometry (SIMS)

We used SIMS to determine the changes in the C depth profile of a 300 nm PCD-coated Zr alloy tube before and after 4 days of exposure to 400 °C hot steam. The SIMS data showed that after 4 days at 400 °C in hot steam, a large amount of C was contained in the ZrO₂ layer formed beneath the protective PCD layer. The exposure to hot steam clearly resulted in the diffusion of carbon into the ZrO₂ layer to a depth larger than 1,5 μm (Fig. 19). In a reference PCD-coated Zr alloy sample (not exposed to hot steam), the majority of the carbon atoms were contained within the thickness of the PCD layer itself. The depth profiles of C and O are in units of counts/s and labelled in the graphs.

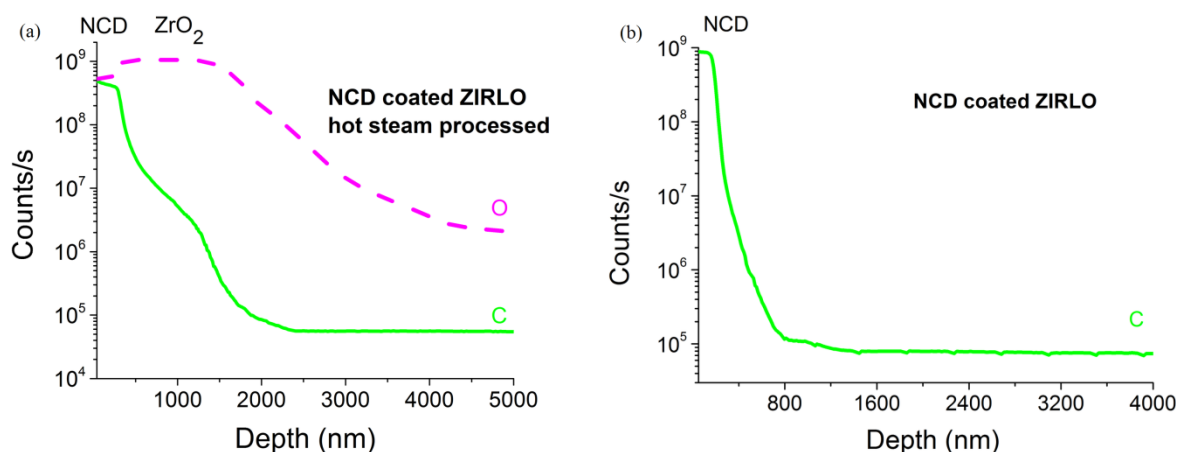


Fig. 19: SIMS data showing that after 4 days of hot steam exposure at 400 °C, the ZrO₂ layer in 300 nm PCD-coated Zr alloy contained C to a depth bigger than 1,5 μm (left), whereas in non-exposed PCD-coated Zr alloy, the majority of the carbon was contained only within the thin (0,4 μm) PCD layer (right). The depth profiles of C and O are in units of counts/s and labelled in the graphs. [A2]

PCD Capacitance measurements

Capacitance measurements were performed on uncoated Zr alloy tubes before and after steam exposure (400 °C for 4 days) and on 300nm PCD-coated Zr alloy sample exposed to the same steam conditions. The types and densities of the defects in the surface films were determined.

The nature of the electric field at the ZrO₂/Zr interface depends on the semiconductor type (donor/acceptor densities) and markedly influences oxygen transport through the oxide/metal interface.

Measurements showed, that the oxide films on uncoated and steam exposed samples were found to exhibit solely n-type semi-conductive behavior. This result was consistent with observations of pure zirconium [32] and of Zr-Nb [33] and Zr-Sn alloys [34]. The results of the doping density analysis are presented in Table 12, where N_A and N_D denote the acceptor and donor densities, respectively. A high donor density (characteristic of an n-type semiconductor) was found for the uncoated Zr samples both before and after hot steam exposure, whereas the PCD-coated Zr samples after steam exposure showed both p-type (acceptor-containing) and n-type semi-conductive behavior.

Table 12: Acceptor and donor densities obtained from the Mott-Schottky plots [A2]

Sample	N _A [cm ⁻³]	N _D [cm ⁻³]
Zirlo (uncoated)	-	4 × 10 ²⁰
Zirlo (4 days at 400 °C)	-	2,3 × 10 ¹⁸
Zirlo with 300 nm PCD, 4 days at 400 °C	4,4 × 10 ¹⁶	2 - 3 × 10 ¹⁶

6.2 Protective coatings based on Cr – Al – Si nitrides

CrAlSiN coating preparation

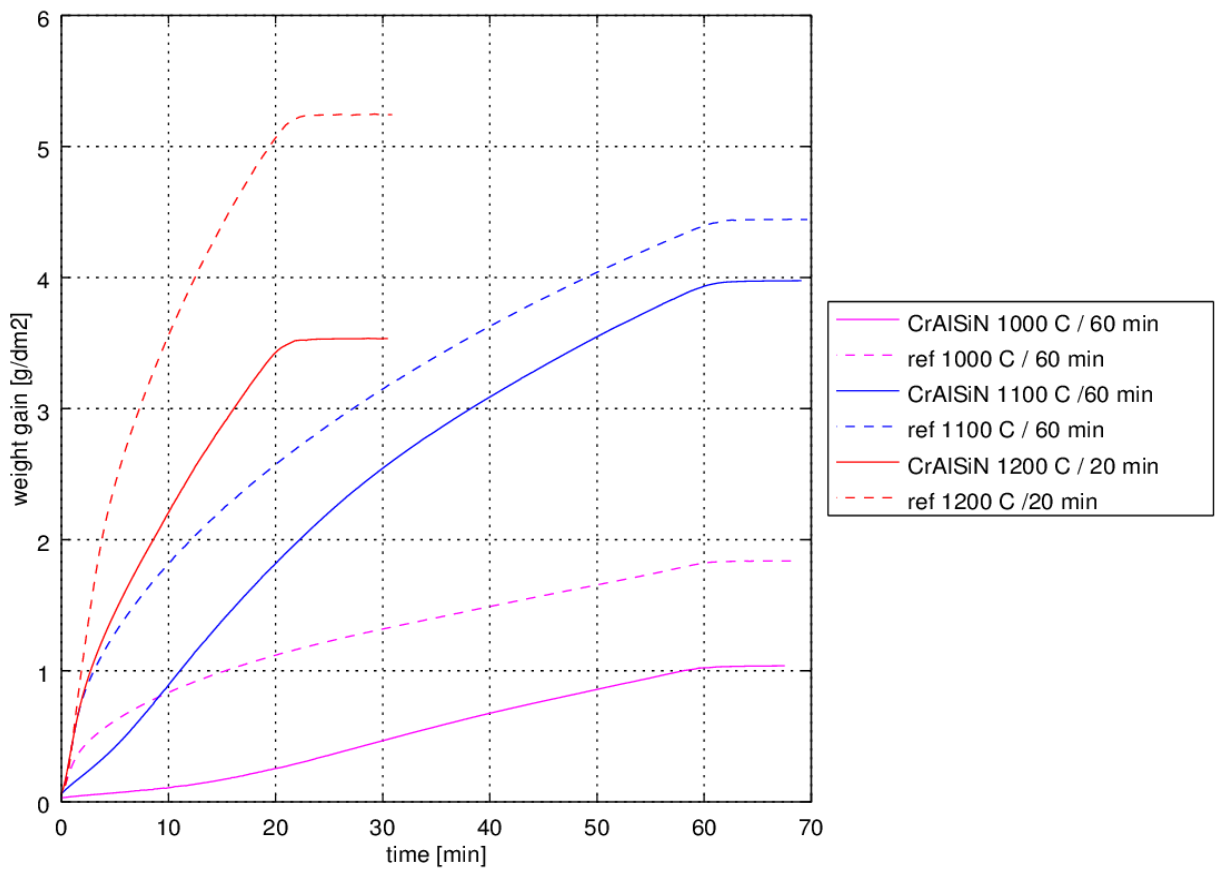
CrAlSiN was deposited on Zircaloy-2 zirconium alloy using method of Physical Vapor Deposition (PVD). Composition of nitrides in coating is: 36,5 % (Al), 4,8 % (Si), 58,7 (Cr). Thickness of the coating varies between 2 – 4,5 μm. As proved later samples were coated only on outer surface. Properties of prepared coating: Micro-hardness 35 GPa, thickness 2 – 4,5 μm and roughness Ra 0,15 – 0,20 μm.

CrAlSiN Long-Term Exposure in Reactor Operation Conditions

Long-term exposures were performed according ASMT G2 at VSCHT (steam environment 400 °C) The autoclave tests were performed consistent with procedures used for testing zirconium alloys.

CrAlSiN Thermogravimetry and hydrogen production measurement

Weight gain and hydrogen production of CrAlSiN coated and uncoated (reference) samples are visualized in Fig. 20 and Fig. 21. Lower hydrogen production and lower mass gain of CrAlSiN coated sample is visible at temperature 1000 °C. Even at temperature 1100 °C is no hydrogen peak present at the beginning of steam exposure and also weight gain denotes lower reaction kinetics. Exposure at 1200 °C also shows lower oxidation kinetics but hydrogen peak during beginning of oxidations phase is present.



ig. 20: Thermogravimetry of CrAlSiN coated Zry-2

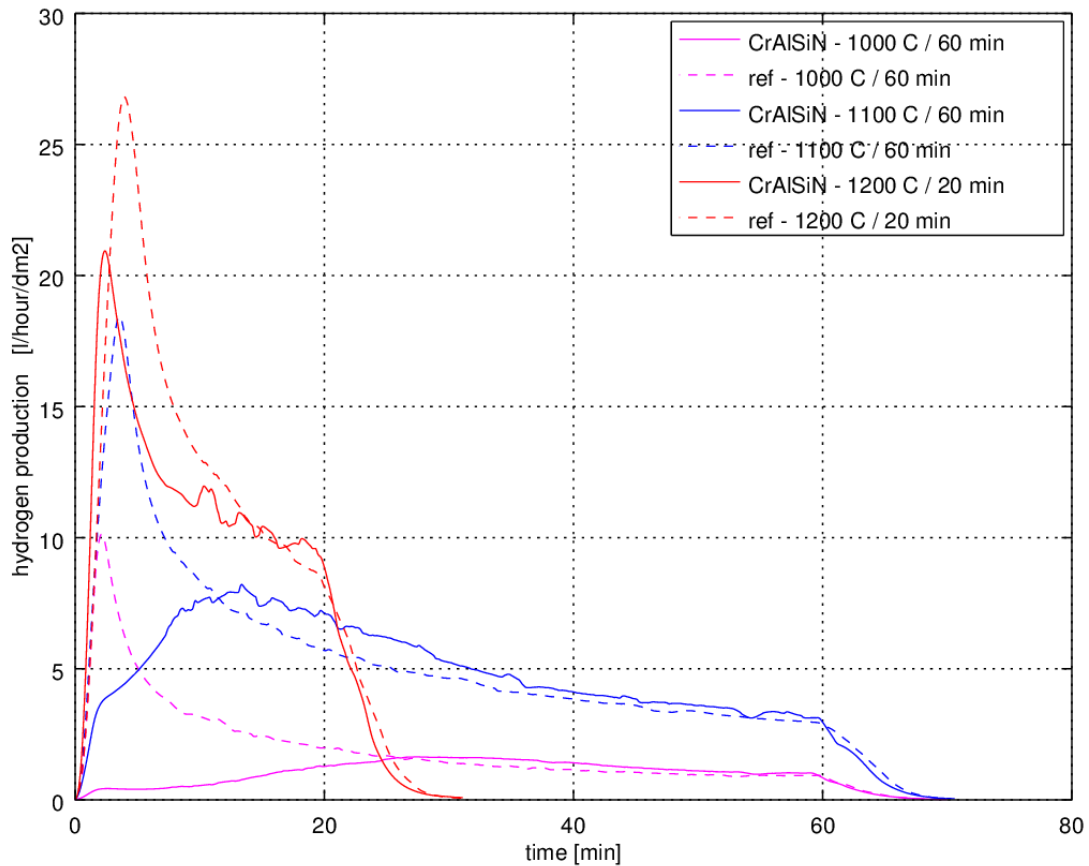


Fig. 21: Hydrogen production during TG exposures of CrAlSiN coated Zy-2

Measures overall weight gain and measured overall hydrogen production with calculated ECR summarized in Table 13.

Table 13: Overall TG weight gain and hydrogen production

Temp. [°C]	Time [min]	Weight gain [g.dm ⁻²]		ECR [%]		Hydrogen produced [l.dm ⁻²]	
		Coated	Reference	Coated	Reference	Coated	Reference
CrAlSiN coatings on Zry-2							
1000	60	1,01 ± 0,01	1,82 ± 0,01	14,4	24,5	1,15	2,11
1100	60	3,94 ± 0,01	4,39 ± 0,01	56,3	59,3	5,22	5,79
1200	20	3,48 ± 0,01	4,15 ± 0,01	49,7	56,1	4,33	4,99

CrAlSiN High-temperature exposures

Three samples from Zircaloy-2 were oxidized at 1200 °C for two times 30 minutes. First sample was coated with PCD, second with CrAlSiN and third one was left uncoated as reference sample.

After first 30 minutes in steam were samples cooled down in inert argon atmosphere and removed from BOX furnace. Sample was than returned back to furnace after measuring of weight gain for second 30 minutes long exposure.

Very high temperature test was performed in BOX furnace. Exposition parameters were set as follows: temperature – 1400 °C, time – 6 min., argon flow-rate – 30 l/hour, steam flow-rate – 40 g/hour. Time was determined after previous calculation using Carthcarth – Pawel correlation in order to avoid complete oxidation of the sample. Data are summarized in Table 14.

Table 14: Overall weight gains and hydrogen productions from high temperature exposures

Temp. [°C]	Time [min]	Weight gain [g.dm ⁻²]		ECR [%]		Hydrogen produced [l.dm ⁻²]	
		Coated	Reference	Coated	Reference	Coated	Reference
CrAlSiN coatings on Zry-2							
900	240	0,71 ± 0,01	0,96 ± 0,01	10,1	13,0	0,95	1,34
1000	60	1,38 ± 0,01	0,98 ± 0,01	19,7	13,9	1,57	1,26
1100	40	2,43 ± 0,01	2,98 ± 0,01	34,7	43,54	3,29	3,82
1200**	30	2,83 ± 0,01	3,56 ± 0,01	40,2	50,8	-na-	-na-
1200**	60	4,75 ± 0,01	5,48 ± 0,01	68,9	78,3	6,63	7,42
1400	6	4,82 ± 0,01	3,29 ± 0,01	68,86	44,48		

CrAlSiN Optical microscopy

Several polishing and etching techniques was used for sample preparations, that resulted in slightly different look of metallographs. Furthermore, different types of metallographical microscopes at different laboratories (KIT, CTU) were used, so enlightening is also different.

Table 15: CrAlSiN optical microscopy results at 1000 °C / 60 min. samples

CrAlSiN (Zry-2) – 1000 °C, 60 min	
<p>(1) Partial segregation of inner oxide layer – probably caused during polishing (2) Inner part of cladding tube still consist of relatively thick prior β-Zr phase</p>	<p>Several Zr oxide “nodes” or “blisters” with different size are present on outer surface.</p>
<p>“BLISTER” DETAIL Zr oxide “blister”, which developed after coating failure with visible initial crack (1) and secondary coating cracks (2). Secondary cracks are caused by expansion of zirconium oxide underneath the coatings. Coating residua are still present on outer surface.</p>	<p>COMPACT COATING DETAIL Detail of area where no oxidation of zirconium. Different areas are visible on coating layer.</p>
<ul style="list-style-type: none"> • Inner oxide thickness: 230 μm • Outer (coated) surface oxide thickness (best): 0 μm • Outer (coated) surface oxide thickness (worst): 360 μm 	

Table 16: CrAlSiN optical microscopy results at 1100 °C / 60 min. samples

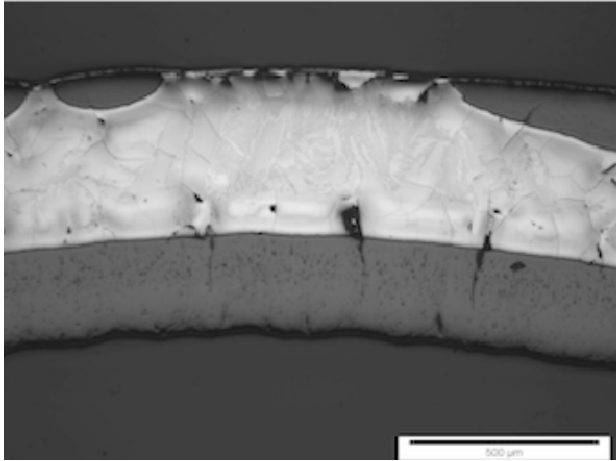
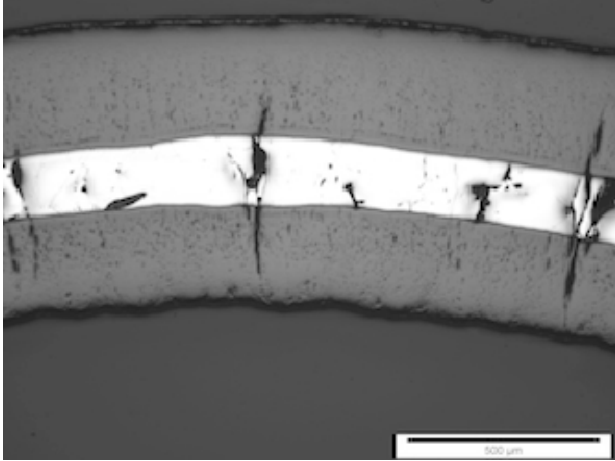
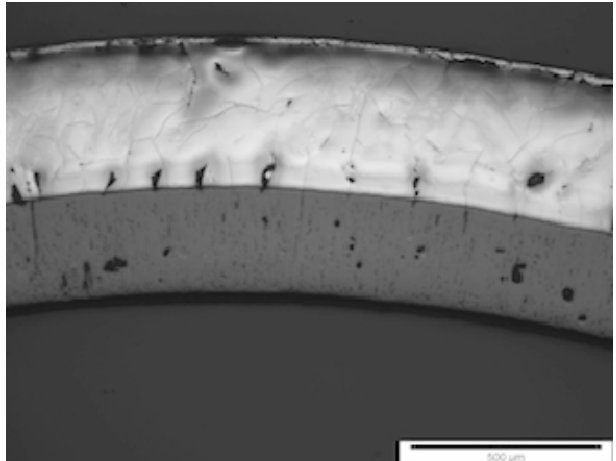
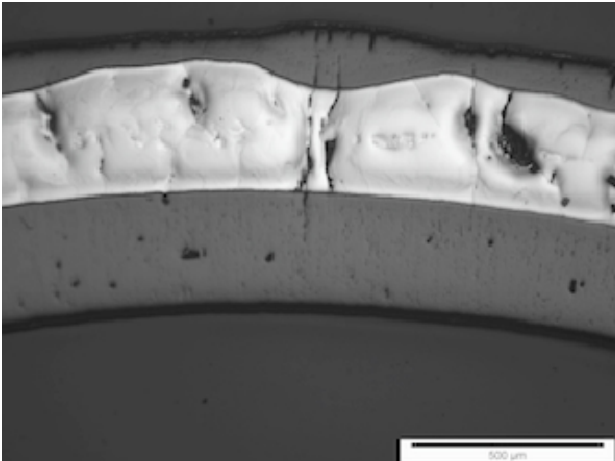
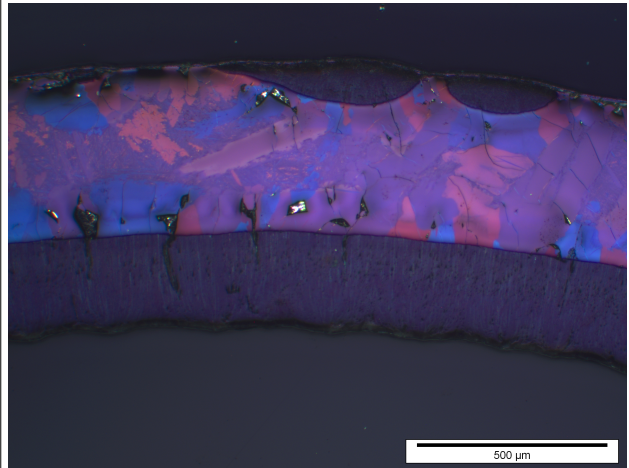
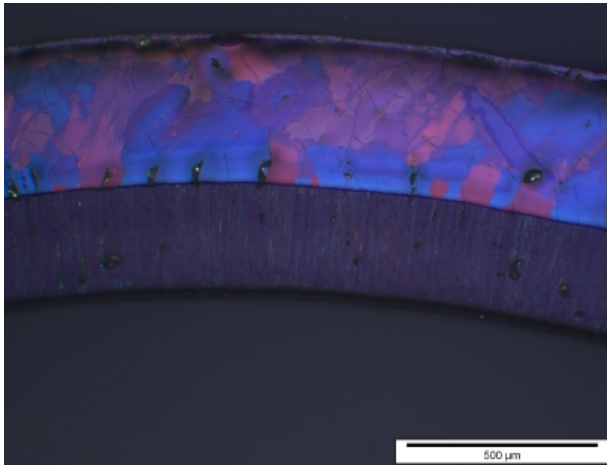
CrAlSiN – 1100 °C, 60 minutes	
	
Several failures of coating on outer surface with developing oxide layer with variable thickness. Thin α -Zr layer is visible on Zr oxide blisters on outer surface, but prior β -Zr is still present on significant part near outer surface.	Thick oxide layers on both outer and inner surfaces are visible. No prior β -Zr phase is present.
<ul style="list-style-type: none"> • Inner oxide thickness: 230 μm • Outer (coated) surface oxide thickness (best): 0 μm • Outer (coated) surface oxide thickness (worst): 360 μm 	
<ul style="list-style-type: none"> • Reference sample inner oxide thickness: 260 μm • Reference sample outer oxide thickness: 310 μm 	

Table 17: CrAlSiN optical microscopy results at 1200 °C / 20 min. samples

CrAlSiN – 1200 °C, 20 minutes	
	
Optical microscopy reveals no ZrO_2 layer on outer surface. No prior β -Zr phase on outer diameter indicates no or very limited diffusion of oxygen through the coating.	Thick oxide layer on inner surface and developing homogenous Zr oxide layer on outer surface with variable thickness are visible. No prior β -Zr phase is present.



Polarized optical microscopy image clearly shows prior β -Zr grain (grains with sharp texture) structure on outer surface. Oxygen containing and oxygen stabilized α -Zr grain structure (more rounded grains) is present on inner surface underneath the oxide layer.

- Inner oxide thickness: 290 μm
 - Outer (coated) surface oxide thickness (best): 0 μm
 - Outer (coated) surface oxide thickness (worst): 170 μm
-
- Reference sample inner oxide thickness: 212 μm
 - Reference sample outer oxide thickness: 283 μm

From metallographic observations is clear that CrAlSiN coated samples were coated only at the outer surface, what has strong influence on measured data, where mixed oxidation of coated and uncoated surface occurs. On the other hand at metallographic observation serves inner oxide layer as a good reference in coated and uncoated surface's oxide layer thickness. Thickens of outer (coated) oxide layer varies from zero to same or even higher thickness then inner oxide. Fully protected and unprotected places (with most thick oxide) are randomly distributed along outer surfaces. At fully protected places is still apparent prior β -Zr structure. Prior β -Zr phase with no oxygen stabilized zirconium alpha phase indicates no, or very low oxygen diffusion through the CrAlSiN coating into the zirconium metal. Nodular (or “blister”) pattern is quite common on outer surface and indicates places, where protective coating mechanical fails and steam starts to penetrate zirconium alloy through cracks in coating.

CrAlSiN Hydrogen concentration in Zr metal measured by IGF

Knowing the area, initial weight and final weight of each sample, along with the bulk hydrogen concentration, the hydrogen pickup fraction was calculated. The initial hydrogen concentration of 8 ppm was used in the hydrogen pickup calculations. Measured values are summarized in Table 18.

Table 18: Hydrogen concentrations measured by IGF

Temp. [°C]	Time [min]	Hydrogen concentration	
		[ppm]	
		Coated	Reference
CrAlSiN on Zry-2			
1200	2 x 30	141,4	62,3
1100	40	388,8	612,4
1000	60	1528,4	282,85

CrAlSiN EDS and SEM observations

Sample composition of steam exposed sample (1100 °C, 60 minutes, water-quenched) was analyzed via EDS analysis on different places on polished sample cross-section. EDS analysis on coating is in (Tables 19, 20, 21) Spectrum 2, 3, and 4 corresponds to CrAlSiN coating and Spectra 6 and 8 corresponds to underlying zirconium dioxide. All spectra shows high content of carbon (around 50 atm%), this high carbon content is probably caused by contamination of polished sample by resin dust and residuals brushing and polishing material.

Table 19: EDS Spectrum - Element analysis

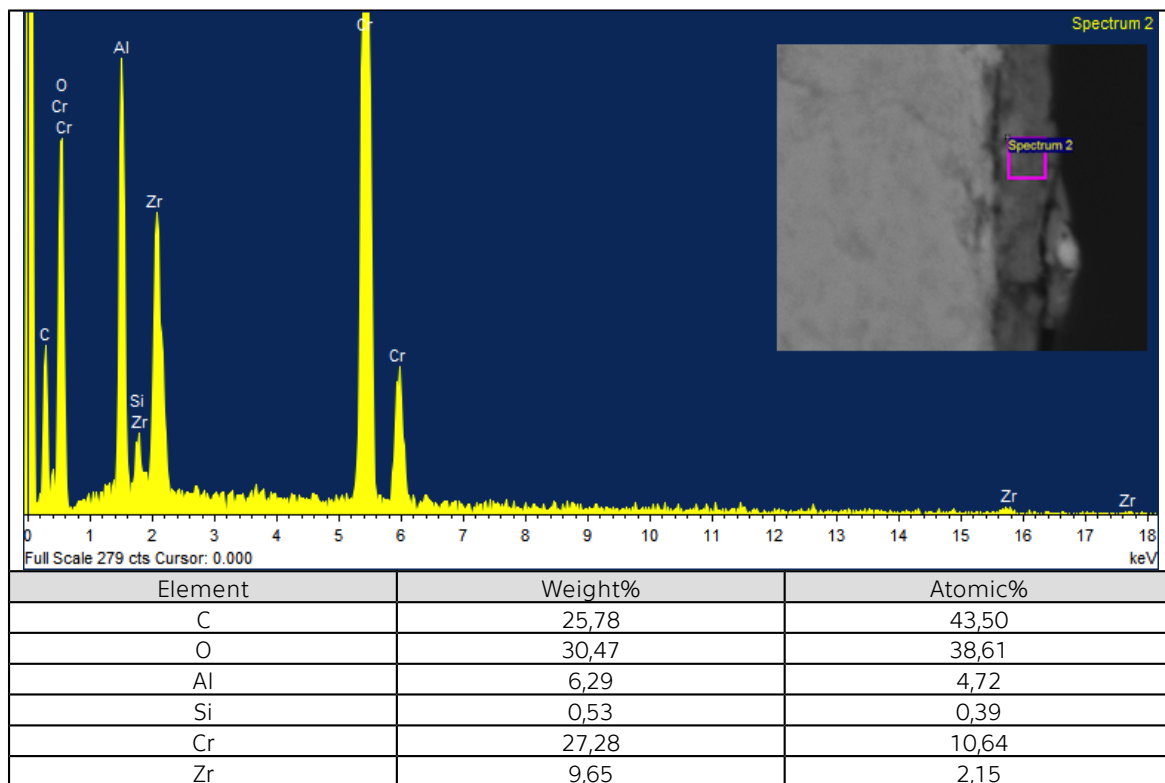


Table 20: EDS analysis of exposed CrAlSiN coating

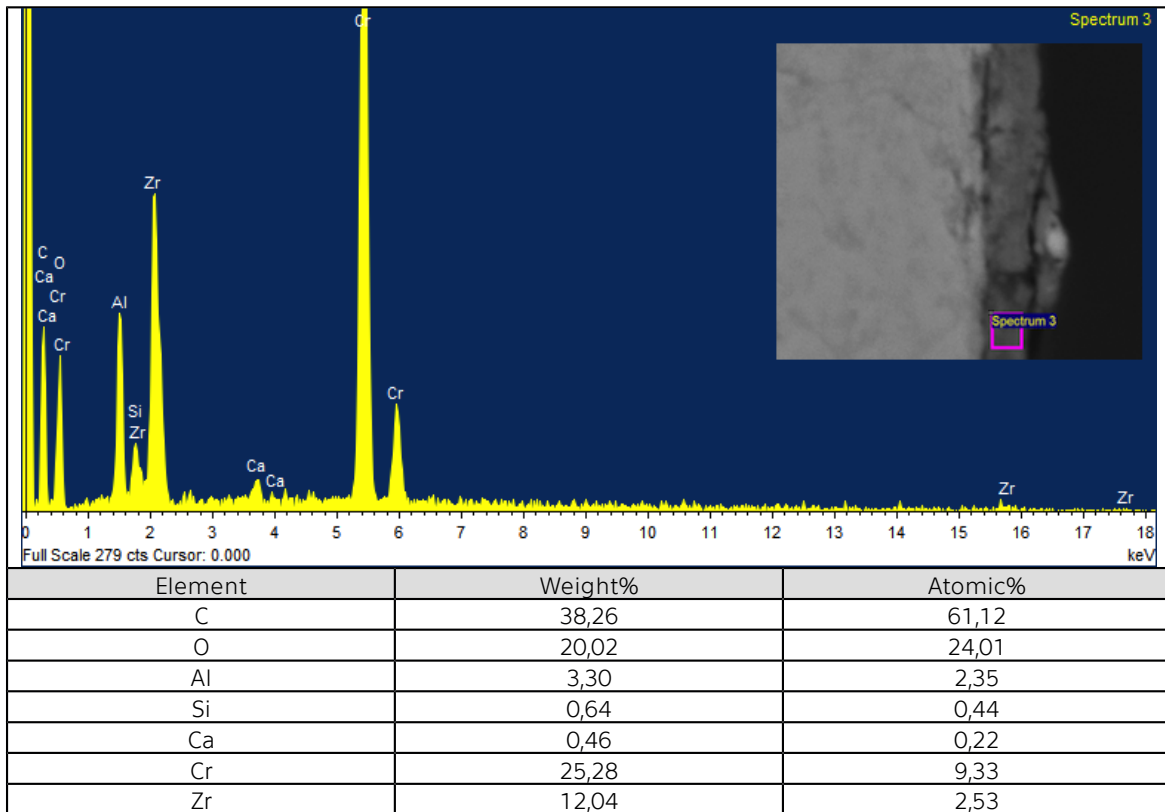
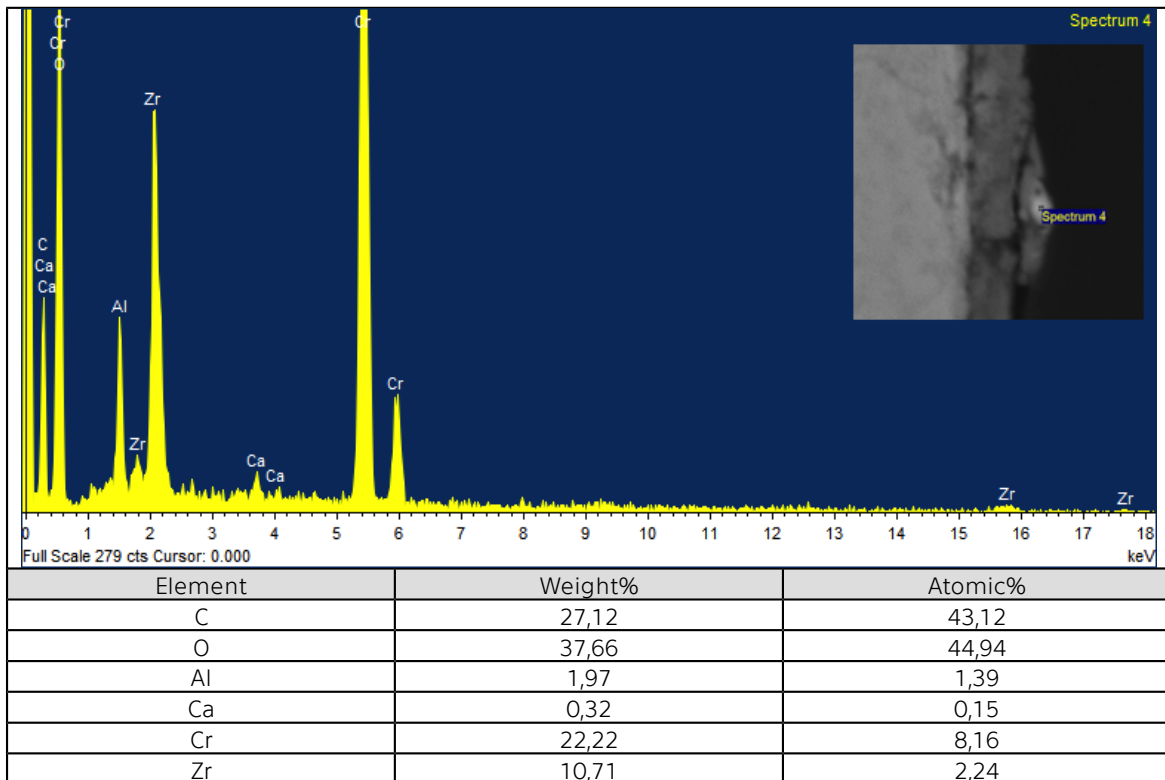
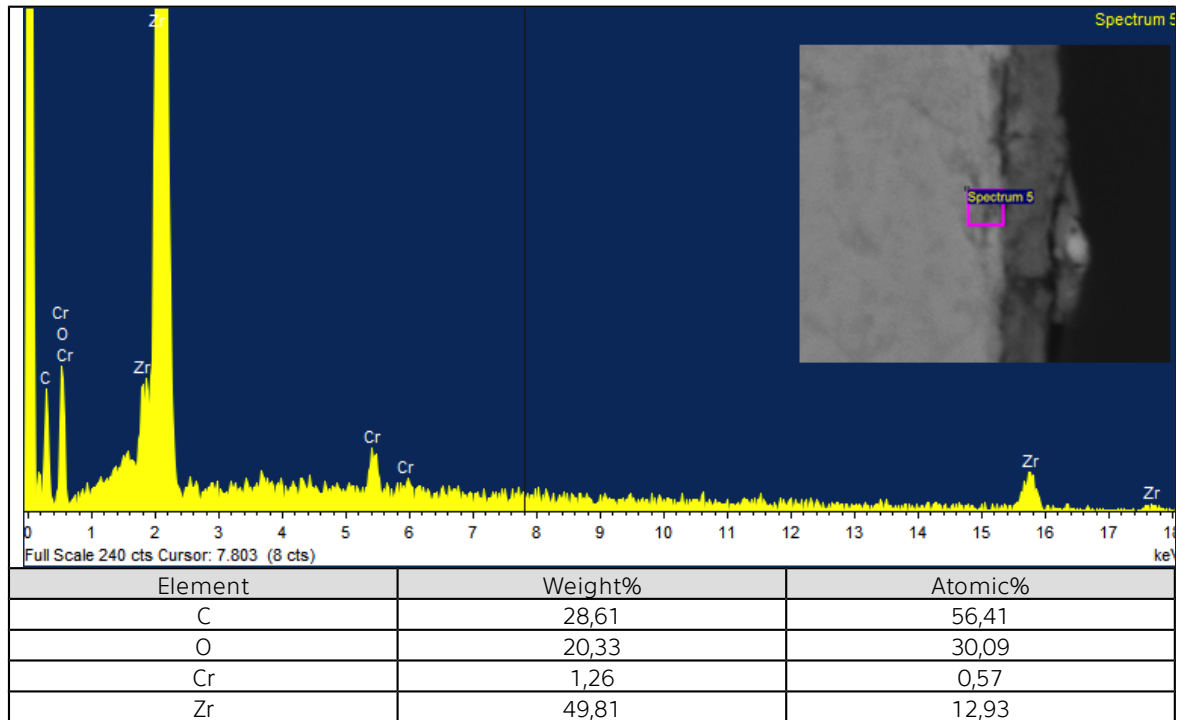


Table 21: EDS analysis of exposed CrAlSiN coating



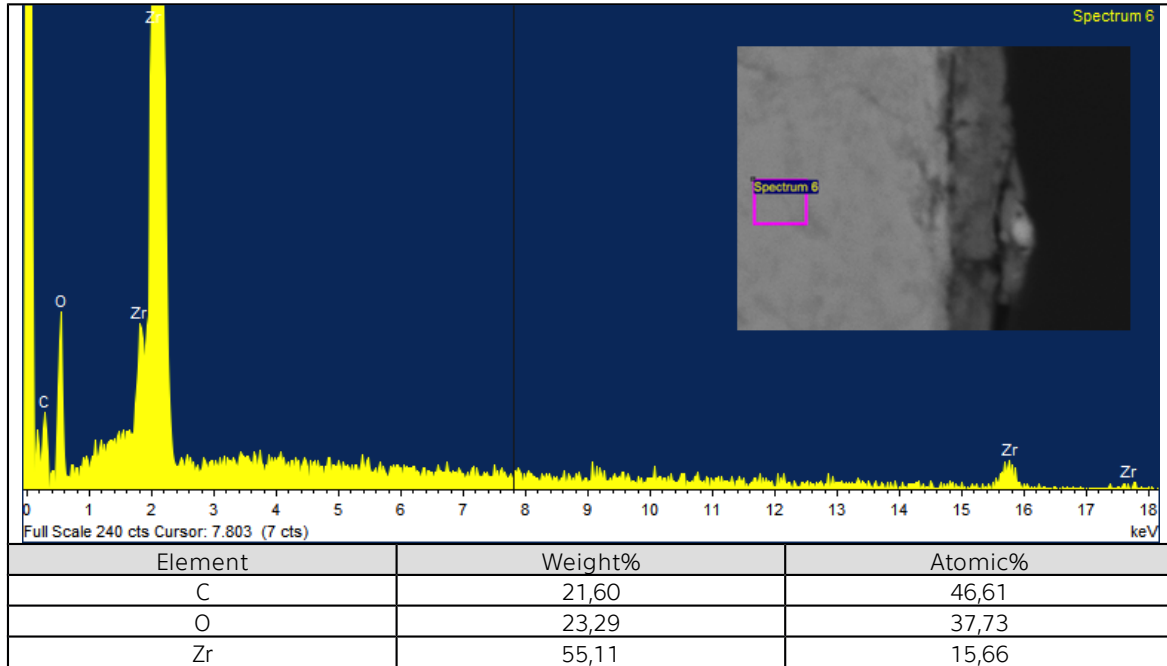
As there is no nitrogen present in the formal CrAlSiN coating is obvious that all coating has been oxidized, replacing chromium, aluminum and silicon nitrides with chromium oxide, alumina and silica. Average ratio among Cr: Al : Si is 10 : 3,5 : 0,4 3 which roughly corresponds with initial ratio 58,7% (Cr), 36,5 % (Al) and 4,8 % (Si). Source of contamination with calcium is not known, this could be connected either with coating or sample preparation. Nevertheless this contamination can be considered as negligible due it's very low concentrations.

Table 22: EDS analysis of exposed CrAlSiN coating



Spectrum 5 (Table 22) measured just underneath the CrAlSiN coating, shows no, or very limited diffusion of coating element (Cr, Si, Al) into the underlying zirconium material.

Table 23: EDS analysis of exposed CrAlSiN coating



Composition of Spectrum 8 (Table 23) is typical for zirconium dioxide, as oxygen atomic concentration is two times higher than zirconium, corresponding with stoichiometric ratio.

Table 24: CrAlSiN SEM results at 1100 °C / 60 min. samples

CrAlSiN– 1100 °C, 60 min, water-quenched	
<ol style="list-style-type: none"> 1. Uniform oxide layer on inner surface 2. Zr alloy 3. Non-uniform oxide layer on outer surface – variable oxide layer thickness due to different oxidation kinetics caused by failing coating 	<p>OUTER SURFACE DETAIL</p> <ol style="list-style-type: none"> (1) zirconium oxide (2) oxidized coating

It is obvious from SEM cross-section (Table 24), that CrAlSiN coatings is present on sample surface after 1100 °C / 60 minutes test in steam environment, with final water quench into ice cold water. Non-uniform thickness of the oxide layer under the CrAlSiN coating corresponds with different oxidation kinetics at different areas caused by developing oxidation with oxygen going through cracks in coating.

7 Published papers

7.1 Nanosized polycrystalline diamond cladding for surface protection of zirconium nuclear fuel tubes.

I. Kratochvílová, R. Škoda, J. Škarohlíd, P. Ashcheulov, A. Jäger, J. Racek, A. Taylor, L. Shao, *Journal of Materials Processing Technology* 214 (2014), pp 2600 – 2605. [A5]

A 300 nm thick polycrystalline diamond layer has been used for protection of zirconium alloy nuclear fuel cladding against undesirable oxidation with no loss of chemical stability and preservation of its functionality. Deposition of polycrystalline diamond layer was carried out using microwave plasma enhanced chemical vapor deposition apparatus with linear antenna delivery (which enables deposition of PCD layers over large areas). Polycrystalline diamond coated zirconium alloy fuel tubes were subjected to corrosion tests to replicate nuclear reactor conditions, namely irradiation and hot steam oxidation. Stable radiation tolerance of the polycrystalline diamond layer and its protective capabilities against hot steam oxidation of the zirconium alloy were confirmed. Finally, the use of polycrystalline diamond layers as a sensor of specific conditions (temperature/pressure dependent phase transition) in nuclear reactors is suggested.

Techniques of PCD protective layer deposition (using CVD) and basic characterization (using Raman spectroscopy) are introduced in this paper. First results from high temperature oxidation in simple furnace are presented. These results were first steps to complex fuel cladding protective coating as satisfactory high temperature oxidation protective capabilities were shown together with satisfactory radiation resistance, measured by Ion Beam Irradiation.

7.2 Thin polycrystalline diamond films protecting zirconium alloys surfaces: From technology to layer analysis and application in nuclear facilities

P. Ashcheulov, R. Škoda, J. Škarohlíd, A. Taylor, L. Fekete, F. Fendrych, R. Vega, L. Shao, L. Kalvoda, S. Vratislav, V. Cháb, K. Horáková, K. Kůsová, L. Klimša, J. Kopeček, P. Sajdl, J. Macák, S. Johnson, I. Kratochvílová, *Applied Surface Science* 359 (2015), 621–628 [A3]

Zirconium alloys can be effectively protected against corrosion by polycrystalline diamond (PCD) layers grown in microwave plasma enhanced linear antenna chemical vapor deposition apparatus. Standard and hot steam oxidized PCD layers grown on Zircaloy2 surfaces were examined and the specific impact of polycrystalline Zr substrate surface on PCD layer properties was investigated. It was found that the presence of the PCD coating blocks hydrogen diffusion into the Zircaloy2 surface and protects Zircaloy2 material from degradation. PCD anticorrosion protection of Zircaloy2 can significantly prolong life of Zircaloy2 material in nuclear reactors even at temperatures above Zr phase transition temperatures.

This paper concentrates more deeply on properties of deposited PCD layer, in as-prepared and steam-exposed form. Impedance spectroscopy, Raman spectroscopy and Neutron diffraction, were

used to characterize properties of deposited coating and underlying substrate. X-ray photo electron spectroscopy, SEM and AFM were used for surface morphology characterization.

7.3 High temperature oxidation of polycrystalline diamond coated zirconium alloys

J. Škarohlíd, R. Škoda, I. Kratochvílová, Proceedings of the 2016 24th International Conference on Nuclear Engineering ICONE24, June 26-30, 2016, Charlotte, North Carolina [A6]

Polycrystalline diamond coating is a promising possibility for prevention, or reduction of high temperature oxidation of zirconium alloys and decrease corrosion rate of zirconium alloy during standard operation. Zirconium alloys are widely used as cladding and construction material in almost all types of nuclear reactors, where usually creates a barrier between nuclear fuel and cooling water in the primary circuit. Hydrogen and considerable amount of heat is released during steam oxidation that may occur in an eventual accident. In this paper zirconium alloy was covered by polycrystalline diamond layer using Plasma Enhanced Linear Antennas Microwave Chemical Vapor Deposition system reactor. X-Ray Diffraction and Raman spectroscopy measurements confirmed coverage of the surface area with crystalline and amorphous carbon layer. Characterizations (Raman spectroscopy) were done for zirconium alloy covered with polycrystalline diamond layer before and after high temperature steam exposure. Weight increase and hydrogen release were measured during steam exposure.

This conference paper concentrates primary to complex High Temperature Oxidation observations. Online TG and outgoing gas analyses were performed on PCD coated samples at temperatures in range from 900 °C to 1400 °C.

7.4 Nanocrystalline diamond protects Zr cladding surface against oxygen and hydrogen uptake: Nuclear fuel durability enhancement

J. Škarohlíd, P. Ashcheulov, R. Škoda, A. Taylor, R. Čtvrtlík, J. Tomáščík, F. Fendrych, J. Kopeček, V. Cháb, S. Cichoň, P. Sajdl, J. Macák, P. Xu, J. M. Partezana, J. Lorinčík, J. Prehradná, M. Steinbrück, I. Kratochvílová, Scientific Reports [A2]

In this work, we demonstrate and describe an effective method of protecting zirconium fuel cladding against oxygen and hydrogen uptake at both accident and working temperatures in water-cooled nuclear reactor environments. Zr alloy samples were coated with nanocrystalline diamond (NCD) layers of different thicknesses, grown in a microwave plasma chemical vapor deposition apparatus. In addition to showing that such an NCD layer prevents the Zr alloy from directly interacting with water, we show that carbon released from the NCD film enters the underlying Zr material and changes its properties, such that uptake of oxygen and hydrogen is significantly decreased. After 100–170 days of exposure to hot water at 360 °C, the oxidation of the NCD-coated Zr plates was typically decreased by 40%. Protective NCD layers may prolong the lifetime of nuclear cladding and consequently enhance nuclear fuel burn-up. NCD may also serve as a passive element for nuclear safety. NCD-coated ZIRLO claddings have been selected as a candidate for Accident Tolerant Fuel in commercially operated reactors in 2020.

Paper summarizing all previous results and introducing new results from Long-term exposures – simulating reactor operation conditions. Advanced characterisation methods as Nano-Esca and SIMS were used for detailed coating and underlying zirconium alloy characterisation. Principles of protective function of PCD coating is described.

8 Comments and Outlook

I would like to present more personal insight in coatings and ATF problematics, not exactly supported by measured “hard” data and peer-reviewed journals, but belonging to more unofficial atmosphere, like having beer and fruitful discussion with colleagues after official conference banquet. I would like to start this few lines with quotation of Dr. Steve Johnson, our colleague and friend who was at the beginning of the co-operation with Westinghouse: “Coatings on Zr are difficult.”

LOCA sequences (high and low pressure) are very complex and complicated phenomena, depending on many different variables, so addition of anti-corrosion barrier on the surface of the cladding still brings some questions. More data and operation experience are still needed for most of newly developed coatings, whereas most material has never been used in nuclear reactors yet. What surprises can be found with adding new material in fuel cladding (erbium in this case) is nicely described in [35]. In this case, what seems to be an easy task, erbium starts to “do absolutely crazy stuff” (citing Dr. Brachet) which in the end broke neck of this idea in the beginning. Other studies [36] showed that Cr coatings significantly (in order of several minutes!) prolongs quenching time (when steam blocks water to reach to overheated tube), this is thermomechanic's nightmare – having core full of cooling water, but not cooling at all! Not only this microscopic-material aspects has to be considered but also the macroscopic-whole reactor / power plant aspects. As the ATF coating could delay initiation of high temperature oxidation to late stages of the accident, what is generally considered as beneficial, it also means that the most intensive oxidation (with heat and hydrogen release) should start in phase with already empty tanks for ECCS's, more damaged technology (e.g. from fire, tsunami,...) and already tired personal.

And what is the future of coated Zr alloys? Hard to say, but few possibilities already exists. ATF should be introduced to commercial reactors, according conditions of DOE, in 2020. At this moment the most promising candidates has been selected by Westinghouse and are tested in Halden reactor. PCD is also among candidates! Metallic (chromium) coating seems to be most likely choice nr. one, while still having some problems. Titanium based nitrates and MAX phase are the worst option, according my opinion, while Cr based material performs much better (also according other results¹⁰). Also adding more ceramic layers (multilayered Ti or Cr based MAX phases) and increase of coating's thickness (more than 6 μm) seems to be a wrong way, leading to enormous coating peeling. I think the most promising way are multilayer coatings, with outer impenetrable ceramic layer (chromium and / or aluminium based nitrates or carbides) with softer inner layer (carbon (PCD) based). This soft layer will compensate differences in hoop strain and prevent outer surface from cracking. PCD layers seems to work perfectly in this manner. Realization of such a layer is our next step. Other coating possibilities are: inner coatings of Zr cladding, which promises improvements in PCI and PCMI, optimization of heat transfer and gap behaviour, opening whole

10 Chongchong Tang and Martin Steinbrück (both from KIT) – personal communication

new playground for research. Addition of burnable poisons to cladding materials seems as beautiful idea, but will lead to more new discoveries (usually concept neck-breaking) , then to functional design.

9 Conclusions

In this work, a new anticorrosion strategy for Zr nuclear fuel cladding tubes was presented and explained. Two different coatings were used, one which could be beneficial at temperatures above 800 °C (accident tolerant fuel) and the other one for the operational conditions at lower temperatures 300 – 400 °C. Especially, this work deals with a protection of zirconium fuel cladding against corrosion in LWR by coating of polycrystalline diamond and chromium-aluminium-silicon nitrate layers. It was shown that Zr alloy surfaces can be effectively protected against oxygen and hydrogen uptake at both accident and operation temperatures in LWR's by coating the Zr surface by PCD layer or chromium-aluminium-silicon nitrate each in the specific way and for a specific purpose.

After long-term processing (for up to 195 days) in 360 °C hot water (in accordance with ASTM standard procedures), a larger relative weight gain was found for Zr alloy samples with unprotected surfaces than for PCD-coated samples. The relative weight gain of the PCD-coated samples was decreased by 35 – 55 %. This decrease was attributed to the restricted oxidation and hydrogen uptake of the PCD-protected samples. PCD layers were also found to protect Zr alloy surfaces against hydrogen uptake: the average hydrogen concentration was markedly greater for uncoated samples. For high-temperature steam exposures (1100 °C, 1200 °C), the uptake of hydrogen into the unprotected material was an order of magnitude higher than that indicated by the hydrogen concentrations in the PCD-protected samples.

Thicker (700 nm and 500 nm) PCD layers provided stronger protection of ZIRLO plates and tubes against oxidation than thinner (300 nm) PCD layers. The best protective effect was achieved by 700 nm PCD coatings on Zr plates (low tin Zirlo®): the surface oxidation of these samples after long term processing (360 °C, from 20 days to 40 days) was decreased by more than 50 %. The higher protective efficacy achieved by the PCD coatings for plates compared with tubes was attributed to the inner surfaces of the tubes not being fully covered with PCD, whereas in the case of plates mounted vertically in the deposition chamber, all surfaces were covered with homogeneous PCD layers. Notably, the MW-LA-PECVD apparatus, if scaled up as necessary, would be capable of homogeneously coating the full lengths of nuclear rods.

This protection of PCD occurs at three basic levels: 1. the PCD protects the Zr alloy surface from directly interacting with water molecules; 2. carbon atoms penetrate into the Zr alloy from the PCD, thus creating carbides and becoming incorporated into ZrO₂, thereby making conditions less favourable for subsequent O and H uptake; and 3. the carbon from the PCD changes the electrical properties of the ZrO₂ and creates less favourable conditions for Zr oxidation at the ZrO₂/Zr interface. The specific anticorrosion function of PCD coating of Zr alloy prepared in MW-LA-PECVD apparatus was patented in [A4].

Major points concerning Zr alloys new anticorrosion strategy using PCD coating are:

- Zr alloys used as nuclear fuel cladding and other structural elements in nuclear reactors covered by compact and homogeneous PCD layers consisting of sp^3 and sp^2 carbon phases with a high crystalline diamond content and low roughness are strongly protected against corrosion in hot steam / hot water environment.
- After ion beam irradiation (10 dpa, 3 MeV Fe^{2+}) the diamond layer shows satisfactory structural integrity with both sp^3 and sp^2 carbon phases.
- Exposure of the PCD coated Zr alloy to hot steam (1100 °C, 30 min) caused the infusion of both oxygen and Zr substrate atoms into the protective layer. The protective layer has a constitution of Zr carbide and underwent a phase change from diamond to sp^2 phase carbon.
- After 1100 °C steam oxidation of PCD coated Zr alloy samples, zirconium atoms are incorporated into PCD layer – first fingerprints of zirconium carbide layer were forming.
- The Zr alloy under the PCD protective layer after high temperature steam oxidation differed from the original alloy material composition only very slightly (XPS), proving that the PCD coating increases the material resistance to high temperature oxidation.
- The larger weight gain of unprotected Zr fuel cladding can be attributed to the greater oxygen intake compared to PCD covered/protected Zr fuel cladding.
- In addition to the fact that PCD layers prevent the surface of Zr alloys from direct interaction with hot water, carbon released from the PCD film enters and changes the physical properties of the underlying Zr. **This effect plays significant role in PCD protective function.**
- Compared with Zr samples protected with 500 nm of PCD, the hydrogen concentration in the unprotected Zr samples was found to be larger by one order of magnitude after 1 hour at 1100 °C in autoclave.

The above mentioned protection of Zr alloys surfaces by 300-700 nm thick polycrystalline diamond layers may be applied to a wide range of functional elements for nuclear reactors, such as fuel assembly elements. This includes, in particular, parts of commercially operated power producing light-water reactors PWR, BWR, VVER and heavy-water reactors CANDU. The described PCD protective layer can mainly prolong (40 % more) the Zr alloys lifetime in nuclear reactors under standard operation conditions. Protective PCD layers may prolong the lifetime of nuclear cladding and consequently enhance nuclear fuel burn-up. PCD layer can also to some extent serve as a passive element for nuclear safety.

Costs for PCD coverage will increase the original cost by less than 1%. Zr fuel rods covered by PCD were selected by Westinghouse as candidates for accident-proof fuel. Fuel cells covered with PCD layers are tested for long-term (until 2020) in the Halden Norwegian testing reactor. If tests are successful, PCD coverage will be commercially used to protect against corrosion of fuel cells. The results were published in impacted journals including Scien. Reports (Nature Publ. Group) and

raised the interest of Czech and foreign media (Czech Radio, HN, Service24, Energy, Economics, Materials Performance, Science Daily and others). The Czech patent was granted in 2015, patent procedures are currently underway in the EU, the USA, Japan and South Korea. PCD-coated ZIRLO claddings have been selected as a candidate for Accident Tolerant Fuel in commercially operated reactors in 2020. Fuel cells covered with PCD layers are nowadays tested for long-term (until 2020) in the Halden Norwegian reactor.

CrAlSiN coatings is homogeneous one phase layer. Thickness of the CrAlSiN coating varies between 2 – 4,5 μm . We proved its indubitable influence on high-temperature oxidation of zirconium alloy, with major points of high temperature protection mentioned below:

- CrAlSiN coated samples shows significant changes in oxidation curves – especially eliminates initial very kinetic initial oxidation phase and also overall hydrogen production and weight gain values are generally lower than for uncoated samples. CrAlSiN coating works very well at temperatures around 1000 °C, where they delayed breakaway oxidation.
- From optical microscopy is clear that CrAlSiN coating serves as full barrier against oxygen diffusion, until mechanical failure of the coating. But when the CrAlSiN coatings mechanically failed the oxidation process is even faster than in the case of unprotected samples.
- Oxidation of the primary chromium, aluminium and silicon nitrides has been detected, leading to creation of highly stable and high temperature resistant alumina and chromium oxide layers.

10 References

10.1 Autor references

[A1] Škarohlíd, J., Škoda, R., Kazda, R., (2013). Problematics of high-temperature oxidation of zirconium (in czech). *Bezpečnost jaderné energie*, **21**(59), 298-301.

[A2] Škarohlíd, J. *et al.* Nanocrystalline diamond protects Zr cladding surface against oxygen and hydrogen uptake: Nuclear fuel durability enhancement. *Scientific Reports* **7**, 1–14 (2017).

[A3] Ashcheulov, P. *et al.* Thin polycrystalline diamond films protecting zirconium alloys surfaces : From technology to layer analysis and application in nuclear facilities. *Applied Surface Science* **359**, 621–628 (2015).

[A4] Škoda, R., Škarohlíd, J., Kratochvílová, I., Taylor, A., Fendrych, F. (2015) Layer protecting the surface of zirconium alloys used in nuclear reactors. PCT WO/2015/039636, Czech patent 305059.

[A5] Kratochvílová, I. *et al.* Nanosized polycrystalline diamond cladding for surface protection of zirconium nuclear fuel tubes. *Journal of Materials Processing Technology* **214**, 2600–2605 (2014).

[A6] Škarohlíd, J., Škoda, R. & Kratochvílová, I. High temperature oxidation of polycrystalline diamond coated zirconium alloy. *International Conference on Nuclear Engineering, Proceedings, ICONE 5*, 1–4 (2016).

10.2 Other references

[1] 1. Allen, T. R., Konings, R. J. M. & Motta, A. T. Corrosion of Zirconium Alloys. in *Comprehensive Nuclear Materials* (2012). doi:10.1016/B978-0-08-056033-5.00063-X

[2] Steinbrück, M., Vér, N., & Grosse, M. Oxidation of advanced zirconium cladding alloys in steam at temperatures in the range of 600-1200 °C. *Oxidation of Metals* **76**, 215-232,(2011).

[3] Fuel Design Data, *Nuclear Engineering International*, September 2004

[4] Cox, B. Some thoughts on the mechanisms of in-reactor corrosion of zirconium alloys. *Journal of Nuclear Materials* **336**, 331–368, (2005).

[5] Brachet, J.Ch. (2015) High temperature oxidation and LOCA behaviour of Zr alloys: microstructural evolutions, consequences on the mechanical properties. *Institut national des sciences et techniques nucléaires*.

[6] Evaluation of Conditions for Hydrogen Induced Degradation of Zirconium Alloys during Fuel Operation and Storage, IAEA-TECDOC-1781

[7] Mitigation of Hydrogen Hazards in Severe Accidents in Nuclear Power Plants, IAEA-TECDOC-

- [8] Hirano, M. *et al.* Insights from review and analysis of the Fukushima Dai-ichi accident. *Journal of Nuclear Science and Technology* **49**, 1-17, (2012).
- [9] Terrani, K. A. Accident tolerant fuel cladding development: Promise, status, and challenges. *Journal of Nuclear Materials* **501**, 13–30, (2018).
- [10] Zinkle, S. J., Terrani, K. A., Gehin, J. C., Ott, L. J. & Snead, L. L. Accident tolerant fuels for LWRs: A perspective. *Journal of Nuclear Materials* **448**, 374–379, (2014).
- [11] Tang, C., Stueber, M., Seifert, H. J. & Steinbrueck, M. Protective coatings on zirconium-based alloys as accident-Tolerant fuel (ATF) claddings. *Corrosion Reviews* **35**, 141–165, (2017).
- [12] Motta, A. T., Couet, A., & Comstock, R. J. Corrosion of Zirconium Alloys Used for Nuclear Fuel Cladding. *Annual Review of Materials Research*, **45**, 311-343, (2015).
- [13] Corrosion of zirconium alloys in nuclear power plants, IAEA-TECDOC-684
- [14] United States Nuclear Regulatory Commission. NUREG/CR-6967. Cladding Embrittlement During Postulated Loss-of-Coolant Accidents. (2008).
- [15] Likhanskii, V. V. & Evdokimov, I. Review of theoretical conceptions on regimes of oxidation and hydrogen pickup in Zr-alloys 2 . Factors affecting corrosion regimes of zirconium alloys. *IAEA NCL Collection*.
- [16] Baek, J. H. & Jeong, Y. H. Breakaway phenomenon of Zr-based alloys during a high-temperature oxidation. *Journal of Nuclear Materials* **372**, 152–159 (2008).
- [17] Young, D. High Temperature Oxidation and Corrosion of Metals. *Elsevier Corrosion Series*
- [18] Pawel, R. E., Cathcart, J. V., McKee, R. A. (1979) The Kinetics of Oxidation of Zircaloy-4 in Steam at High Temperatures. *J. Electrochem. Soc.* **126**, 1105-1111 (1979).
- [19] Baker, L., Just, J. C. Studies of Metal-Water Reactions at High Temperatures; III. Experimental and Theoretical Studies of the Zirconium-Water Reaction, ANL-6548, (1962).
- [20] Pshenichnikov, A. & Stuckert, J. Orientation relationships of delta hydrides in zirconium and Zircaloy-4. *International Conference on Nuclear Engineering, Proceedings, ICONE* (2016).
- [21] Puls, M. P. Review of the thermodynamic basis for models of delayed hydride cracking rate in zirconium alloys. *Journal of Nuclear Materials*, **393**, 350-367, (2009).
- [22] Couet, A., Motta, A. T., & Comstock, R. J. Hydrogen pickup measurements in zirconium alloys: Relation to oxidation kinetics. *Journal of Nuclear Materials*, **451**, 1-13, (2014).
- [23] Bragg-Sitton, S., Development of advanced accident-tolerant fuels for commercial LWRs. *Nuclear News*, **4**, 83–91, (2014).
- [24] Brachet, J. C. *et al.* Behavior under LOCA conditions of Enhanced Accident Tolerant Chromium Coated Zircaloy-4 Claddings. *Top Fuel 2016 Proceedings* (2016).

- [25] Sung, J. H. *et al.* Fretting damage of TiN coated zircaloy-4 tube. *Wear* **250**, 658–664, (2001).
- [26] Pu, J.-C. *et al.* High-temperature oxidation behaviors of CVD diamond films. *Applied Surface Science*. **256**(3), 668-673, (2009).
- [27] Mercks, D. *et al.* Mechanical and tribological properties of Cr-N and Cr-Si-N coatings reactively sputter deposited. *Surface and Coatings Technology* **200**, 403–407 (2005).
- [28] Rafaja, D. *et al.* Microstructure development in Cr-Al-Si-N nanocomposites deposited by cathodic arc evaporation. *Surface and Coatings Technology* **201**, 2835–2843 (2006).
- [29] Polcar, T. & Cavaleiro, A. High-temperature tribological properties of CrAlN, CrAlSiN and AlCrSiN coatings. *Surface and Coatings Technology* **206**, 1244–1251 (2011).
- [30] Fendrych, F. *et al.* Growth and characterization of nanodiamond layers prepared using the plasma-enhanced linear antennas microwave CVD system. *Journal of Physics D: Applied Physics*. **43**(37), (2010)
- [31] ASTM G2 / G2M – 06 Standard Test Method for Corrosion Testing of Products of Zirconium, Hafnium, and Their Alloys in Water at 680°F [360°C] or in Steam at 750°F [400°C].
- [32] Chen, Y. *et al.* The electrochemistry of zirconium in aqueous solutions at elevated temperatures and pressures. *Journal of Nuclear Materials* **348**, 133-147 (2006).
- [33] Krausová, A. *et al.* In-situ electrochemical study of Zr1Nb alloy corrosion in high temperature Li+containing water. *Journal of Nuclear Materials* **467**, 302-310 (2015).
- [34] Meisterjahn, P. *et al.* Electrochemical and XPS measurements on thin oxide films on zirconium. *J. Electroanal. Chem.* **217**, 159-185 (1987).
- [35] Brachet, J. C. *et al.* Microstructure and properties of a three-layer nuclear fuel cladding prototype containing erbium as a neutronic burnable poison. *ASTM Special Technical Publication STP 1543*, 184–224 (2015).
- [36] In, W. K, Pool Boiling Critical Heat Flux and Quenching Experiments using Oxidized Zircaloy Surface, In *19th QUENCH Meeting Proceedings*, (2013).

11 Supplementary

Supplementary S1

An evaluation of the fuel system design should be presented for the physically feasible combinations of chemical, thermal, irradiation, mechanical, and hydraulic interaction. Evaluation of these interactions should include the effects of normal reactor operamismatchtions, anticipated transients without scram, and postulated accidents. The fuel system design evaluation should include the following (cladding concerning evaluations are highlighted):

i. Cladding

- a) Vibration analysis.
- b) Fuel element internal and external pressure and cladding stresses during normal and accident conditions with particular emphasis on temperature transients or depressurization accidents.
- c) Potential for chemical reaction, including hydriding, fission product attack, and crud deposition.
- d) Fretting and crevice corrosion.
- e) Stress-accelerated corrosion.
- f) Cycling and fatigue.
- g) Material wastage due to mass transfer.
- h) Rod bowing due to thermal, irradiation, and creep dimensional changes
- i) Consequences of power-coolant mismatch.
- j) Irradiation stability of the cladding.
- k) Creep collapse-and creepdown.

ii. Fuel

- a) Dimensional stability of the fuel,
- b) Potential for chemical interaction, including possible waterlogging rupture,
- c) Thermal stability of the fuel, including densification, phase changes, and thermal expansion,
- d) Irradiation stability of the fuel, including fission product swelling and fission gas release.

iii. Fuel Rod Performance

- a) Fuel-cladding mechanical interaction.

- b) Failure and burnup experience, including the thermal conditions for which the experience was obtained for a given type of fuel and the results of long-term irradiation testing of production fuel and test specimens,
 - c) Fuel and cladding temperatures, both local and gross, with an indication of the correlation used for thermal conductivity, gap conductance as a function of burnup and power level, and the method of employing peaking factors,
 - d) An analysis of the potential effect of sudden temperature transients on waterlogged elements or elements with high internal gas pressure,
 - e) An analysis of temperature effects during anticipated operational transients that may cause bowing or other damage to fuel, control rods, or structure,
 - f) An analysis of the energy release and potential for a chemical reaction should physical burnout of fuel elements occur,
 - g) An analysis of the energy release and resulting pressure pulse should waterlogged elements rupture and spill fuel into the coolant,
 - h) An analysis of the behavior of fuel rods in the event coolant flow blockage is predicted.*
- iv. Spacer Grid and Channel Boxes
- a) Dimensional stability considering thermal, chemical, and irradiation effects,
 - b) Spring loads for grids.
- v. Fuel Assembly
- a) Loads applied by core restraint system,
 - b) Analysis of combined shock (including LOCA) and seismic loading,
 - c) Loads applied in fuel handling, including misaligned handling tools.
- vi. Reactivity Control Assembly and Burnable Poison Rods
- a) Internal pressure and cladding stresses during normal, transient, and accidental conditions,
 - b) Thermal stability of the absorber material, including phase changes and thermal expansion,
 - c) Irradiation stability of the absorber material, taking into consideration gas release and swelling,
 - d) Potential for chemical interaction, including possible water-logging rupture.

Supplementary 2: Detailed DB LOCA description

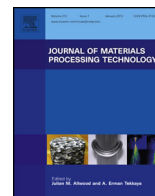
- The reactor has been operating for an infinite period of time at an assumed slight overpower condition. No power or other transient precedes the accident.
- Peak core power density or linear power generation is at the maximum allowable value.

- A double-ended rupture of one primary coolant loop is assumed (largest existing pipe)
PWR: rupture of cold leg imposes most severe conditions
BWR: rupture of a recirculation loop
 Remaining intact loops continue their operation as dictated by available electric supply or stored rotational energy.
- Off-site power is lost upon initiation of the accident and is restored after several days.
- Reactor scram systems need not contribute to the nuclear shut down because voiding of the core provides sufficient negative reactivity for shutdown.
- The reactor is isolated after the initiation of the accident, i.e. the regular heat sink is removed.
PWR: Upon initiation of the accident the steam generators are isolated on the secondary side by closing the steam supply valves and the feedwater valves.
BWR: Upon receipt of a reactor-vessel low-water signal the main steam isolation valves close within 10 seconds. Feedwater flow ramps to zero within four seconds.
- EECS are actuated automatically by appropriate signals. No corrective operator action is assumed for the first 10 minutes following initiation of the accident.
- A single failure criterion is applied to the reactor system whereby an additional fault is postulated which may render inoperative any one of the following:
 - Mechanical active components (e.g. pump) Active or passive electrical components
 - Events in the reactor pressure vessel during a large-break LOCA. a) Normal operation; b) blowdown phase; c) refill phase; d) reflood phase

Supplementary 3: Event Categories

Cat.	Description	Frequency / Reactor	Examples of events
1	Conditions that occur regularly in normal operation	~ 10	<ul style="list-style-type: none"> • Bringing the reactor to full power
2	Faults that are expected during the life of the plant: Anticipated moderately frequent events requiring safety response	~1	<ul style="list-style-type: none"> • Loss of external grid • Loss of feed water • Loss of reactor coolant pump
3	Faults not expected during life of a particular plant: Anticipated infrequent events requiring safety response	~10 ⁻²	<ul style="list-style-type: none"> • Small LOCA • Valves open
4	Improbable events not expected to occur in the nuclear industry but provided for by the design	~10 ⁻⁴	<ul style="list-style-type: none"> • Large LOCA • Main steam line break
5	Extremely improbable events not provided for in the design of the plant	~10 ⁻⁶	<ul style="list-style-type: none"> • LOCA without ECCS • Transient with total loss of On- and Off- site power

PUBLISHED PAPERS



Nanosized polycrystalline diamond cladding for surface protection of zirconium nuclear fuel tubes



I. Kratochvílová^{a,d,*}, R. Škoda^b, J. Škarohlíd^b, P. Ashcheulov^{a,d}, A. Jäger^a, J. Racek^a, A. Taylor^a, L. Shao^c

^a Institute of Physics, Academy of Sciences Czech Republic v.v.i, Na Slovance 2, CZ-182 21 Prague 8, Czech Republic

^b Czech Technical University in Prague, Faculty of Mechanical Engineering, Technická 4, CZ-160 07 Prague 6, Czech Republic

^c Texas A&M University, Department of Nuclear Engineering TAMU-3133, College Station, TX 77843, USA

^d Faculty of Nuclear Physics and Physical Engineering, Czech Technical University in Prague, Žitkova 1, CZ-160 00 Prague 6, Czech Republic

ARTICLE INFO

Article history:

Received 5 February 2014

Received in revised form 5 May 2014

Accepted 6 May 2014

Available online 13 May 2014

Keywords:

Polycrystalline diamond film

Nuclear fuel cladding protection

Microwave plasma enhanced chemical vapor deposition

ABSTRACT

A 300 nm thick polycrystalline diamond layer has been used for protection of zirconium alloy nuclear fuel cladding against undesirable oxidation with no loss of chemical stability and preservation of its functionality. Deposition of polycrystalline diamond layer was carried out using microwave plasma enhanced chemical vapor deposition apparatus with linear antenna delivery (which enables deposition of PCD layers over large areas). Polycrystalline diamond coated zirconium alloy fuel tubes were subjected to corrosion tests to replicate nuclear reactor conditions, namely irradiation and hot steam oxidation. Stable radiation tolerance of the polycrystalline diamond layer and its protective capabilities against hot steam oxidation of the zirconium alloy were confirmed. Finally, the use of polycrystalline diamond layers as a sensor of specific conditions (temperature/pressure dependent phase transition) in nuclear reactors is suggested.

© 2014 Elsevier B.V. All rights reserved.

1. Introduction

Zirconium alloys (with a common subgroup trademarked Zircaloy2) are a material used in all modern hot steam water cooled commercial nuclear reactors. Such a material must comply with stringent material requirements; Zinkle and Was (2013) described the recent material challenges of nuclear-reactor materials. Zircaloy2 is a material with very useful properties for nuclear facilities applications: it has a low absorption cross-section of thermal neutrons, high ductility, hardness and corrosion resistance. However, it also has significant weakness, as it reacts with water steam, as recently reviewed by Burns et al. (2012). During this (oxidative) reaction hydrogen gas is released; the oxidation rate of such a reaction was studied by Causey et al. (2006). The released hydrogen then partly diffuses into the alloy forming zirconium hydrides, which are less dense and are mechanically weaker than the original Zircaloy2 material. Their formation results in blistering and finally cracking of the cladding, mechanisms of which were

studied by Puls (1990). Moreover, a large production of hydrogen gas can result in a hydrogen-air chemical explosions (as seen in the recent Fukushima accident, the reasons and effects of which are thoroughly analyzed by Hirano et al. (2012) and Högborg (2013)). As these effects are surface related, a solution to the problem, namely how to fully utilize the advantages of the bulk of the zirconium-based material and to reinforce its surface chemical resistance, is to cover the surface with a thin film of a protective substance. Recently, many materials have been applied to protect zirconium alloy surfaces from destruction, but without any significant success. For example, Steinbruk et al. (2011) describes newly developed materials such as Zircaloy-4, or Bryan US patent EP 0673539 proposed a wear-resistant coating comprising a ceramic material with glass.

In this work, we provide a proof of concept for a new strategy of zirconium-alloy nuclear fuel cladding (NFC) surface protection, by the use of polycrystalline diamond (PCD) film. PCD films have been grown in a microwave plasma enhanced chemical vapor deposition apparatus with linear antenna delivery system (MW-LA-PECVD) as described in Fendrych et al. (2010). Polycrystalline diamond layers consist of crystalline (sp^3) and amorphous (sp^2) carbon phases. Diamond has excellent material properties, it withstands very high temperatures, has high thermal conductivity and low chemical reactivity and does not degrade over time (studied by Kratochvílová

* Corresponding author at: Institute of Physics, Academy of Sciences Czech Republic v.v.i, Na Slovance 2, CZ-182 21 Prague 8, Czech Republic.
Tel.: +420 723814810.

E-mail address: krat@fzu.cz (I. Kratochvílová).

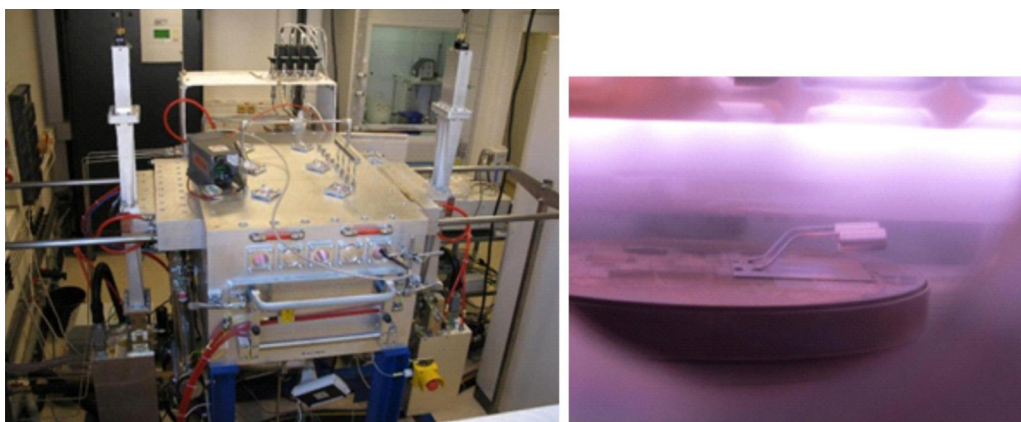


Fig. 1. MW-LA-PECVD deposition chamber and mounting of the Zircaloy2 sample tubes ensuring the growth of PCD layer completely around the tubes' circumference.

et al. (2011) and Petráková et al. (2012)). Therefore, it has already been considered as a material of choice for a large variety of applications. Such applications were described by May (2000) and Balmer et al. (2009) in their reviews and include high power/high temperature or radiation-hard electronics and detectors.

Pure carbon has perfect neutron cross-section properties. Moreover, polycrystalline diamond layers consisting of crystalline (sp^3) and amorphous (sp^2) carbon phases have suitable thermal expansion. To the best of our knowledge, diamond has never been studied as a possible protective coating for NFC.

Various diamond films are now being used in industry for the protection of materials and devices, usually enhancing the mechanical properties. The combination of the already well-established usage and the simple, but novel idea we have put forward implies a significant application potential of diamond coated zirconium nuclear fuel claddings.

2. Experimental

2.1. Growth of PCD

Prior to growth Zircaloy2 tubular samples (length: 25 mm and diameter: 10 mm) were immersed in a water based dispersion containing nanodiamond particles (NanoAmando[®]), which act as seeds and therefore induce sites for PCD growth. Samples were then mounted onto a holder to ensure that the whole circumference of the tube is exposed to the plasma, and placed into the microwave plasma enhanced chemical vapor deposition apparatus with linear antenna delivery (MW-LA-PECVD) chamber. The temperature of the Zircaloy2 samples was measured during the diamond deposition by a Williamson Pro 92-38 infrared thermometer capable of measurements in the 450–1000 °C range.

The MW-LA-PECVD apparatus is capable of producing both continuous wave (at a maximum of 3 kW) and tunable pulsed microwaves (at a maximum of 10 kW). Microwaves are delivered into the growth chamber in a linear form by four pairs of antennas enclosed in quartz envelopes. The plasma sources are arranged parallel to one another above the substrate holder which enables deposition of PCD onto substrates with sizes, currently, as large as 50 cm × 30 cm, using a gas mixture of $H_2 + CH_4 + CO_2$ at low process pressures (<1 mBar) as described by Taylor et al. (2011). The MW-LA-PECVD system enables a surface wave to be sustained linearly along the antennas, therefore the size of microwave discharge is not limited by the wavelength of inputted microwave power, in addition to this the system is of a modular design (in all axis). These factors therefore can, in the future, facilitate coating of actual full lengths of fuel cladding tubes (3–4 m), see Liehr et al. (2006). Photographs of the system and the sample holder are presented in Fig. 1.

Owing to its diffuse plasma properties, due to a combination of low electron temperature (1.5 eV), high plasma density ($>10^{11}/cm^3$) (see Tsugawa et al., 2006) low power density and high atomic hydrogen concentrations (details see Vlcek et al., 2012), the MW-LA-PECVD system enables growth on 3D objects with good homogeneity over large areas (as evidenced in Figs. 1 and 2) even if the object is held static during the deposition, which other plasma enhanced techniques such as cavity based microwave and hot filament systems would not be able to due to issues such as plasma focusing.

2.2. PCD characterization techniques

Raman spectroscopy measurements were carried out at room temperature using a Renishaw InVia Raman Microscope with

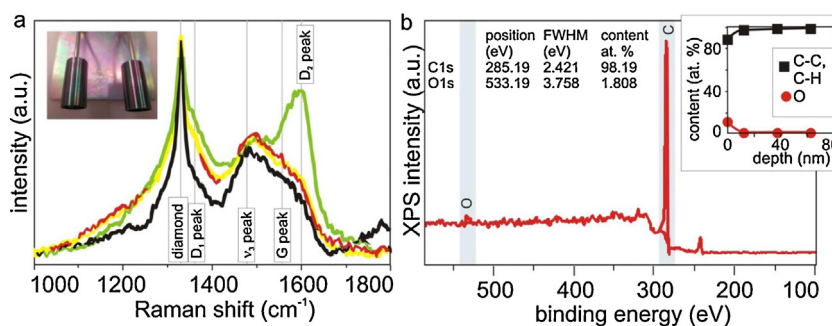


Fig. 2. (a) Raman spectra of the PCD coating prior to corrosion tests. Spectra were collected from various positions over the sample and indicate good homogeneity. The inset shows the deposition of the PCD layer. (b) XPS spectra of the PCD coating prior to corrosion tests acquired at the depth of 65 nm, the inset represents XPS element depth profile.

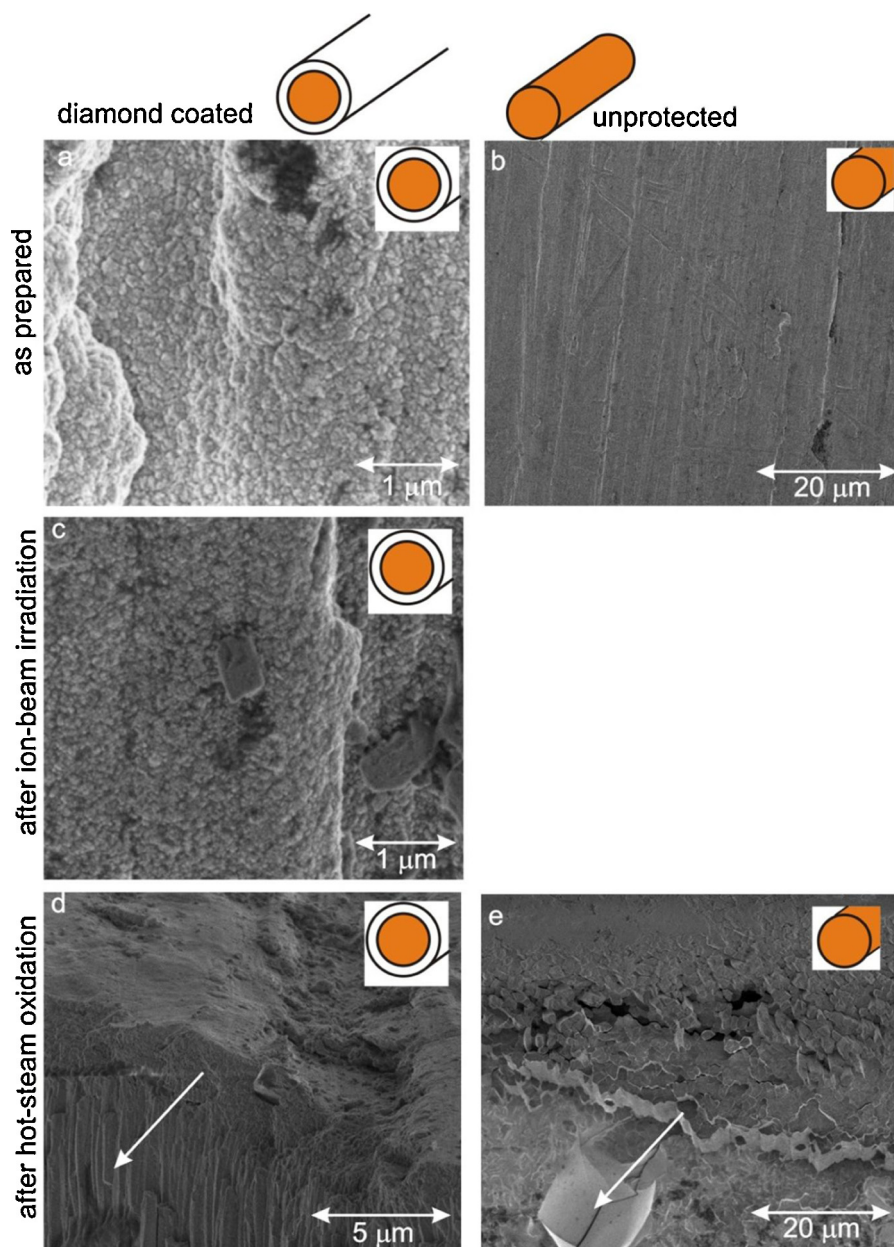


Fig. 3. SEM images of PCD-coated (first column) and uncoated (second column) Zircaloy2 tubes. The samples were measured as-prepared (first row), after ion-beam irradiation (second row) and after hot steam oxidation (third row). The arrows in the SEM images indicate areas where the top-most layer was intentionally scratched off.

the following conditions: laser excitation wavelength of 488 nm (25 mW), 50× Olympus objective, 65 μm slits, spot focus, grating of 2400 l/mm. The surface of the PCD layers was analyzed by a FEI Quanta 3D FEG Scanning Electron Microscope (SEM) fitted with a TSL/EDAX energy dispersive spectrometer (EDS). The accelerating voltage in high resolution mode was kept in the range 2–5 kV, in order to minimize the interaction volume (Figs. 3 and 4). X-ray photoelectron spectroscopy was carried out using an ESCA Probe by Omicron Nanotechnology. The depth concentration profile was obtained using Ar ion sputtering at 5 keV up to a depth of 120 nm. It has been shown by many authors (Lucas et al., 2013; Tan et al., 2011; Olsson and Landolt, 2004) that XPS is a sensitive method for studying the surface of Zr alloys containing carbide and carbon. In our XPS analysis, particular attention was given to obtain a reproducible quantification of the PCD film and the oxide layer development, which was well distinguishable in the survey scan as well as in individual peaks of XPS spectra O 1s and C 1s. The data analysis routine

(sensitivity factor, curve fitting, background subtraction, etc.), used for this purpose permitted quantification of the chemical composition. X-Ray diffraction (XRD) measurements were performed using a PANalytical diffractometer X'Pert PRO equipped with a Co anode ($\lambda = 0.178901$ nm). In order to enhance the contribution of the surface layers a parabolic mirror and a parallel plate collimator were used in the primary and the diffracted beam, respectively. The angle of incidence of the primary beam was 3°. The Rietveld-like program Topas was used for the analysis of the measurement. Since the sample was textured, the Pawley refinement mode was used to improve the preciseness of lattice parameters and crystallite sizes.

2.3. Hot steam oxidation

For hot steam oxidation of the PCD coated Zircaloy2 samples a silica glass tube, 40 mm in diameter was used, which was placed inside a vertically oriented furnace with a maximum operating

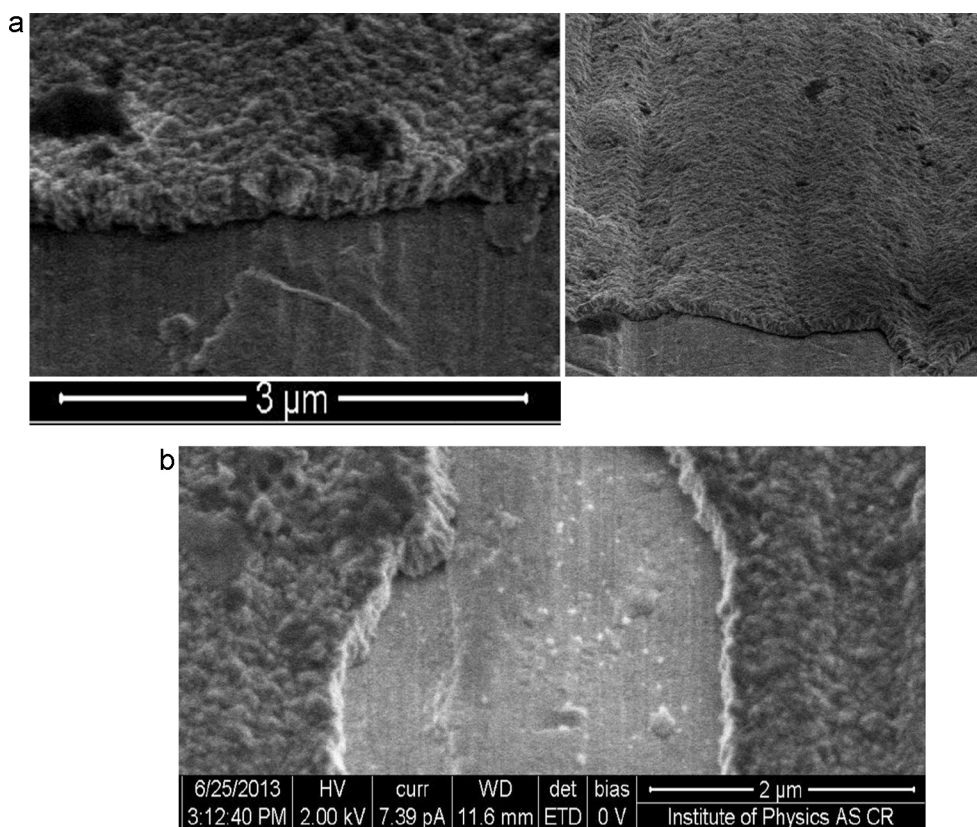


Fig. 4. (a) SEM images of partly removed polycrystalline diamond layer on the Zircaloy2 tube. (b) SEM images of partly removed polycrystalline diamond layer on the Zircaloy2 tube after irradiation tests.

temperature of 1200 °C. To maintain an inert atmosphere during the experiment, argon was flowed through the tube. Samples were hung on a small silica glass tube, supported by a thin glass straw. The small glass tube allows the vertical movement of the tested sample. The lowest position allows the tested sample to be pulled into the testing zone inside the furnace. Further sample movement upwards breaks the holding straw and the sample falls down into a quenching pot. Temperature is measured by a thermocouple located inside the small glass tube. Water was introduced through a thin capillary tube in the furnace below the sample where it evaporated so that steam reacts with the hot sample.

2.4. Ion beam irradiation

In order to replicate constant neutron bombardment, the PCD coated Zircaloy2 sample was subjected to ion beam irradiation testing, by using a 1.7 MeV tandemron accelerator at the ion beam facility of Texas A&M University. Samples were irradiated by Fe ions of 3 MeV at room temperature, to a fluence of $1.95 \times 10^{16} \text{ cm}^{-2}$. The beam spot size was about 5 mm^2 and beam rastering was used to guarantee irradiation uniformity. Irradiation took about 5 h and beam heating was measured to be less than 20 °C. The study's aim was to test radiation tolerance of the deposited PCD layer using ion bombardments to simulate its behavior in neutron environments.

Ion accelerators have been widely used in the past few decades to simulate neutron damage (Gary, 2007). To the first order, correlation between ion irradiation and neutron irradiation can be established through the use of the displacement-per-atom (dpa). However, exact one-to-one correlation is difficult due to many neutron-atypical effects introduced by ion irradiation. One effect is the so-called temperature shifting due to large flux difference between particles from accelerator and neutrons inside a reactor

(Mansur, 1978). Another effect is interstitial injection due to extra atoms introduced by ion irradiation (Garner, 1983). The third effect is lack of concurrent generation of helium and hydrogen. These various artifacts preclude an exact one-to-one ion-neutron comparison for prediction of swelling or other structural degradation. But, ion irradiation can still be used a quick screening tool for materials development, which is the primary motivation in the presented study.

Fig. 5 shows distributions of displacements created by 3 MeV ion irradiation, by using Monte Carlo simulation code SRIM (Ziegler et al., 2009). The peak damage is about 0.9 dpa/Å ion at a depth of 1 μm in the PCD film (assuming a density of 3.5 g/cm^3). The

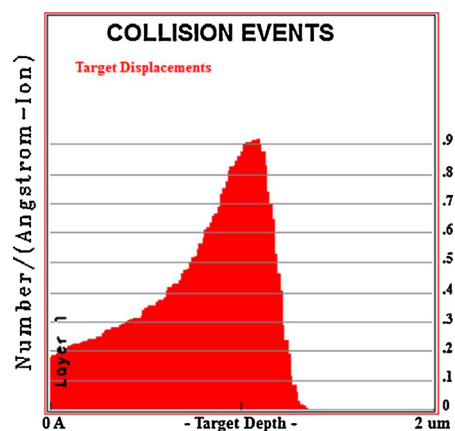


Fig. 5. SRIM calculated distribution of target displacements as a function of depth into the surface of the sample. Doubly charged Fe iron ions were accelerated up to the energy of 3 MeV.

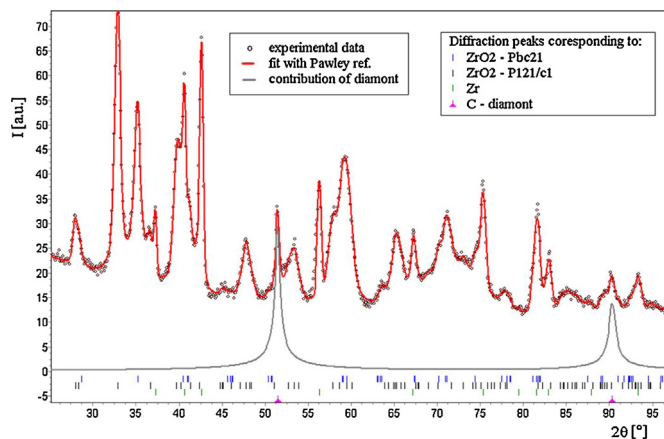


Fig. 6. The X-ray diffraction pattern of the of Zircaloy2 tube coated with the PCD film. The calculated part of diffraction pattern corresponding to diamond is highlighted.

simulation considered normal incidence of the Fe ions into a flat surface. In reality, the cylindrical surface of the sample will lead to variance of incidence angles. We therefore characterized the sample region locally normal to the ion beams. The projected range of Fe ions is about $1.1\ \mu\text{m}$ and the PCD film thickness is about $300\ \text{nm}$. Therefore Fe ion penetration is deep enough to pass through the PCD/Zircaloy2 interface. In other words, interface mixing and debonding are tested in the present study. Systematical studies involving large irradiation matrix at higher energies and higher irradiation temperatures are under progress.

3. Results and discussion

Successful deposition of a PCD layers onto Zircaloy2 tubes is shown by Raman spectroscopy, see Fig. 2a. Raman spectra of the PCD-coated Zircaloy2 sample features the sp^3 diamond line at $1332\ \text{cm}^{-1}$. The diamond line is superimposed on the D_1 disorder-related sp^2 band at $\sim 1350\ \text{cm}^{-1}$. The broad band between ~ 1400 and $\sim 1650\ \text{cm}^{-1}$ can be attributed to non-diamond carbon phases. Namely, it originates in two overlapping components: the ν_3 band around $1480\ \text{cm}^{-1}$ related to amorphous carbon and the G band usually centered around $\sim 1580\ \text{cm}^{-1}$, pertaining to sp^2 carbon phases (Buijnsters et al., 2002) put forward a similar assignment of the peak. Raman spectra collected at various positions over the whole surface of the sample tube, as shown in Fig. 2a, show that the whole surface around the tube was successfully coated and indicate good homogeneity. Spectra taken from positions facing the sample holder during the deposition are somewhat different, containing also the disorder-related D_2 band at $\sim 1600\ \text{cm}^{-1}$, which is attributed to the thermal gradient across the sample during the growth (i.e. the surface facing the sample holder was cooler).

In addition to Raman spectroscopy, growth of PCD is also evidenced by XRD (beam area approx. $3\ \text{mm} \times 10\ \text{mm}$, penetration depth $\sim 2\ \mu\text{m}$) see Fig. 6.

XRD detects the presence of Zr and ZrO_2 (P121/c1 ICSD n. 57187 and Pbc21 ICSD n. 67004 phases approximately in the ratio 1:1) crystallites with mean size around $14\ \text{nm}$ coated with PCD crystallites with average size of $29\ \text{nm}$. X-ray photoelectron spectroscopy depth profiling (using argon ions sputtering) also confirms that the surface layer of PCD coating is made up almost entirely of carbon: 98 atomic % of carbon C–C and C–H bonds are present at $(284.7 \pm 0.5)\ \text{eV}$ with a small amount of incorporated surface oxygen. XPS also evidences that the PCD layer is homogeneous with no obvious impurities. Finally, SEM investigation showed a compact continuous PCD layer around $300\ \text{nm}$ thick without

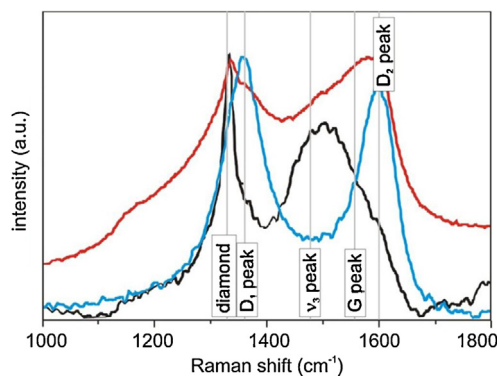


Fig. 7. Comparison of Raman spectra of the PCD coating growth (black curve with sharp diamond peak), after ion beam irradiation (red curve) and hot steam oxidation (blue curve with D_1 peak). Hot steam oxidation causes sp^2 transition of the layer. (For interpretation of the references to color in this figure legend, the reader is referred to the web version of the article.)

obvious indication for pin holes. The corresponding morphologies are shown in Fig. 3.

Morphologically, the PCD coated Zircaloy2 sample subjected to ion irradiation did not reveal any microstructural changes, see Fig. 3e. However, Raman spectroscopy (Fig. 7) revealed an increase in the D_1 and D_2 sp^2 related bands. This effect can be associated with the partial breaking of the sp^3 in the film and formation of sp^2 due to the displacement of carbon atoms. Previous studies on the effect of irradiation on diamond and diamond-like films suggest that the mechanisms of sp^2 transition can be quite complicated as reviewed by Vankar and Dilawar (1996). First, in the case of Fe ion irradiation, nuclear stopping contributes to the generation of atom displacements. Second, electronic stopping leads to electron excitation and ionization, which changes the charge status of the displaced atoms and increases their mobilities. These carbon atoms then prefer to diffuse toward the surface or the interface and promote localized graphitization. Next, damage cascades caused by high energy knock on, which features a vacancy-rich core surrounded by interstitials, facilitate formation of the localized sp^2 phase. Despite the formation of the sp^2 , our study confirms a high level of structural integrity and radiation tolerance after ion irradiation.

In order to simulate the protective capabilities of the PCD layer under emergency conditions in nuclear reactor the PCD coated Zircaloy2 sample underwent a hot steam oxidation (HSO) test. During the HSO test the sample reacted with steam at $1100\ ^\circ\text{C}$ for 30 min. After HSO, the sample was still fully covered by a protective layer. Raman spectroscopy revealed that the PCD layer had graphitized, see Fig. 7: the diamond line is not visible in the spectra, but two sp^2 -related D bands appear, implying that a homogeneous non-crystalline carbon layer (with a large graphitic phase content) covers the Zircaloy2 surface after HSO. Thus, the HSO corrosion test caused the phase transition of the PCD layer to a new material consisting of phase transitioned carbon (soft graphite and amorphous carbon layer), oxygen and substrate Zr atoms. It should be also emphasized that the PCD layer phase transition absorbed a large part of the energy released in the surface oxidation reaction.

Incorporation of the atoms from surrounding and PCD phase transition led to a substantial increase in the thickness of the protective layer, which rose up to $10\ \mu\text{m}$ as measured by cross sectional SEM. XPS analysis showed that Zirconium and oxygen diffused to the film, partly forming zirconium carbide and zirconium oxide.

XRD revealed that after HSO the lattice parameters of the underlying Zr had enlarged by 0.5–0.8% (from $3.228\ \text{\AA}$ to $3.245\ \text{\AA}$ in the a -direction and from $5.153\ \text{\AA}$ to $5.195\ \text{\AA}$ in the c -direction). This suggests that adhesion of the originally PCD film to the Zircaloy2

surface is reasonably good, since tensile strain is preferred over peeling off the layer.

The protective capabilities of the PCD layer were compared with a standard uncoated Zircaloy2 tube after HSO test. The XPS depth profile on the as received Zircaloy2 tube surface showed a thin oxide layer of 100 nm, identified the relative and constant presence of zirconium carbide bonds, binding energy 281.5 eV, probably resulting from acrylate resin. After the HSO test a 10 µm thick layer was formed (SEM, XPS). In contrast to the PCD coated sample, the new layer on the unprotected Zircaloy2 tube is composed mainly of ZrO₂ (XPS), implying a large intake of oxygen (accompanied by the release of hydrogen from the stripped water molecules). The cracked surface with columns is clearly visible in Fig. 3e, differing morphologically from the phase-changed PCD layer, showing also the widening of zirconium oxide layer after HSO test. Starting from 20 nm below the HSO treated PCD coated Zircaloy2 surface we found a higher concentration of zirconium carbide (10 atomic %) and a smaller concentration of oxygen (10 atomic %) as compared to the surface layer of the unprotected Zircaloy2. Furthermore, when we compared O:Zr ratio of PCD protected Zircaloy2 and unprotected Zircaloy2 tube after applied HSO we found significant difference. Normal O:Zr ratio (same as in basic Zircaloy2 material) of protected Zircaloy2 was at 50 nm under the surface whereas in the Zircaloy2 without protection the same O:Zr ratio as in standard Zircaloy2 was found at 100 nm under the surface. Also, a larger post HSO weight gain of the unprotected Zircaloy2 samples (2.04 g dm⁻²) than PCD:ZrA (1.29 g dm⁻²) can be connected with their greater oxygen intake, as oxides massively enters the surface of the unprotected and temperature changed Zircaloy2 material surface and strongly changing its properties. The unprotected Zircaloy2 tube after HSO was also significantly more fragile than the PCD coated sample. All of these results clearly show that PCD protects Zircaloy2 even at high temperature emergency conditions.

The final decision about feasibility of the proposed technique relies not only on the structural, but also on the mechanical and electronic changes. Fine-tuning of the properties of the PCD layer, such as surface roughness or thickness, will be necessary. Obviously, a key issue will be strength of the bonding between the film and the underlying Zircaloy2. Damage cascade induced mixing at the interface can strengthen the bonding, but the accumulation of gas atoms and the difference in thermal expansion coefficients can, on the other hand, weaken it. These complexities will be carefully addressed in the future. PCD's layer temperature dependent phase transition can be also used as marker/sensor of specific conditions in nuclear reactors—high temperature (above 900 °C) cause the phase transition of the PCD layer to a new material consisting of phase transitioned carbon.

4. Conclusions

Cylindrical Zircaloy2 nuclear fuel cladding was covered by a 300 nm thick protective polycrystalline diamond layer using MW-LA-PECVD deposition technique. We showed that the polycrystalline diamond layer protects zirconium alloy nuclear fuel cladding against undesirable oxidation and consolidates its chemical stability while preserving its functionality:

- Using MW-LA-PECVD, which as the ability to coat full 3 m–4 m lengths, nuclear fuel cladding surface was covered by a compact

and homogeneous layer consisting of sp³ and sp² carbon phases with high crystalline diamond content and low roughness (SEM, Raman spectroscopy, XPS and XRD),

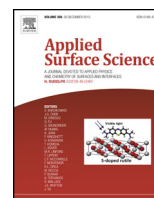
- after ion beam irradiation (10 dpa, 3 MeV Fe²⁺) the PCD film still shows satisfactory structural integrity with both sp³ and sp² carbon phases (SEM, Raman spectroscopy),
- the exposure of the PCD protected Zircaloy2 to hot steam (1100 °C, 30 min) caused the infusion of both oxygen and Zr substrate atoms into the protective layer as well as a phase change of diamond to sp² phase (XPS, Raman spectroscopy, XRD), the Zircaloy2 under the carbon-based protective layer after hot steam oxidation test differed from the original Zircaloy2 material composition only very slightly (XPS) – the PCD coating increases the material resistance to high temperature oxidation, PCD's layer temperature dependent phase transition can be also used as marker/sensor of specific conditions in nuclear reactors.

Acknowledgements

The authors acknowledge financial support from European R&D projects FP7 ITN Grant No. 238201-MATCON, TA01011165, MEYS grant LM2011026, Grant Agency of the Czech Republic (Contract No. 13-31783S), J Drahokoupil is acknowledged for XRD measurement.

References

- Balmer, R.S., et al., 2009. *J. Phys.: Condens. Matter* 21, 364221.
- J.W. Bryan, Wear resistant coating for components of fuel assemblies and control assemblies and method of applying a wear resistant coating, US patent EP 0673539 B1.
- Buijnsters, J.G., Shankar, P., Fleischer, W., van Enckevort, W.J.P., Schermer, J.J., ter Meulen, J.J., 2002. *Diamond Relat. Mater.* 11, 536.
- Burns, P.C., Ewing, R.C., Navrotsky, A., 2012. *Science* 335, 1184–1188.
- Causey, R.A., Cowgill, D.F., Nilson, R.H., 2006. *Review of the Oxidation Rate of Zirconium Alloys*. Sandia National Laboratory Report SAND2005-6006.
- Fendrych, F., Taylor, A., Peksa, L., Kratochvílová, I., Vlček, J., Rezacova, V., Petrak, V., Klüber, Z., Fekete, L., Liehr, M., Nesládek, M., 2010. *J. Phys. D: Appl. Phys.* 43, 374018.
- Garner, F.A., 1983. *J. Nucl. Mater.* 117, 177.
- Gary, S. Was, 2007. *Fundamentals of Radiation Materials Science: Metals and Alloys*. Springer, New York.
- Hirano, M., Yonomoto, T., Ishigaki, M., Watanabe, N., Maruyama, Y., Sibamoto, Y., Watanabe, T., Moriyama, K., 2012. *J. Nucl. Sci. Technol.* 49, 1.
- Högberg, L., 2013. *Ambio* 42, 267.
- Kratochvílová, I., Kovalenko, A., Fendrych, F., Petráková, V., Zálší, S., Nesládek, M., 2011. *J. Mater. Chem.* 21, 18248.
- Liehr, M., Wieder, S., Dieguez-Campo, M., 2006. *Thin Solid Films* 502, 9.
- Lucas, R., Pizon, D., Laborde, E., Trolliard, G., Foucaud, S., Maitre, A., 2013. *Appl. Surf. Sci.* 287, 411.
- Mansur, L.K., 1978. *J. Nucl. Mater.* 78, 156.
- May, P.W., 2000. *Philos. Trans. R. Soc. London Ser. A* 358, 473.
- Olsson, C.O.A., Landolt, D., 2004. *Corros. Sci.* 46, 213.
- Petráková, V., Taylor, A., Kratochvílová, I., Fendrych, F., Vacík, J., Kučka, J., Štursa, J., Cígler, P., Ledvína, M., Fišerová, A., Kneppo, P., Nesládek, M., 2012. *Adv. Funct. Mater.* 22, 812.
- Puls, M.P., 1990. *Metall. Mater. Trans* 21, 2905.
- Steinbrück, M., Věr, N., Große, M., 2011. *Oxid. Metals* 76, 215.
- Taylor, A., Fendrych, F., Fekete, L., Řezáčová, V., Petrák, V., Krucký, J., Nesládek, M., Liehr, M., 2011. *Diamond Relat. Mater.* 20, 613.
- Tan, M., Liu, Q., Zhang, N., Hu, H., Li, B., Kang, X., 2011. *J. Alloys Compd.* 509, 5926.
- Tsugawa, K., Ishihara, M., Kim, J., Hasegawa, M., Koga, Y., 2006. *New Diamond Front. Carbon Technol.* 16, 6.
- Vankar, V.D., Dilawar, N., 1996. *Vacuum* 47, 1275.
- Vlček, J., Fendrych, F., Taylor, A., Novotný, M., Liehr, M., 2012. *J. Mater. Res.* 27, 863.
- Ziegler, J.F., Biersack, J.P., Ziegler, M.D., 2009. *SRIM: The Stopping and Range of Ions in Matter*. Lulu Press, Morrisville, NC.
- Zinkle, S.J., Was, G.S., 2013. *Acta Mater.* 61, 735.



Thin polycrystalline diamond films protecting zirconium alloys surfaces: From technology to layer analysis and application in nuclear facilities

P. Ashcheulov^a, R. Škoda^b, J. Škarohlíd^b, A. Taylor^a, L. Fekete^a, F. Fendrych^a, R. Vega^c, L. Shao^c, L. Kalvoda^d, S. Vratislav^d, V. Cháb^a, K. Horáková^a, K. Kůsová^a, L. Klimša^a, J. Kopeček^a, P. Sajdl^e, J. Macák^e, S. Johnson^f, I. Kratochvílová^{a,d,*}

^a Institute of Physics, Academy of Sciences Czech Republic v.v.i, Na Slovance 2, CZ-182 21, Prague 8, Czech Republic

^b Czech Technical University in Prague, Faculty of Mechanical Engineering, Technická 4, Prague 6, CZ-160 07, Czech Republic

^c Texas A&M University, Department of Nuclear Engineering TAMU-3133, College Station, TX TX 77843, USA

^d Faculty of Nuclear Science and Physical Engineering, Czech Technical University in Prague, Brehova 7, CZ-115 19, Prague 1, Czech Republic

^e University of Chemistry and Technology, Power Engineering Department, Technická 3, Prague 6, CZ-166 28, Czech Republic

^f Nuclear Fuel Division, Westinghouse Electric Company, 5801 Bluff Road, Hopkins, SC 29209, USA

ARTICLE INFO

Article history:

Received 16 July 2015

Received in revised form 2 October 2015

Accepted 16 October 2015

Available online 21 October 2015

Keywords:

Metal coatings

Thin polycrystalline diamond film

Impedance spectroscopy

Raman spectroscopy

XPS

ABSTRACT

Zirconium alloys can be effectively protected against corrosion by polycrystalline diamond (PCD) layers grown in microwave plasma enhanced linear antenna chemical vapor deposition apparatus. Standard and hot steam oxidized PCD layers grown on Zircaloy2 surfaces were examined and the specific impact of polycrystalline Zr substrate surface on PCD layer properties was investigated. It was found that the presence of the PCD coating blocks hydrogen diffusion into the Zircaloy2 surface and protects Zircaloy2 material from degradation. PCD anticorrosion protection of Zircaloy2 can significantly prolong life of Zircaloy2 material in nuclear reactors even at temperatures above Zr phase transition temperatures.

© 2015 Elsevier B.V. All rights reserved.

1. Introduction

Our research is motivated by the essential investigation of new strategies on how to protect zirconium alloys nuclear fuel cladding surface, in particular by polycrystalline diamond (PCD) film. Zirconium has very useful properties for nuclear facilities applications due to its low absorption cross-section of thermal neutrons [1–7]. However, there is also a significant disadvantage: zirconium surface reacts with water steam and during this (oxidative) reaction it releases hydrogen gas, which partly diffuses into the alloy forming zirconium hydrides. At temperatures around 850 °C the α phase of zirconium changes to β phase which is more opened for oxygen/hydrogen diffusion. The zirconium alloys changed by oxygen/hydrogen diffusion are less dense and are mechanically weaker than the original material - their formation results in blistering and

finally cracking of the cladding [5,6]. Moreover, big production of hydrogen gas during oxidative reaction can result into hydrogen-air chemical explosions (like in the recent Fukushima accident). As these effects are surface related [8–20], a solution to the problem, namely how to fully utilize the advantages of the bulk of the zirconium-based material and to reinforce its surface chemical resistance, is to cover the material surface with a thin film of a protective substance. Recently, many materials have been applied to protect zirconium alloys surfaces from destruction, but without any significant success [5–7].

In our previous work [20] we utilized our experience of growing polycrystalline diamond layers using microwave plasma enhanced linear antenna chemical vapor deposition apparatus (MW-LA-PECVD) [22–24] and protected Zircaloy2 surfaces with PCD films.

Diamond has excellent material properties as a protective layer in nuclear applications: high thermal stability, thermal conductivity, neutron cross-section and chemical stability – therefore, it has already been used for a large variety of applications [14–18,23–25].

In Ref. [20], first studies on a new PCD application were made: we showed that PCD films kept structural integrity with both sp^3

* Corresponding author at: Institute of Physics, Academy of Sciences Czech Republic v.v.i, Na Slovance 2, CZ-182 21 Prague 8, Czech Republic.
Tel.: +420 723814810.

E-mail address: krat@fzu.cz (I. Kratochvílová).

and sp^2 C phases after ion beam irradiation (10 dpa, 3 MeV Fe^{2+}). The Zircaloy2 under the PCD protective layer after 1100 °C differed from the original Zircaloy2 material composition very slightly. On the contrary, for unprotected 1100 °C hot steam oxidized Zircaloy2 oxide massively enter the surface and strongly change its composition and properties. Unprotected Zircaloy2 after 1100 °C hot steam oxidation was also significantly more fragile than the 1100 °C treated PCD coated sample.

In this work we focused on progress in description and understanding of polycrystalline diamond/Zircaloy2 fuel cladding surface properties after 950 °C hot steam tests and the specific impact of the metal surface on parameters of PCD layers. We investigated if and how PCD layer protects Zircaloy2 surface against corrosion at a temperature when α phase of zirconium changes to β phase (when Zircaloy2 is more opened for oxygen/hydrogen diffusion) [20]. To expand the PCD layer possible applications (PCD growth on intentionally unseeded surfaces) we also showed how zirconium surface crystallinity affects the PCD layer grown in MW-LA-PECVD reactor [35]. A number of characterization methods: Scanning Electron Microscopy (SEM), Atomic Force Microscopy (AFM), Raman spectroscopy, X-ray photoelectron spectroscopy (XPS) and neutron scattering, secondary ion mass spectroscopy (SIMS) [26–34] and impedance spectroscopy [35–37] were employed both before and after corrosion 950 °C hot steam oxidation.

2. Experimental

2.1. Growth of PCD

A microwave plasma enhanced linear antenna chemical vapor deposition apparatus (MW-LA-PECVD) as described in [22,23] was used for the deposition of PCD films. The Zircaloy2 rod fuel claddings and polycrystalline Zr samples plates were immersed in a colloidal solution of diamond nanoparticles (NanoAmando®), which act as seeds and therefore induce nucleation sites for PCD growth. As a comparison unseeded polycrystalline Zr plate samples were loaded into the reactor. The Zircaloy2 rods were suspended in the reactor to ensure that their whole surface is exposed to plasma.

For PCD layer growth in MW-LA-PECVD a gas mixture of $H_2 + CH_4 + CO_2$ at low process pressures (<1 mbar) with a MW power of 2×3 kW was used. Owing to its diffuse plasma properties due to low process pressures, the MW-LA-PECVD system enables growth on 3D objects with good homogeneity over large areas (Fig. 1).

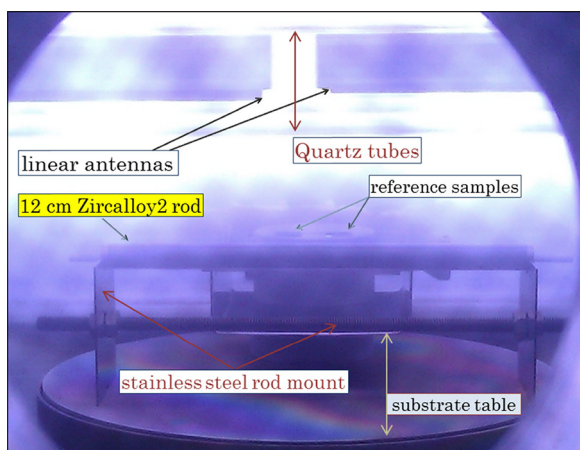


Fig. 1. Photograph of Zircaloy2 rod during PCD deposition. Above the Zircaloy2 rod the linear antennas (from which diffuse plasma is formed) can be seen housed inside quartz tubes which act as air/vacuum interfaces. Reference samples are app. 2 cm long.

2.2. PCD characterization techniques

Surfaces morphology of PCD layers were analyzed by a Tescan FERA 3 Scanning Electron Microscope and atomic force microscopy. Accelerating voltage in the high resolution mode was kept in the range 2–5 kV, in order to minimize the interaction volume. Atomic Force Microscopy measurements were performed on PCD layers grown on planar polycrystalline Zr using Dimension Icon Bruker microscope using Tap150Al-g budget sensors tips (resonant frequency 150 kHz, force constant 5 N/m) in ScanAsyst measurement mode and under ambient conditions.

Deposited layers were also characterized by Raman spectroscopy carried out at room temperature using a Renishaw InVia Raman Microscope under following conditions: laser excitation wavelength of 488 nm (25 mW), $\times 50$ Olympus objective, 65 μm slits, spot focus, and grating of 2400 lines/mm to determine the PCD layer composition.

Monochromatic beam of thermal neutrons (wavelength 0.1362 nm, parallel collimation, 40 mm \times 40 mm cross-section) was utilized on PCD coated Zircaloy2 samples before and after hot steam oxidation (950 °C). Two types of measurements were performed: (i) characterization of the crystallographic texture by means of inverse pole densities p_{hkl} calculated in Harris approximation [30] and (ii) determination of linear attenuation coefficient characterizing the reduction of the incident neutron beam intensity across the specimen ($\Sigma = t^{-1} \ln(I_0/I)$ where t is the path through the specimen, I_0 and I is the incident and transmitted intensity, respectively) [29]. Due to its high penetration power and large beams cross-section available, family of neutron scattering techniques provides a very mighty tool for analysis of microstructure, crystalline structure and crystallographic preferential orientation (texture) of voluminous polycrystalline samples. In case of zirconium alloys, application of the methods is exceptionally fruitful because of the high scattering cross-sections of thermal neutrons on light elements allowing thus for analysis of concentration and crystallographic orientation of zirconium hydrides playing a crucial role in degradation of mechanical properties of the material exposed to high temperature/pressure water environment [26]. The neutron diffraction and transmittance experiments were performed on four types of tube samples of different technological and testing history. For the neutron measurements, the tubes were cut into segments and glued on a plastic foil to form planar specimens. Orientation of the specimens was related to the three orthogonal directions of the original tube: the longitudinal (axial) direction, the circumferential direction and the radial direction.

The X-ray photoelectron spectroscopy was carried out at the NanoESCA instrument (Oxford Instruments Omicron Nanoscience) on planar polycrystalline Zr samples. The monochromatic Al $K\alpha$ (1486.6 eV) X-ray was used as source. It can be focused to illuminate a spot of size 10–100 μm . Emitted electrons are accelerated by the voltage 15 kV and then they enter the Photo Emission Electron Microscopy. The XPS spectra were recorded with pass energy of 100 eV X-ray.

Zircaloy2 samples were analyzed by secondary ion mass spectroscopy (SIMS) using an ATOMIKA setup with an oxygen sputter gun operating at 10 keV. The angle of ion beam incidence was 45°. The sputtered ions were analyzed by a quadrupole mass filter.

2.3. Hot steam oxidation

Hot steam oxidation of the PCD coated and bare Zircaloy2 samples were carried out in a silica glass tube, 40 mm in diameter, placed inside a furnace with maximal operating temperature 1200 °C. A small silica glass capillary allows the movement of tested sample inside the silica glass tube. Silica glass capillary is also equipped with N type thermocouple, which serves for temperature

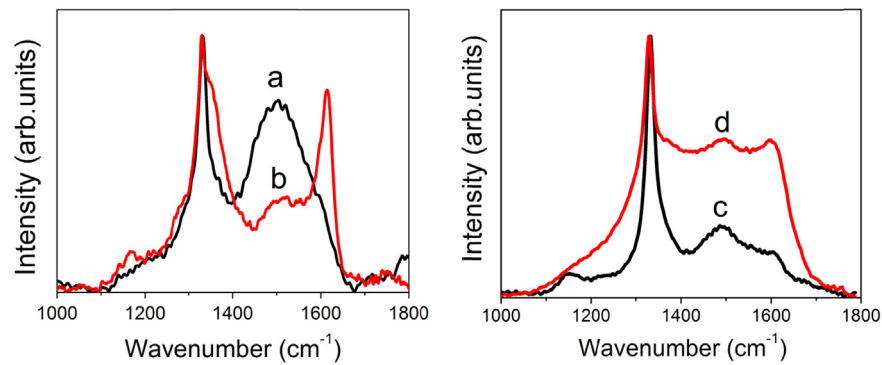


Fig. 2. Left: Raman spectra of the PCD coated Zircaloy2 sample (a), PCD coated Zircaloy2 sample after hot steam oxidation at 950 °C (b). Right: Raman spectra of seeded planar Zr polycrystalline samples with grown PCD (c), unseeded planar Zr polycrystalline samples with grown PCD layer (d).

measurement inside the furnace. Water was introduced through a thin capillary tube in the furnace below the sample where it evaporates – steam reacts with the hot sample. PCD coated Zircaloy2 samples were exposed to steam for 30 min at temperature 950 °C and after that slowly cooled in the inert argon atmosphere.

2.4. Impedance spectroscopy

Impedance spectra [38] were measured at room temperature in a demineralized water solution of K_2SO_4 (0.5 M) in a 3-electrode cell. A saturated calomel electrode was used as a reference electrode, Zircaloy2 tube samples approximately 5 cm long were used as working electrodes. The edges and internal surface of the tubes were isolated. Platinum wire coaxially wound around the working electrode served as counter electrode. The measurement set-up included Reference600 potentiostat (Gamry). Impedance spectra were measured after the stabilization of open circuit potential in the range of 1×10^6 to 1×10^{-4} Hz in the potentiostatic mode. The amplitude of perturbation signal was 5 mV. Impedance spectra were analyzed using ZSimpWin 3.21 software.

3. Results and discussion

3.1. Hot steam oxidation tests: weight change

Hot steam oxidation (HSO) at 950 °C was applied to PCD coated and bare Zircaloy2 samples. After HSO at 950 °C, the Zircaloy2 sample was still covered by a protective PCD layer. Weight gains were measured after HSO tests of PCD coated Zircaloy2 samples and unprotected Zircaloy2 samples. A greater relative weight gain after hot steam oxidation of unprotected Zircaloy2 sample (0.38 g dm^{-2}) than PCD coated Zircaloy2 (0.20 g dm^{-2}) can be explained by the

stronger oxidation impact on the unprotected surface. Oxygen massively enters the surface which, being unprotected and with temperature variations, strongly changes its properties.

3.2. Raman spectroscopy

Fig. 2 shows the typical Raman spectra of PCD films grown on Zircaloy2 and polycrystalline Zr substrates. The peak at 1332 cm^{-1} corresponds to the stretching vibration of the tetrahedrally (sp^3) bonded carbon in the diamond lattice. The band centred at 1500 cm^{-1} is related to transpolyacetylene, which is typical for the nanocrystalline form of the PCD layer [28].

After hot steam oxidation of the PCD coated Zircaloy2 sample at 950 °C (Fig. 2b) peaks related to disorder carbon (D) and amorphous carbon (G) at 1350 cm^{-1} and 1600 cm^{-1} , respectively, appear, which is a sign of partial sp^3 to sp^2 transition in the PCD layer during steam oxidation treatment.

For the seeded and unseeded polycrystalline Zr samples sp^3 peaks are also seen along with the G peak of amorphous carbon (Fig. 2 right). Notably, the Raman spectrum of unseeded planar polycrystalline Zr sample (Fig. 2d) shows a relatively larger amount of sp^2 C phase (higher intensity of D and G phases) than for the PCD layer grown on seeded polycrystalline Zr sample (Fig. 2c). This is attributed to the fact that isolated diamond grains grown on the unseeded polycrystalline Zr substrate comprise of sp^3 bonded carbon “diamond” core enveloped by the sp^2 bonded carbon layer located on the outermost surface. Furthermore, transpolyacetylene peak situated at 1120 cm^{-1} in the spectrum for seeded polycrystalline Zr is not observed for the unseeded polycrystalline Zr sample, leading to a conclusion that outermost surface of isolated diamond grains grown on unseeded sample are comprised only of sp^2 carbon.

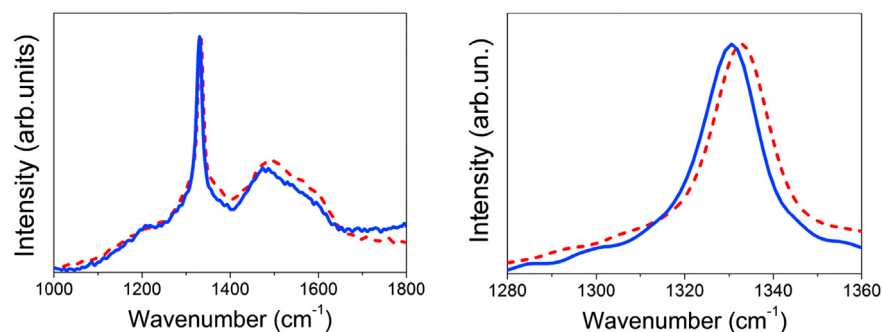


Fig. 3. PCD Raman line dispersion. Left: diamond peak 1332 cm^{-1} for PCD layer grown on seeded Zircaloy2 surface (dotted line) and 1329 cm^{-1} for PCD layer grown on unseeded Zircaloy2 surface (full line). Right: detail of the spectra. In unseeded samples we can suppose bigger number of nanometer scale crystallites than in seeded sample. From diamond Raman line dispersion spectra we can suppose relevant number of nanometer scale crystallites in the layer grown on unseeded Zircaloy2 surfaces.

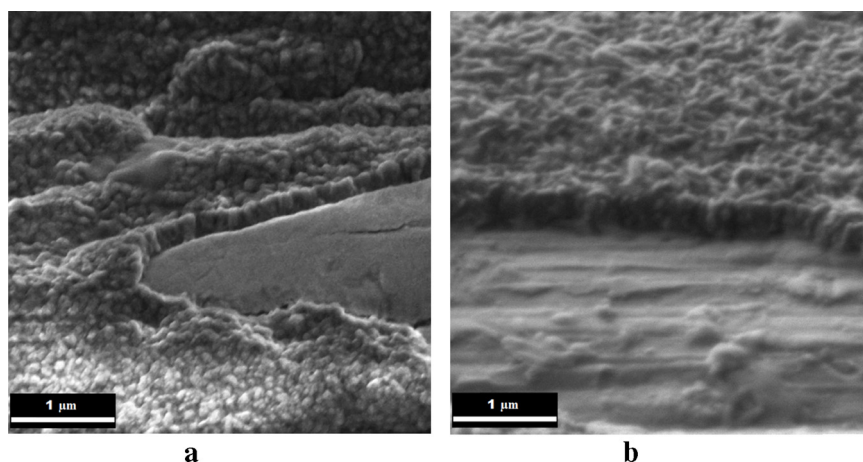


Fig. 4. SEM images of PCD-coated Zircaloy2 fuel cladding sample standard (a) and after HSO at 950 °C (b). In both cases part of the PCD layer was artificially peeled off before SEM measurements.

Additionally, for Zircaloy2 samples Raman diamond peak was situated at 1332 cm^{-1} for PCD layer on seeded surface and at 1329 cm^{-1} for PCD layer on unseeded surface. Layers on unseeded Zircaloy2 surfaces have a bigger number of smaller physical dimensions (up to tenths of nm) of diamond crystals than layers grown on seeded Zircaloy2 substrates (Fig. 3). This 3 cm^{-1} downshift of the first order diamond Raman line (1332 cm^{-1}) of layers grown on unseeded Zircaloy2 samples is through a relaxation of the $q=0$ selection rule [39] for nanometer scale diamond crystals. From diamond Raman line dispersion spectra [40] we can suppose relevant number of nanometer scale crystallites in the layer grown on unseeded Zircaloy2 surfaces. The AFM analysis of the unseeded Zircaloy2 sample (see Fig. 5b) reveals the formation of isolated diamond crystals in a form of non-closed layer, thus the diamond peak downshift can be associated solely with the diamond crystals size. Finally, diamond peak positions and full width at half maximum (FWHM) values for seeded/unseeded Zircaloy2 and polycrystalline Zr samples are summarized in the Table S1.

3.3. Scanning electron microscopy/atomic force microscopy

Scanning Electron Microscopy (SEM) was employed to evaluate surface coverage, crystal size, crystal shape and thickness of PCD covering Zircaloy2 before and after hot steam oxidation tests. As deposited PCD coating grown on seeded areas of Zircaloy2 samples are compact and without pinholes. The delamination was done manually to measure the PCD layer thickness as shown in Fig. 4. No significant variation of PCD films thickness (300 nm) before and after HSO test at 950 °C was observed. Overall, the studies suggest a high level of structural integrity of diamond coated Zircaloy2 after HSO.

SEM images of both planar polycrystalline Zr samples revealed distinct differences between seeded and unseeded samples (Fig. 5a and b). A closed PCD layer with octahedral grains, i.e. with eight triangular (111) faces, with random orientations was observed on seeded polycrystalline Zr sample (Fig. 5a). SEM images from the unseeded polycrystalline Zr sample (Fig. 5b) shows growth of isolated grains with an average grain size of 500 nm, with a nucleation density of about 10^8 cm^{-2} , which is 3 decades above diamond nucleation density reported on untreated substrates [34]. There were not observed neck or conical shapes of the growing grains between the substrate and PCD layer, which is the sign of good coalescence of PCD layer on substrate. That is why the PCD layer is rigid. Even separate PCD grains on unseeded sample are in good contact with the substrate, the mechanism of the coalescence is the same as in the case of the compact layer.

AFM analysis confirmed that a continuous layer was formed on the seeded polycrystalline Zr surfaces and isolated diamond crystals were grown on the surface of unseeded polycrystalline Zr (Fig. 5c and d).

Using AFM it was also possible to establish the RMS roughness of the coated Zircaloy2 samples to 20 nm on the scale of $3\text{ }\mu\text{m} \times 3\text{ }\mu\text{m}$, where the measured area is slightly influenced by the natural roughness of the Zircaloy2 substrate. The RMS roughness on a reference sample (PCD layer on a seeded flat Silicon (Si) substrate grown at the same conditions) was of 16.1 nm. The PCD layer thickness of the reference Si sample was of 300 nm, which is in a good agreement with the value obtained by SEM. The algorithm based on the autocorrelation function [41] was used to evaluate the grain size distribution from AFM topographies. The mean lateral-size of diamond crystals in case of reference sample and PCD layer grown on seeded Zircaloy2 was of 90 nm with a few larger crystals.

3.4. X-ray photoelectron spectroscopy

We compared photoemission spectra of seeded and unseeded planar polycrystalline PCD covered Zr samples. From the oxygen/carbon peaks ratio in XPS spectra we can conclude that on the surface of unseeded polycrystalline Zr sample a larger fraction of oxygen atoms was absorbed compare to that of PCD layer grown on seeded sample (Figs. 6 and 7). C1s main peak (D) was broader on unseeded polycrystalline Zr covered by PCD – Fig. 7 and its position was shifted to higher binding energies – 0.6 eV (compared to seeded polycrystalline Zr). This is caused by different chemical states (i.e. more sp^2 hybridization) of carbon. In C1s photoemission spectra, specific peaks corresponding to different chemical states of carbon were determined on unseeded samples. Positions and interpretation of individual peaks are reported in Table 1. Peak D and D' are assigned to sp^3 hybridized carbon. The different binding energies of peaks can correspond to different modifications of bonds with respect to ambient. Peak E is attributed to sp^2 hybridized carbon. The other peaks are attributed to organic compounds [30]. The main peaks seen in the seeded PCD covered polycrystalline Zr sample XPS spectrum are assigned to sp^3 carbon. PCD grown on unseeded polycrystalline Zr contains mixture of sp^3 hybridized C, sp^2 hybridized carbon and oxidized carbons. Small amount of organic compounds in unseeded polycrystalline Zr sample are represented by peaks A, B, C in C1s spectrum (Fig. 7). Organic compounds are presented on these parts of unseeded samples surfaces where diamond crystals were not present. Zr 3d was also measured at the PCD surface.

Additionally, SIMS measurements have confirmed no relevant contamination of B and Si atoms (which might incorporate to the

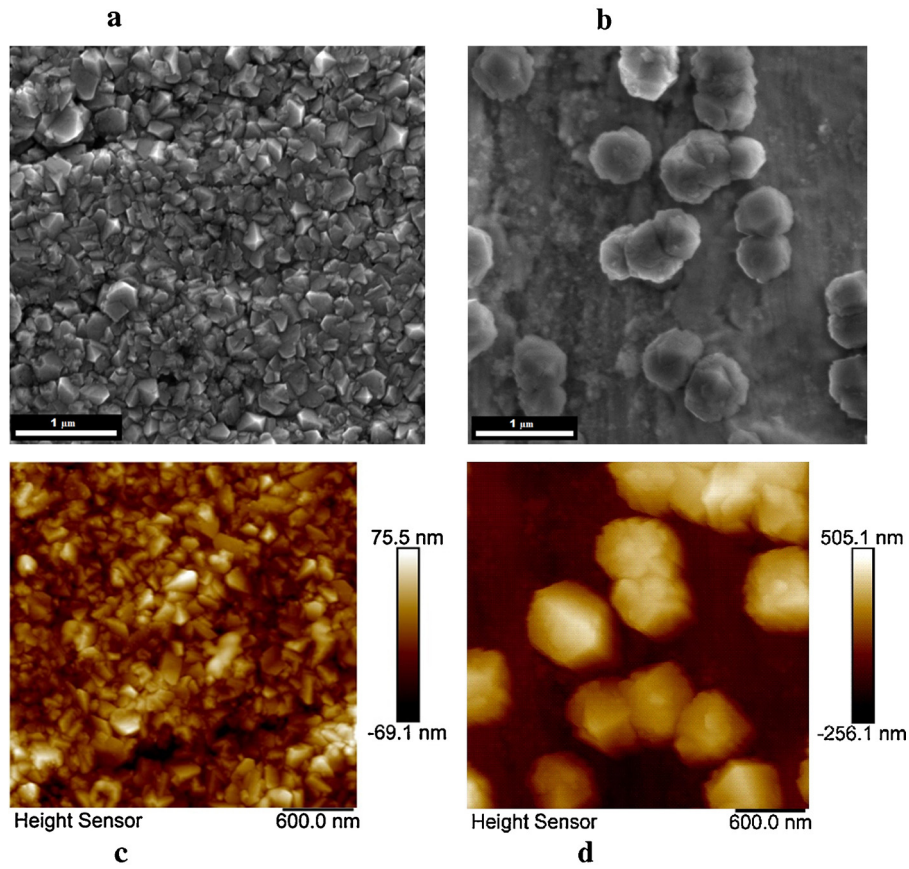


Fig. 5. SEM images of the (a) seeded and (b) unseeded planar polycrystalline Zr samples with PCD layers. AFM images of (c) seeded and (d) unseeded planar polycrystalline Zr samples showing the grain sizes.

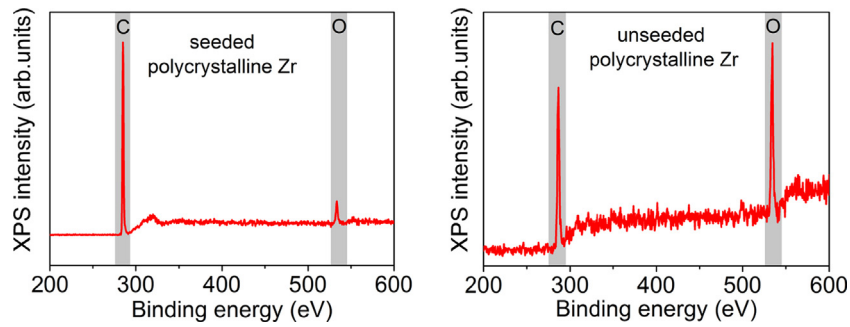


Fig. 6. Photoemission spectra of seeded (left) and unseeded (right) planar polycrystalline Zr samples with NCD layers.

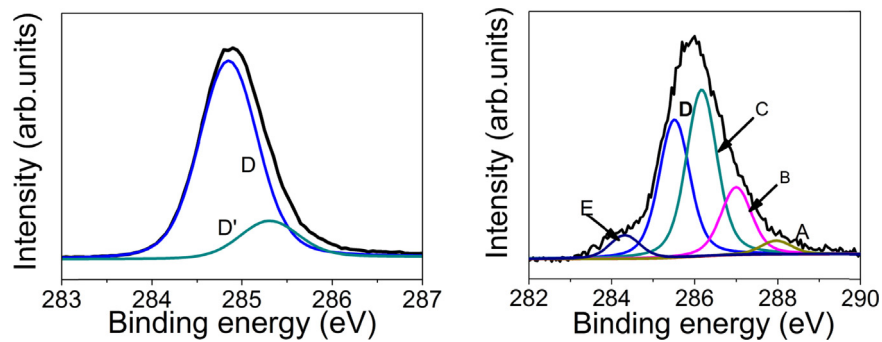


Fig. 7. Comparison of fitted C1s photoemission spectra seeded (left) and unseeded (right) polycrystalline Zr PCD coated samples.

Table 1

XPS peaks corresponding to different chemical states of carbon determined from photoemission spectra of PCD layer grown on unseeded and seeded polycrystalline Zr.

Bond	Seeded polycrystalline Zr Binding energy (eV)	Unseeded polycrystalline Zr Binding energy (eV)
sp ²	–	284.3 (E)
sp ³	284.9 (D), 285.3 (D')	285.5 (D)
≥C–O–C≤>C–OH	–	286.2 (C)
>C=O	–	287 (B)
–C=O OH	–	288 (A)

PCD layer during the deposition process) in PCD layers grown on Zircaloy2 samples discussed herein.

3.5. Neutron diffraction and transmittance

The obtained results of neutron diffraction and transmittance can be summarized as follows:

The presence of PCD coatings on Zircaloy2 fuel cladding samples does not influence the character of the texture changes caused by the thermal treatment. For both sets of samples, steam treatment leads to a slight decay of the inverse pole densities in axial direction orientations of grains obtained along the <001> crystallographic directions and a slight rise of the inverse pole densities in radial direction orientations of grains obtained along the <001> crystallographic directions (Tables S2, S3). There is no significant difference between the texture changes observed for the coated and uncoated samples.

The preferential orientation of the basal planes poles found along the radial direction is compatible with the circumferential orientation of zirconium hydrides platelets. Reduction of the radial orientation of the latter is highly desired in order to preserve good mechanical properties of zirconium alloy tubes [26].

Observed values of linear absorption coefficient are summarized in Table 2. For both types of tested samples, the steam treatment leads to a small increase of sample absorption – the material absorption increase is caused by hydrogen entering Zr surface during HSO process. The effect is more pronounced in case of the uncoated samples, thus suggesting that presence of the coating (to some extent) blocks the hydrogen diffusion into the metal.

3.6. Electrochemical impedance spectroscopy

Impedance spectra of Zircaloy2 samples are given in Fig. 8. Experimental data fitting was performed using equivalent circuit

Table 2

Results of the neutron transmission experiments. I_0 and I is the incident and transmitted beam intensity, respectively; t is the tested specimen thickness and Σ is the observed linear absorption coefficient.

Sample	I/I_0	t (cm)	Σ (cm ⁻¹)
Zircaloy2 fuel cladding	0.969	0.2	0.0157
Zircaloy2 fuel cladding coated by PCD	0.965	0.2	0.0178
Zircaloy2 fuel cladding after HSO at 950 °C	0.967	0.2	0.0167
Zircaloy2 fuel cladding coated by PCD after HSO at 950 °C	0.964	0.2	0.0183

models which included 1 (for Zircaloy2 without PCD) to 3 (for Zircaloy2 PCD coated and Zircaloy2 hot steam oxidized at 950 °C) ZARC elements in series. ZARC impedance can be expressed as:

$$Z = \frac{R}{1 + (j\tau\omega)^n}$$

where R is resistance, τ is relaxation time constant $\tau = RC$, where C is capacitance parallel to R , j is imaginary unit and ω is angular frequency. In this equation n is a dimensionless coefficient which quantifies degree of impedance dispersion. In case of $n = 1$ no time constant dispersion occurs.

The high frequency end of the spectra of samples not exposed to HSO (Fig. 8a) is distorted by measurement artifacts of inductive nature (originated from connecting leads and mutual inductance of working and counter electrode circuit). Impedance of the PCD coated Zircaloy2 sample is increasingly dispersive, due to its polycrystalline character, surface roughness and distributed charge transfer properties of the PCD layer. Values around 0.85 are typical for PCD coated samples compared to values $0.95 < n < 1$ found for the bare Zircaloy2 surface. The impedance response of the PCD layer is distinguishable at high frequencies between 10^4 and $\sim 5 \times 10^5$ Hz. The capacitance values estimated by complex capacitance analysis [37,38] of the high frequency impedance of PCD layer were between 2×10^{-8} and 2.6×10^{-8} F cm⁻², which corresponds, for the 300 nm thick layer, to the effective relative permittivity $\epsilon_r = 6.7$ –9. Such values indicate permittivity of a mixture of diamond (5–6) and graphite (10–15). Resistance associated with PCD layer was about 90–100 Ω cm².

Impedance spectra of samples exposed to HSO at 950 °C (Fig. 8b) show, at high frequencies a dominating capacitance contribution from the zirconium oxide (ZrO₂) corrosion layer. This part of the spectra is typical for a very low impedance dispersion (phase angle Φ is close to -90° and the slope of $\log|Z|$ vs. $\log f$ is approximately equal to 1) and extends down to 10^4 Hz (in the case of oxide grown on a bare Zircaloy2 sample) or to 10^2 Hz for the zirconium oxide formed on PCD coated sample. Capacitance of the zirconium oxide corrosion layer formed on the untreated Zircaloy2 surface was

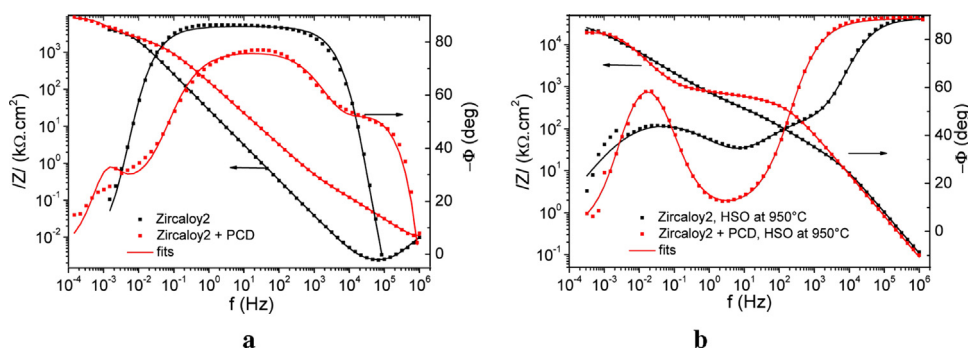


Fig. 8. Bode plots of impedance spectra of PCD coated and uncoated Zircaloy2 samples before (a) and after (b) exposure in steam at 950 °C. Measured in 0.5 M K₂SO₄ at a laboratory temperature.

between 1.4×10^{-9} and 1.8×10^{-9} F cm⁻². Using ϵ_r (ZrO₂) = 23, oxide thickness results between 11 and 14 μ m. Capacitance of zirconium oxide formed on PCD coated sample was around 2.3×10^{-9} F cm⁻². Assuming the same relative permittivity, the thickness of the oxide is \sim 8–10 μ m. Both samples were exposed to the high temperature steam for the same time. Consequently, this is an indication of the relatively lower corrosion rate of PCD coated samples during HSO. Moreover, significant differences between the two cases can be seen in the lower frequency range of impedance spectra. The spectra of uncoated bare samples after HSO test are distinguished by a higher degree of impedance dispersion and by the presence of three time constants. It suggests a more heterogeneous oxide structure including probably up to three sublayers of different charge transfer properties and different levels of impedance dissipation and/or porosity effects. Total oxide resistance was of 2×10^5 Ω cm². The spectrum of PCD coated sample exposed in steam shows 2 well separated time constants. The oxide layer resistance was approximately 1×10^6 Ω cm². No signs of PCD layer impedance response after HSO test were noted in the spectra. A probable reason is the dominating effect of oxide impedance in the high frequency part of the spectrum.

The low frequency limit of impedance can be interpreted as polarization resistance. It is in both cases approximately 2×10^7 Ω cm².

It can be concluded that a thicker oxide layer distinguished by a higher degree of impedance dispersion and/or porosity and lower resistivity was formed on the untreated sample.

4. Conclusions

In this work we showed that PCD films prepared by MW-LA-PECVD technology can be used as anticorrosion protective layer for Zircaloy2 nuclear fuel claddings at elevated temperatures (950 °C) when α phase of zirconium changes to β phase (more opened for oxygen/hydrogen diffusion). Quality of PCD films was examined by Raman spectroscopy, XPS, SEM, AFM and SIMS analysis.

The polycrystalline diamond films were of high quality - without defects and contaminations. After hot steam oxidation (950 °C) a high level of structural integrity of PCD layer was observed. Both sp² and sp³ C phases were present in the protective PCD layer. A greater relative weight gain of oxidized unprotected Zircaloy2 compared to that of the oxidized PCD coated Zircaloy2 samples is due to oxidation of the unprotected surface, as also confirmed by the formation of a thicker oxide layer after hot steam exposure verified by impedance spectroscopy measurements. Also, a higher resistance and a lower degree of impedance dispersion was found in the hot steam oxidized PCD coated Zircaloy2 samples, which may suggest better protection of the Zircaloy2 surface. The PCD layer blocks the hydrogen diffusion into the Zircaloy2 surface thus protecting the material from degradation.

Nucleation of diamond on polycrystalline Zr surfaces without seeding pretreatment was observed. This finding will be additionally studied in the near future in order to establish ways of coating Zircaloy2 tubes with a homogeneous and pinhole free polycrystalline diamond layer without nanodiamond seeding.

Hot steam oxidation tests confirmed that PCD coated Zircaloy2 surfaces were effectively protected against corrosion. Presented results demonstrate that the PCD anticorrosion protection can significantly prolong service life of Zircaloy2 nuclear fuel claddings in nuclear reactors even at elevated temperatures.

Acknowledgements

Special thanks to Patrik Foral from Westinghouse Electric Czech Republic s.r.o. for cooperation. The authors acknowledge

financial support from TACR grants TA01011165, TA04020156, MEYSCR grants LM2011026 and RVO14000, Czech Science Foundation grants 13-31783S, 14-10279S and 15-05095S. Department of Analysis of Functional Materials would like to thank projects SAFMAT CZ.2.16/3.1.00/22132, MEYS LO1419 and further project Large infrastructure LM2011029. Development of the methodology used in the neutron diffraction and transition experiments was supported by the grant 14-36566G of the Czech Science Foundation.

Appendix A. Supplementary data

Supplementary data associated with this article can be found, in the online version, at <http://dx.doi.org/10.1016/j.apsusc.2015.10.117>.

References

- [1] M. Hirano, T. Yonemoto, M. Ishigaki, Watanabe V.F.N., Y. Maruyama, Y. Sibamoto, N. Watanabe, K. Moriyama, J. Nucl. Sci. Technol. 49 (2012) 1–17.
- [2] G.S. Was, Fundamentals of Radiation Materials Science: Metals and Alloys, Springer Berlin Heidelberg New York, New York, 2007, 978-3-540-49471-3.
- [3] L. Höglberg, Ambio 42 (2013) 267–284.
- [4] M.P. Puls, J. Nucl. Mater. 393 (2009) 350–367.
- [5] R.A. Causey, D.F. Cowgill, R.H. Nilson, Sandia National Laboratory Report 2006 SAND2005-6006.
- [6] K.M. Song, S.B. Lee, J. Power Ener. Syst. 2 (2008) 47–56.
- [7] M. Steinbruk, N. Věr, M. Große, Oxid. Metals 76 (2011) 215–232.
- [8] P.C. Burns, R.C. Ewing, A. Navrotsky, Nuclear fuel in a reactor accident, Science 335 (2012) 1184–1188.
- [9] J. Vujic, R.M. Bergmann, R. Skoda, M. Miletic, Energy 45 (2012) 288–295.
- [10] S.J. Zinkle, G.S. Was, Acta Mater. 61 (2013) 735–758.
- [11] G.S. Brady, H.R. Clauser, J.A. Vaccari, Materials handbook: an encyclopedia for managers, technical professionals, purchasing and production managers, technicians, and supervisors, McGraw-Hill Professional, United States 2002, p. 1063. ISBN 978-0-07-136076-0.
- [12] V. Dostal, M. Takahashi, Prog. Nucl. Energy. 50 (2008) 631–637.
- [13] J.W. Bryan, Wear resistant coating for components of fuel assemblies and control assemblies and method of applying a wear resistant coating, US patent EP0673539 B1.
- [14] P.W. May, Diamond thin films: a 21st-century material, Philos. Trans. R. Soc. Lond. A: Math. Phys. Eng. Sci. 358 (2000) 473–495.
- [15] W.D. Man, J.H. Wang, C.X. Wang, Z.B. Ma, New Carbon Mater. 17 (2002) 62–70.
- [16] E. Monroy, F. Omnès, F. Calle, Semicond. Sci. Technol. 18 (2003) R33–R51.
- [17] Y. Gurbuz, O. Esame, I. Tekin, W.P. Kang, J.L. Davidson, Solid State Electron. 49 (2005) 1055–1070.
- [18] R.S. Balmer, J.R. Brandon, S.L. Clewes, H.K. Dhillon, J.M. Dodson, I. Friel, P.N. Inglis, T.D. Madgwick, M.L. Markham, T.P. Mollart, N. Perkins, G.A. Scarsbrook, D.J. Twitchen, A.J. Whitehead, J.J. Wilman, S.M. Woollard, J. Phys.: Condens. Matter. 21 (2009), 21, 364221.
- [19] J. Šebera, S. Nešpůrek, I. Kratochvílová, S. Zálíš, G. Chaidogiannos, N. Glezos, Eur. Phys. J. B 72 (2009) 385–395.
- [20] I. Kratochvílová, R. Škoda, J. Škarohlíd, P. Ashcheulov, A. Jäger, J. Racek, A. Taylor, L. Shao, J. Mater. Process. Technol. 214 (2014) 2600–2605.
- [22] F. Fendrych, A. Taylor, L. Peksa, I. Kratochvílová, J. Vlček, V. Řezáčová, V. Petrák, Z. Kluiber, L. Fekete, M. Liehr, M. Nesládek, J. Phys. D: Appl. Phys. 43 (2010), 374018.
- [23] A. Taylor, F. Fendrych, L. Fekete, J. Vlček, V. Řezáčová, V. Petrák, J. Krucký, M. Nesládek, M. Liehr, Diam. Relat. Mater. 20 (2011) 613–615.
- [24] R.H. Zhu, C.M. Li, L.X. Chen, J.L. Liu, J.J. Wei, L.F. Hei, H. Guo, Appl. Surf. Sci. 355 (2015) 203–208.
- [25] I. Kratochvílová, A. Kovalenko, F. Fendrych, V. Petráková, S. Zálíš, M. Nesládek, J. Mater. Chem. 21 (2011) 18248–18255.
- [26] Z. Wang, U. Garbe, H. Li, R.P. Harrison, K. Toppler, A.J. Studer, T. Palmer, G. Planchenault, J. Nucl. Mat. 436 (436) (2013) 84–92.
- [27] R. Velázquez, V.F. Neto, K. Uppireddi, B.R. Weiner, G. Morell, Coatings 3 (2013) 243–252.
- [28] A.C. Ferrari, J. Robertson, Phys. Rev. B 64 (2001) 085401–85414.
- [29] M. Krůželová, S. Vratislav, L. Kalvoda, M. Dlouhá, J. Phys. Conf. Ser. 340 (2012) 012095–012105.
- [30] L. Kalvoda, S. Vratislav, J. Hladil, M. Machek, Z. Kristall, Proc. 1 (2011) 113–118.
- [31] V.D. Vankar, N. Dilawar, Vaccum 47 (1996) 1275–1280.
- [32] Y.V. Butenko, S. Krishnamurthy, A.K. Chakraborty, V.L. Kuznetsov, V.R. Dhanak, M.R.C. Hunt, L. Šiller, Phys. Rev. B 71 (2005), 075420-1–075420-10.
- [33] P. Ashcheulov, J. Šebera, A. Kovalenko, V. Petrák, F. Fendrych, M. Nesládek, A. Taylor, Z. Vlčeková Živcová, O. Frank, L. Kavan, M. Dračinský, P. Hubík, J. Vacík, I. Kraus, I. Kratochvílová, Eur. Phys. J. B 86 (2013) 443–451.

- [34] M. Liehr, S. Wieder, M. Dieguez-Campo, *Thin Solid Films* 502 (2006) 9–14.
- [35] E. Barsoukov, J.R. Macdonald, *Impedance Spectroscopy: Theory, Experiment and Applications*, Wiley Interscience, 2005, pp. 17–18.
- [36] A.K. Jonscher, *J. Mater. Sci.* 16 (1981) 2037–2060.
- [37] P. Barberis, A. Frichet, *J. Nucl. Mat.* 273 (1999) 182–191.
- [38] Yanhua Lei, Toshiaki Ohtsuka, Nan Sheng, *Appl. Surf. Sci.* 357 (2015) 1122–1132.
- [39] I.H. Campbell, P.M. Fauchet, *Solid State Commun.* 58 (1986) 739–741.
- [40] J.L. Warren, J.L. Yarnell, G. Dolling, R.A. Cowley, *Phys. Rev.* 158 (1967) 805–808.
- [41] L. Fekete, K. Kúsová, V. Petrák, I. Kratochvílová, *J. Nanopart. Res.* 14 (2012), 1062(1)–1062(10).

ICONE24-60596

HIGH TEMPERATURE OXIDATION OF POLYCRYSTALLINE DIAMOND COATED ZIRCONIUM ALLOY

Jan Škarohlíd

Czech Technical University in Prague
Prague, Czech rep.

Radek Škoda

Czech Technical University in Prague
Prague, Czech rep.

Irena Kratochvílová

Institute of Physics
Czech Academy of Science

ABSTRACT

Polycrystalline diamond coating is a promising possibility for prevention, or reduction of high temperature oxidation of zirconium alloys and decrease corrosion rate of zirconium alloy during standard operation. Zirconium alloys are widely used as cladding and construction material in almost all types of nuclear reactors, where usually creates a barrier between nuclear fuel and cooling water in the primary circuit. Hydrogen and considerable amount of heat is released during steam oxidation that may occur in an eventual accident. In this paper zirconium alloy was covered by polycrystalline diamond layer using Plasma Enhanced Linear Antennas Microwave Chemical Vapor Deposition system reactor. X-Ray Diffraction and Raman spectroscopy measurements confirmed coverage of the surface area with crystalline and amorphous carbon layer. Characterizations (Raman spectroscopy) were done for zirconium alloy covered with polycrystalline diamond layer before and after high temperature steam exposure. Weight increase and hydrogen release were measured during steam exposure.

INTRODUCTION

Aim of this work was testing of Polycrystalline diamond (PCD) coatings on zirconium alloys in conditions of high temperature oxidation simulation accidental conditions of nuclear reactor. Two types of measurements were performed: online thermogravimetry (TG) (measurement of the mass changes caused by mass increase during oxidation) and mass spectrometry analysis of the off-gas released during high-temperature steam exposition. Both experiments were performed on coated and uncoated (reference) original cladding tube segments with a length varying from 5 to 20 mm.

Zirconium alloys are used as a fuel cladding and fuel assembly material in all commercial nuclear reactors due their acceptable mechanical properties, very low neutron capture, long term corrosion resistance and resistance against radiation damage.

Hence zirconium alloys are current standard as nuclear fuel cladding, its use is accompanied with some negative aspects as Pellet Cladding Interaction (PCI), Irradiation Assisted Stress Corrosion Cracking (IASCC), hydrogen uptake causing Delayed Hydride Cracking (DHC) and High-temperature Oxidation [1]. High-temperature oxidation is strongly exothermic reaction between zirconium and water, which occurs at temperatures above 600 °C. Hydrogen and considerable amount of heat is released during this reaction [2,3]. Damage of the cladding tube will lead to the contamination of primary circuit with radiotoxic isotopes of nuclear fuel, fission products and transuranics, and potential radioactivity release. Arisen hydrogen could explode and caused several damage of reactor vessel, primary circuit, containment, and reactor building. Released heat will strongly contribute to the potential core melting. All these we can saw during Fukushima accident in 2011.

Research effort heads for development of technologies, which prevent or diminish high temperature oxidation, by using protective coating layer or by using completely different material.

Polycrystalline diamond layer withstands very high temperatures, has excellent thermal conductivity and low chemical reactivity, it does not degrade over time and it has good neutron cross-section. Moreover, polycrystalline diamond layers consisting of crystalline (sp³) and amorphous (sp²)

carbon phases could have suitable thermal expansion. Polycrystalline diamond coating is a promising possibility for prevention, or reduction of high temperature oxidation of zirconium alloy.

Zirconium-alloys nuclear fuel cladding samples were successfully covered by a good quality polycrystalline diamond layers in our uniquely constructed Plasma Enhanced Linear Antennas Microwave Chemical Vapor Deposition system reactor [4].

EXPERIMENTAL

Two types of experimental devices were used for high-temperature steam expositions: BOX furnace and NETZSCH thermo-balance (TG).

BOX furnace allows steam exposition of coated samples at very high temperatures (up to 1600 °C) at steam flow-rates around 30 kg/hour. Outgoing gas was analyzed by GAM 300 quadrupole mass spectrometer with interest especially in hydrogen, steam, and argon concentrations. Special interest was in CO and CO₂ measurements on PCD coated samples in order to observe any changes in PCD structure at high temperatures.

Thermogravimetry experiments were performed at NETZSCH thermo-balance. Using argon as a cover gas. Simple alumina holder was used as sample support. All steam expositions were isothermal without any changes in steam or cover gas flow-rate. All oxidations were realized with argon flow-rate of 3 l/hour and with steam flow-rate of 3 g/hour. Measured thermogravimetric data were smoothed using moving average filter, in order to eliminate oscillations of thermo-balance apparatus.

Overall weight gain and off gas analysis were performed during both (BOX and TG) tests. In situ weight change was measured during TG test.

Overall weight gain w_g was determined from measured sample weight before (w_0) and after (w_1) the oxidation. Weight gain was then determined as sample weight difference before and after exposition normalized by sample surface, which was exposed to high temperature steam. Sample surface was calculated from sample dimensions (length, inner and outer diameter) measured before steam exposition. Equivalent cladding reacted (ECR) (in %) was calculated using formula [5]:

$$ECR = \frac{87,8 \cdot w_g}{s [cm]}$$

Where s is wall thickness of the sample.

Off-gas analysis was performed on GAM 300 quadrupole mass spectrometer. Hydrogen concentration and overall hydrogen production was calculated from measured concentration data using simple code programed in Octave

software. Hydrogen flow-rate was calculated from measured data using formula:

$$m_H(t) = \frac{c_H(t)}{c_{Ar}(t)} \cdot m_{Ar}$$

where m_H and m_{Ar} are volumetric flow-rates of hydrogen and argon and c_H and c_{Ar} are mass concentrations of hydrogen and argon measured in outgoing gas by mass spectrometer. Overall hydrogen production was then calculated as integral of hydrogen flow-rate. Hydrogen production was normalized to sample surface area to compensate different sizes of samples.

$$H = \int_{t_0}^{t_n} m_H(t) dt$$

RESULTS

Temperatures 900, 1000, 1100 and 1200 °C were chosen for thermogravimetric measurements. Measured data of weight gain and calculated data of ECR and overall hydrogen production are summarized at the table (Tab. 1) for coated and uncoated reference samples.

Tab 1: PCD thermogravimetry data

Temp.	Time	Weight gain		ECR		Hydrogen produced	
[°C]	[min]	[g.dm ⁻²]		[%]		[l.dm ⁻²]	
		Coated	Reference	Coated	Reference	Coated	Reference
900	60	0,55	0,64	8,45	9,90	0,56	0,69
1000	60	2,14	2,87	32,97	44,19	2,20	3,44
1100	60	3,83	3,98	59,05	61,35	4,69	4,96
1200	20	4,73	4,41	72,85	67,95	5,81	5,28

Weight gain time dependences, measured by NETZSCH thermo-balance at different temperatures from 900 °C to 1200°C are on Fig.1.

Oxidation kinetics of PCD coated samples is similar to kinetics of uncoated samples at almost all temperatures, but with lower hydrogen production and lower weight gains. Most important difference is in later beginning of breakaway oxidation at 1000°C, when breakaway oxidation starts on PCD coated sample 15 minutes later.

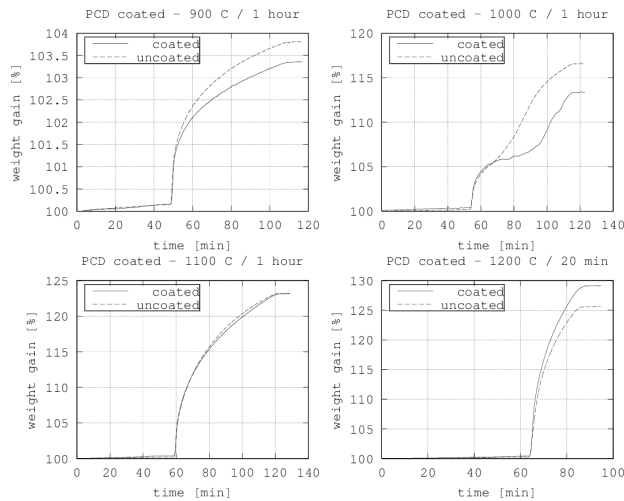


Fig. 1: PCD thermogravimetric data

Special test with sample pre-oxidation was performed in order to see any changes (if they occur) in structure of PCD layer at temperatures below 800 °C. Pre-oxidation phase at 500 °C and 700 °C for 20 minutes was chosen, before exposing the sample to steam at 1000 °C. No steam was introduced to the furnace during changes of temperature. TG data are at Fig.2. Sample with higher (700 °C) temperature of pre-oxidation phase has lower weight gain and hydrogen release in main oxidation phase, what is probably caused by thicker oxide layer developed during pre-oxidation phase. No significant failure of PCD layer was observed during pre-oxidation phase.

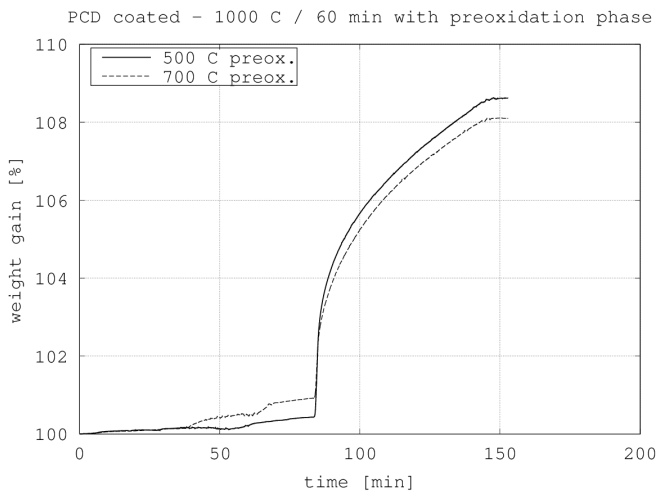


Fig. 2.: TG data with preoxidation phase

Very high temperature test was performed in BOX furnace. Exposition parameters were set as follows: temperature – 1400 °C, time – 6 min., argon flow-rate – 30 l/hour, steam flow-rate – 40 g/hour. Time was determined after previous calculation using Carthcarth – Pawel correlation in order to avoid complete oxidation of the sample. Data are summarized in Tab.2.

Tab.2. Steam oxidation at 1400 °C

Substrate	Coating	Weight gain	ECR	Hydrogen produced
		[g.dm ⁻²]	[%]	[l.dm ⁻²]
Zirlo	PCD	4,91	75,55	3,95
Zirlo		3,13	48,21	2,59

Two samples from Zircaloy-2 were oxidized at 1200 °C for two times 30 minutes. One sample was coated with PCD and one was left uncoated. After first 30 minutes in steam were samples cooled down in inert argon atmosphere and removed from BOX furnace. Sample was than returned back to furnace after measuring of weight gain. Measured data are in Tab.3.

Tab.3. Weight gain and hydrogen production during 2×30 min at 1200 steam exposure.

Substrate	Coating	Weight gain		ECR		Hydrogen produced
		[g.dm ⁻²]		[%]		[l.dm ⁻²]
		30 min	60 min	30 min	60 min	60 min
Zry-2	PCD	3,41	5,45	48,72	77,82	5,99
Zry-2		3,56	5,48	50,75	78,29	7,42

SAMPLES EVALUATION

Exposed samples were than observed using Raman spectroscopy and cross-section optical microscopy. Polycrystalline diamond films quality was investigated using Raman spectroscopy. Raman spectroscopy was performed on all tube samples coated with polycrystalline diamond (PCD) film prior and after high temperature oxidation tests to gain insight on diamond layer changes during oxidation. All measurements were carried out at room temperature using a Renishaw InVia Raman Microscope. The conditions used were as follows: Laser excitation wavelength of 488 nm (25 mW), x50 Olympus objective, 65 μm slits, spot focus, grating of 2400 l/mm.

Raman spectroscopy measurements on the PCD coated with PCD film revealed the existence of peaks related to sp³ diamond (1332 cm⁻¹) and sp² – containing graphitic carbon (1600 cm⁻¹) phases. Measurements taken at positions over the entire surface of the cladding tube showed diamond growth and incorporation of amorphous carbon and graphite (Fig. 3).

After oxidation at 900°C, 1000 °C and 1100 °C a mixture of sp² carbon, sp³ carbon (diamond) and graphite-related features are visible. At 1200 °C steam exposed sample a complete transition to the graphite-related content is evident by

a narrowing of the peak widths. A weak signal sample at 1400 °C suggests the rapid transition of the diamond coating to various carbon phases.

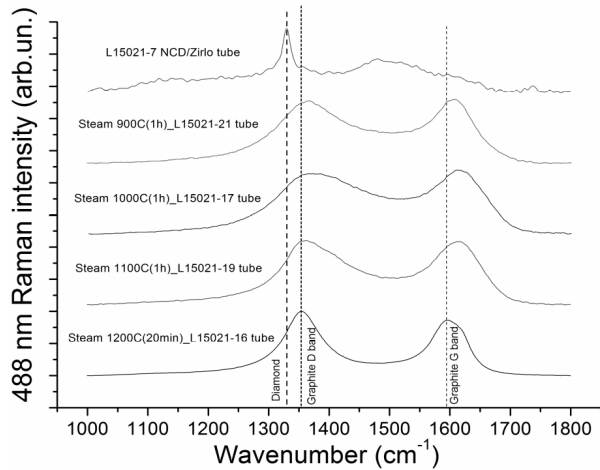


Fig. 3: Raman spectroscopy results

Optical microscopy reveals oxide grows below PCD layer on outer surface. Oxidation rate is lower on the outer tube surface which was protected by thin PCD nanocrystal layer, then on the inner unprotected surface. Optical cross-section microscopy, with measurements of zirconium dioxide thicknesses is on Fig. 4.

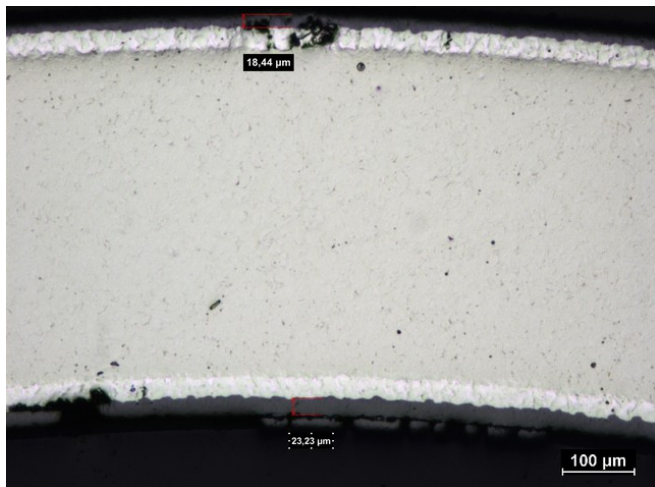


Fig. 4. Optical cross-section microscopy of PCD coated sample exposed at 900 °C for 60 min.

CONCLUSIONS

Oxidation kinetics of PCD coated samples is similar to kinetics of uncoated samples at almost all temperatures, but with lower hydrogen production and lower weight gains. Most important difference is in later beginning of breakaway oxidation at 1000 °C, when breakaway oxidation starts on PCD coated sample 15 minutes later.

Raman spectroscopy revealed graphitization of the PCD layer and the diamond sp^3 bounds are lost and the Raman signal consists only from the two graphite-related D bands. It implies conversion of PCD layer to the homogeneous non-crystalline carbon layer with a large content of graphitic phase. Overall hydrogen production and weight gain values are generally lower than for uncoated samples.

Coated samples show worse results in all measured values at temperature 1400 °C than uncoated samples. That should estimate, that before coating failure, no or only very thin zirconium oxide layer is developed on metal surface. This is the reason of more intense reaction.

ACKNOWLEDGMENTS

Authors would like to acknowledge financial support from EU GENTLE and Technology Agency of the Czech Republic, projects TA4020156 and TE01020455 – CANUT. Zirconium material was kindly provided by Westinghouse Electric. PCD coatings were deposited at Institute of Physics of Czech Academy of Science. High-temperature oxidations were realized at Karlsruhe Institute of Technology – Institute of Applied Materials.

REFERENCES

- [1] Konings, R., 2012, “Comprehensive nuclear materials”, Elsevier
- [2] Steinbrück, M., 2011, “Oxidation of Advanced Zirconium Cladding Alloys in Steam at Temperatures in the Range of 600–1200 °C,” *Oxid. Met.*, DOI:10.1007/s11085-011-9249-3.
- [3] Škarohlíd, J.; Škoda, R.; Kazda, R., 2013, “Problematics of high-temperature oxidation of zirconium,” (in czech) *Bezpečnost jaderné energie*, 2013, 21(59), pp 298-301.
- [4] Fendrych, F.; et al., 2010, “Growth and characterization of nanodiamond layers prepared using the plasma-enhanced linear antennas microwave CVD system,” *J. Phys. D: Appl. Phys.* 43 , 374018
- [5] U.S.NRC – NUREG 6967 – Cladding Embrittlement During Postulated Loss-of-Coolant Accidents, July 2008

SCIENTIFIC REPORTS



OPEN

Nanocrystalline diamond protects Zr cladding surface against oxygen and hydrogen uptake: Nuclear fuel durability enhancement

Jan Škarohlíd¹, Petr Ashcheulov², Radek Škoda¹, Andrew Taylor², Radim Čtvrtlík³, Jan Tomáščík³, František Fendrych², Jaromír Kopeček¹, Vladimír Cháb², Stanislav Cichoň², Petr Sajdl⁴, Jan Macák⁴, Peng Xu⁵, Jonna M. Partezana⁶, Jan Lorinčík⁷, Jana Prehradná¹, Martin Steinbrück⁸ & Irena Kratochvílová²

In this work, we demonstrate and describe an effective method of protecting zirconium fuel cladding against oxygen and hydrogen uptake at both accident and working temperatures in water-cooled nuclear reactor environments. Zr alloy samples were coated with nanocrystalline diamond (NCD) layers of different thicknesses, grown in a microwave plasma chemical vapor deposition apparatus. In addition to showing that such an NCD layer prevents the Zr alloy from directly interacting with water, we show that carbon released from the NCD film enters the underlying Zr material and changes its properties, such that uptake of oxygen and hydrogen is significantly decreased. After 100–170 days of exposure to hot water at 360 °C, the oxidation of the NCD-coated Zr plates was typically decreased by 40%. Protective NCD layers may prolong the lifetime of nuclear cladding and consequently enhance nuclear fuel burnup. NCD may also serve as a passive element for nuclear safety. NCD-coated ZIRLO claddings have been selected as a candidate for Accident Tolerant Fuel in commercially operated reactors in 2020.

To satisfy the demands for safe operation and to extend the lifetime of nuclear fuel, it is necessary to decrease the surface corrosion of zirconium fuel claddings. Zirconium alloys are standard structural materials used in the cores of water-cooled nuclear power reactors^{1–5}. A significant problem is posed by the dissociation of water molecules at the surface of a zirconium alloy, even at standard operating temperatures, thus allowing both oxygen and hydrogen to penetrate into the alloy. As the alloy oxidizes and zirconium hydrides form, the ductility of the nuclear rod decreases. Oxygen and hydrogen uptake into the Zr alloy changes the mechanical properties of the core components, which are important criteria for the licensing of nuclear fuel^{4–7}. Thus, the protection of the surfaces of zirconium fuel rods against corrosion in nuclear reactor environments may significantly prolong nuclear fuel usage^{8–14}. Recently, many typically homogeneous materials have been applied to protect the surfaces of zirconium alloys against direct interaction with water molecules, but the majority of these efforts have not met with significant success^{5–7}.

In this work, we demonstrate and describe a novel means of protecting ZIRLO surfaces against O and H uptake at both accident and working temperatures in water-cooled nuclear reactor environments. Tubular ZIRLO fuel claddings (tubes) and ZIRLO plates were protected by thin (300–700 nm) composite nanocrystalline diamond (NCD) layers deposited onto the ZIRLO surfaces with a microwave plasma-enhanced linear antenna

¹Czech Technical University in Prague, Faculty of Mechanical Engineering, Technická 4, Prague 6, CZ-160 07, Czech Republic. ²Institute of Physics of the Czech Academy of Sciences, Na Slovance 2, CZ-182 21, Prague 8, Czech Republic. ³RCPTM, Joint Laboratory of Optics of Palacký University in Olomouc and Institute of Physics of the Czech Academy of Sciences, 17. listopadu 12, CZ-771 46, Olomouc, Czech Republic. ⁴University of Chemistry and Technology, Power Engineering Department, Technická 3, Prague 6, CZ-166 28, Czech Republic. ⁵Nuclear Fuel Division, Westinghouse Electric Company, 5801 Bluff Road, Hopkins, SC, 29209, USA. ⁶Westinghouse Churchill Site, 1332 Beulah Rd., Pittsburgh, PA, 15235, USA. ⁷Research Centre Řež, Hlavní 130, CZ-250 68, Husinec-Řež, Czech Republic. ⁸Institute for Applied Materials (IAM), Karlsruhe Institute of Technology, Hermann-von-Helmholtz-Platz 1, 76344, Eggenstein-Leopoldshafen, Germany. Correspondence and requests for materials should be addressed to I.K. (email: krat@fzu.cz)

Sample type	NCD layer thickness (nm)	Weight gain (mg/dm ²) of autoclaved samples							
		6 days	15 days	30 days	90 days	120 days	150 days	170 days	195 days
Tube	300	9.4	15.5	19.6	33.3	31	30	41	—
Tube	500	7.7	13.6	19.1	31.5	—	—	—	—
Plate	300	5.4	9.3	14.1	27.1	29	38	40	52
Plate	500	4.8	5.4	9.4	20.6	—	—	—	—
Tube	0	15.1	20.6	26.2	40.3	52	66	68	—
Plate	0	13.0	18.1	23.7	37.3	52	65	70	79

Table 1. Weight gains (mg/dm²) measured after autoclave tests of uncoated ZIRLO samples (tubes and plates) and samples coated with 300 or 500 nm of NCD. The samples were processed in 360 °C hot water for 6, 15, 30, 90, 120, 150, 170, and 195 days under primary circuit conditions in a PWR in accordance with ASTM standard procedures²¹. The greater relative weight gain of the uncoated ZIRLO plates and tubes indicated stronger oxidation of the unprotected surfaces.

chemical vapor deposition (MW-LA-PECVD) apparatus^{15–18} (Fig. S1). NCD layers have a high thermal conductivity, provide environmental stability and exhibit low chemical reactivity^{16,17}. As we have previously shown^{15–17}, NCD layers are able to adhere to Zr alloy surfaces at high temperatures and possess suitable thermal expansion properties.

The behavior of NCD coated Zr alloy in a neutron flux environment was simulated by Fe ion beam irradiation. After Fe²⁺ beam irradiation (10 displacements per atom/dpa, 3 MeV Fe²⁺, fluency of $1.95 \times 10^{16} \text{ cm}^{-2}$), and hot steam processing NCD films grown in the MW-LA-PECVD apparatus have been shown to exhibit structural integrity¹⁶. The diamond radiation damage dose dependence was shown in refs 19 and 20. In ref. 19 the effects of neutron irradiation ((1–5). 10^{20} cm^{-2} fluence range) on chemical vapor deposited diamond were investigated. Despite an increase in unit-cell volume (4.5%) the crystalline structure remain stable¹⁹. In the case of X-ray study of neutron irradiated diamonds²⁰ (4.8 and $16.3 \times 10^{20} \text{ cm}^{-2}$ fluence) the irradiated diamond density decrease (accompanied by structural changes) was in majority cases between 12 and 25%, with the average of 17%.

The NCD grown in the MW-LA-PECVD apparatus is a composite material: it consists of diamond grains (sp³-hybridized phase, >96%) and graphite (sp² phase)¹⁵. Such NCD layers with thicknesses from 300 nm to 700 nm have been found to significantly decrease oxygen and hydrogen uptake into ZIRLO fuel tubes and plates processed in Westinghouse Electric Company facilities, in accordance with ASTM standard procedures (360 °C, hot water exposure for 6 days up to 195 days)²¹. In addition, we evaluated NCD's protective performance for 4 days in hot steam at 400 °C (15 MPa, less than 10 ppb of oxygen) and at extremely high steam temperatures of 900–1100 °C for 1 hour and 1200 °C for 30 min.

We extensively studied and interpreted the detailed role of NCD layers in preventing the penetration of oxygen and hydrogen into ZIRLO surfaces and hindering Zr oxidation, by using several different characterization methods: X-ray photoelectron spectroscopy (XPS), Raman spectroscopy, scanning electron microscopy (SEM), energy-dispersive spectroscopy (EDS), thermogravimetry, mass spectrometry, secondary ion mass spectrometry (SIMS), capacitance measurements and NanoESCA. The relevance of each of these techniques with respect to the subject of this research are discussed in refs 22–32. The adhesion of the protective NCD layers on the nuclear fuel cladding surfaces before and after oxidation due to exposure to hot steam and water was investigated through analysis of the mechanical and tribological properties of the samples. This analysis was conducted on the basis of the approaches presented in refs 31–34. We demonstrated that because of the specific composition of the NCD, carbon atoms from an NCD layer enter the underlying Zr material and significantly modify its structural, chemical and physical parameters in a favorable fashion. These changes result in lower uptake of hydrogen and oxygen into the ZIRLO, thereby leading to lower degradation of fuel tubes and plates in hot steam or water environments.

In this paper, we show that at high temperatures (up to 1200 °C), NCD layers can fully serve as passive elements for nuclear safety. NCD layers provide crucial and effective protection against Zr alloy oxidation and hydration under standard reactor operating conditions (360 °C, hot water, ASTM standard procedures)²¹. Such protective NCD layers can prolong the lifetime of nuclear cladding and, consequently, enhance nuclear fuel burn-up. However, the main novelty and relevance of this work lie in providing a fundamental explanation of the causes of the astonishingly high corrosion prevention of Zr alloys, which is achieved through the deposition of composite NCD layers. Despite long-term exposure to a corrosive environment and specific nature of the heterogeneous NCD material (diamond and graphitic phases), the anti-corrosive effect of such protective NCD layers is very significant. On the basis of a wide range of analyses, we describe in detail the complex and specific mechanism by which heterogeneous NCD layers protect ZIRLO surfaces against corrosion.

Results

Weight gain of samples after hot steam or hot water processing. To determine the protective capabilities of NCD layers under standard reactor conditions, ZIRLO samples (tubes and plates) coated with 300 nm, 500 nm and 700 nm NCD layers were processed in hot water at 360 °C for durations ranging from 6 days up to 195 days (processed in a pressurized water reactor (PWR), in accordance with ASTM standard procedures)²¹. After these tests, the ZIRLO samples were found to still be coated with their protective NCD layers (confirmed through Raman spectroscopy and SEM imaging, as shown below). Table 1 and Fig. 1 display the weight gains of standard and NCD-protected ZIRLO tubes and plates after processing in hot water (360 °C). The weight gain was determined as the difference in the sample weight before and after oxidation, normalized to the total exposed area

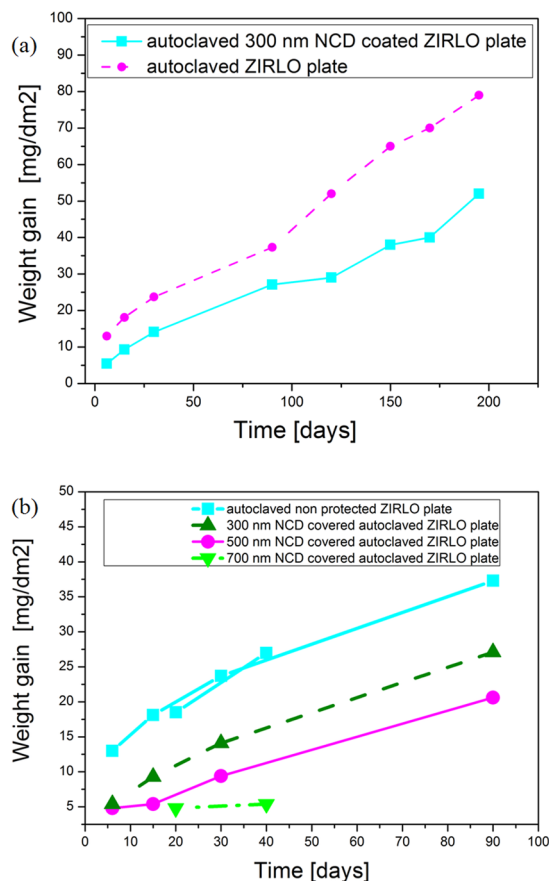


Figure 1. (a) weight gains (mg/dm^{-2}) measured after 6, 15, 30, 90, 120, 150, 170 and 195 days of exposure to hot water (360°C) for uncoated and 300 nm NCD-coated ZIRLO plate samples. (b) weight gains (mg/dm^{-2}) measured after 6, 15, 20, 30, 40 and 90 days of exposure to hot water (360°C) for uncoated, 300 nm NCD-coated, 500 nm NCD-coated and 700 nm NCD-coated ZIRLO plate samples. Thicker NCD layers provide ZIRLO plates with stronger protection against oxidation than thinner layers do.

of the sample surface. According to¹², these weight gains are caused by oxidation and hydrogen uptake into the samples. The weight gains were measured after the hot water processing (360°C) of ZIRLO samples with NCD coatings (300 nm, 500 nm or 700 nm) and uncoated ZIRLO samples. For all of the hot-water-processed samples, the NCD-coated Zr samples showed lower weight gains compared with those of the uncoated samples (Table 1 and Fig. 1). Similar results were observed after 4 days of exposure to hot steam (400°C): the weight gain for a ZIRLO sample coated with a 300 nm NCD layer was $7.8 \text{ mg}/\text{dm}^2$, whereas the weight gain for an uncoated ZIRLO sample was $13.2 \text{ mg}/\text{dm}^2$. All weight gains were subject to an uncertainty (experimental plus numbers rounding) of less than 2%.

Table 1 and Fig. 1 show that in the case of the thickest (700 nm) NCD coatings, the smallest oxidation (weight gain) of the protected ZIRLO was measured. For ZIRLO plates coated with 700 nm NCD layers, the surface oxidation/weight gain was decreased by more than 50% compared with that of the non-protected ZIRLO plates. The weight gains of ZIRLO plates coated with 700 nm NCD and uncoated ZIRLO plates after exposure to 360°C hot water for 20 days were $4.8 \text{ mg}/\text{dm}^2$ and $18 \text{ mg}/\text{dm}^2$, respectively. When the exposure was prolonged to 40 days, the same trend was observed: the weight gain was $5.4 \text{ mg}/\text{dm}^2$ for ZIRLO plates coated with 700 nm NCD and $31 \text{ mg}/\text{dm}^2$ for uncoated ZIRLO plates. From Table 1 and Fig. 1, a systematic decrease in weight gain was evident for ZIRLO plates coated with 300 nm, 500 nm and 700 nm of NCD.

In the case of ZIRLO plates that were mounted vertically in the deposition chamber, all surfaces were covered with more homogeneous NCD layers compared with those coating the ZIRLO tubes¹⁵. This observation was because the inner surfaces of the ZIRLO tubes were not fully covered by the NCD (as confirmed by SEM imaging and Raman spectroscopy), as the plasma was unable to fully penetrate into a tube's internal structure. Therefore, an apparent decrease in corrosion resistance was observed for the ZIRLO tubes. These results demonstrate the importance of coating homogeneity. For this reason, the results obtained for the NCD-coated ZIRLO plates are more representative (Table 1 and Fig. 1). In practice, during NCD growth in the MW-LA-PECVD apparatus, both ends of each tube could be closed with metallic closures to prevent the inner part of the tube from being coated with an NCD layer.

For the samples processed in hot water (360°C) for 90 days, the hydrogen concentrations were measured by means of mass spectrometry. The obtained results showed that uncoated ZIRLO tubes had a higher

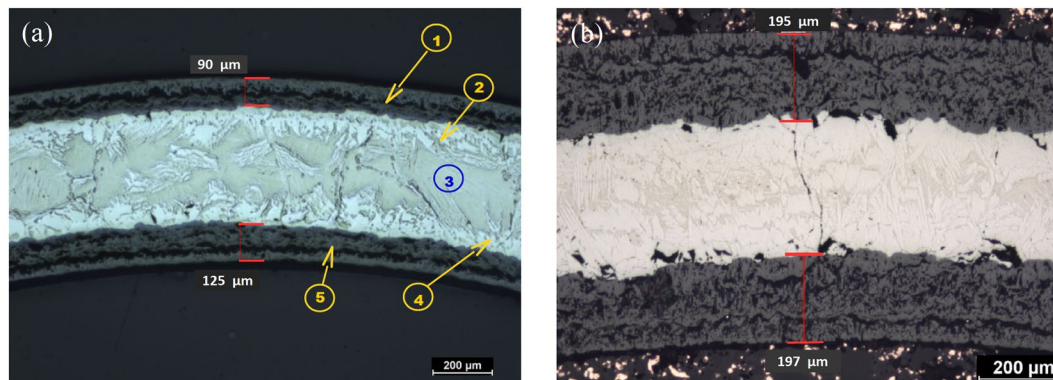


Figure 2. Optical microscopy images of the metallographic cross sections. (a) a 300 nm NCD-coated ZIRLO tube sample processed at 1000 °C in hot steam. (1) Outer-surface zirconium dioxide layer, with a thickness of 90.8 μm. (2) Outer-surface oxygen-stabilized zirconium α phase (solid Zr-O solution). (3) Initial Zr β phase (metastable modified hexagonal close-packed structure). (4) Inner-surface oxygen-stabilized Zr α phase. (5) Inner-surface ZrO₂ layer, with a thickness of 125.02 μm. (b) an uncoated ZIRLO tube sample subjected to hot steam (1000 °C/1 h). On the outer surface of the tube, the ZrO₂ thickness was 195.13 μm; on the inner surface, the ZrO₂ thickness was 196.8 μm.

hydrogen concentration (37 ppm) compared with 500 nm NCD-coated ZIRLO tubes (31 ppm) and plates (21 ppm) (Table S1). The same analysis was conducted for uncoated and 300 nm NCD-coated ZIRLO tubes after hot steam processing (1100 °C for 60 min and 1200 °C for 20 min) (Table S2). The highest hydrogen concentration was found in the uncoated samples (Table S1). For hot steam processing at temperatures above 900 °C, the uptake of hydrogen into the unprotected material was very high (Table S3). Compared with ZIRLO samples protected with 500 nm of NCD, the hydrogen concentration in the unprotected ZIRLO samples was found to be larger by one order of magnitude (Table S3). The relative standard deviation of the hydrogen concentrations was less than 6.4%. The precision of all hydrogen concentration measurements was 0.5% (mass spectrometer model: G8 GALILEO).

Mechanical and tribological measurements. NCD layers exhibit stable and strong adhesion to ZIRLO surfaces, protecting them from direct interaction with water. The improvement in the scratch resistance of a ZIRLO plate after the application of an NCD coating (300 nm thick) is shown in Fig. S2, in which on-load depth measurements are presented for uncoated and NCD-coated ZIRLO before and after hot steam processing (400 °C, 4 days). Because of the higher hardness of the NCD (approx. 18.5 GPa), a low depth profile was clearly seen for the NCD-coated ZIRLO substrate. ZIRLO, by contrast, is a softer material with a lower scratch resistance. The formation of zirconium oxide on the surface of ZIRLO during exposure to hot steam improved its scratch resistance. However, the adhesion of this oxide layer was poor, thus leading to sudden ZrO₂ failure and delamination, exposing the underlying ZIRLO; note the sudden drop in depth at a scan distance of ~330 μm. The critical load was approximately 370 mN. In the case of the NCD-coated ZIRLO, there were no signs of such failure after hot steam exposure. Analysis of the residual wear track also revealed a lower level of cracking. Similar results were obtained for ZIRLO tubes coated with 700 nm thick NCD films. Notably, a 500 nm thick NCD layer was found to provide less protection than a 700 nm layer.

The deposition of the 300–700 nm thick NCD layers improved the mechanical stability and overall integrity of the ZIRLO during and after hot water/steam exposure and provided an extra level of mechanical durability. In summary, the scratch resistivity of NCD-protected ZIRLO remained unchanged after 4 days of exposure to hot steam at 400 °C.

Thermogravimetry, mass spectrometry and optical microscopy of the metallographic cross sections of samples. Thermogravimetry experiments were performed to measure the mass changes occurring during high-temperature steam oxidation. Furthermore, off-gas analysis was performed to measure hydrogen production (Table S1). After exposure for 60 min at 900 °C, 1000 °C, or 1100 °C in hot steam, the 300 nm NCD-coated ZIRLO samples were still covered with an NCD layer (as confirmed by Raman spectroscopy and SEM imaging). The weight gains were measured after the hot steam tests for the NCD-coated and unprotected ZIRLO samples. After hot steam exposure, higher relative weight gain (surface oxidation) and hydrogen production were measured for the uncoated ZIRLO samples compared with the NCD-coated ZIRLO samples. After exposure at 1100 °C, the amount of hydrogen in the uncoated samples was approximately 571 ppm, whereas for the NCD-coated samples, this value was decreased to 51 ppm (Table S3). The oxygen concentration in the outgoing gas/high-temperature steam (above 900 °C) was less than 0.08%.

Metallographic cross sections (Fig. 2) of NCD-coated (300 nm) and uncoated ZIRLO tubes after exposure to hot steam (1000 °C) for 1 h were obtained with an optical microscope. Metallographic cross-section analysis allowed oxides and different zirconium phases to be distinguished. As discussed earlier, the inner parts of the tubes were not as effectively coated with NCD compared with the outer surfaces. For this reason, a thinner layer of ZrO₂ was measured on the outer surface of the tube depicted in the figure (90.80 μm) compared with the inner surface (125.02 μm). However, both of these values were significantly less than those for an uncoated ZIRLO tube

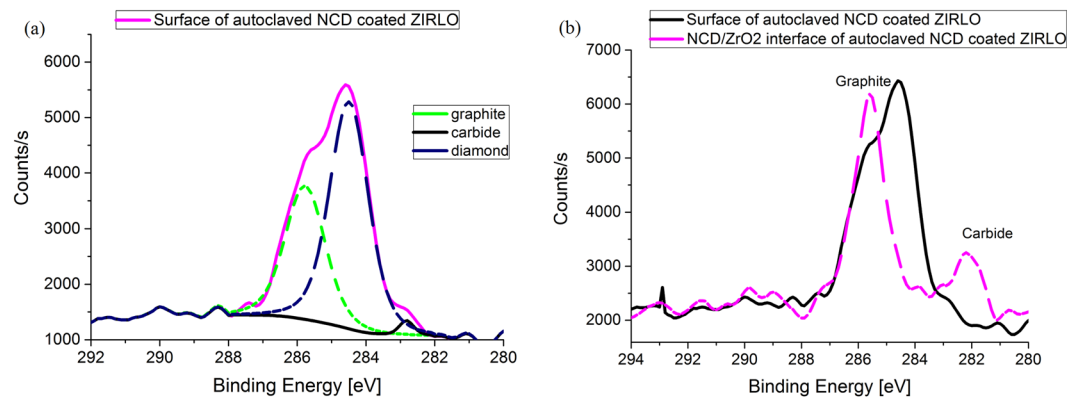


Figure 3. C1s lines of ZIRLO coated with NCD after calibration on the basis of the Zr 3d5/2 line. The areas analyzed were on the NCD surface and at the NCD/ZrO₂ interface after hot steam exposure (400 °C, 4 days). Four different states of carbon are evident (a): graphite, with a binding energy of 285.4 eV; diamond, with a binding energy of 284.2 eV; carbon in a single bond with oxygen, with a binding energy of 286.1 eV; and carbide, with a binding energy of 282 eV. Carbides were also present below the NCD layer (b).

(195.13 μm on the outer surface and 196.8 μm on the inner surface) exposed to the same conditions. These values confirmed the protective effect of the NCD layers.

X-ray photoelectron spectroscopy. The protective capabilities of the NCD layers were further evidenced by XPS data acquired from the NCD-coated (300 nm) and uncoated ZIRLO tubes before and after hot steam tests (in an autoclave for 4 days at 400 °C). The XPS spectra were obtained from cross sections of the samples. The results of the XPS analysis can be divided into two parts: the results of a quantitative analysis performed on the surface of each cross section at the metal-to-oxide interface and the results of an analysis of the states of carbon identified to be present in the metal and oxide layers.

Regarding the analysis of the carbon states, the presence of carbides and forms of carbon with a binding energy near 285 eV was determined from the detailed spectra of the C1s peak. The Zr 3d5/2 line of metallic zirconium (179 eV) was used as the calibration standard because of the low level of surface charging.

The presence of carbide in the ZrO₂ layer was identified from the existence of a line with a binding energy of 281.6 eV. The difference in the carbon binding energy peaks for autoclaved NCD-coated ZIRLO compared with autoclaved uncoated ZIRLO was 0.8 eV, which was reproducibly observed in many spectra. At least two carbon states (with different binding energies) were identified in the autoclaved NCD-coated ZIRLO, as indicated by the structure of the main part of the C1s line.

In total, four states of carbon were identified: graphite (Fig. 3), with a binding energy of 285.4 eV; diamond, with a binding energy of 284.2 eV; carbon in a single bond with oxygen, with a binding energy of 286.1 eV; and carbide, with a binding energy of 282 eV. The binding energies of graphite and diamond are relatively close to each other. These two carbon states were resolved on the basis of a set of spectra measured at several different locations in the samples. The difference in the positions of the two lines may also be the result of electrical charging, which might occur slightly differently for the two carbon forms.

The surface layer of an autoclaved uncoated ZIRLO tube was found to be chemically composed mainly of ZrO₂, thus suggesting a large uptake of oxygen. Furthermore, after autoclaving, the amount of oxygen at the surface for uncoated ZIRLO (25%) was higher than that for the NCD-coated ZIRLO samples (14%). The uncoated autoclaved samples also contained a larger number (compared with the NCD-protected autoclaved samples) of oxygens in non-stoichiometric positions – i.e., during hot steam processing (4 days, 400 °C), oxygen defects formed in the surface layer of the uncoated ZIRLO in higher numbers than in the NCD-coated ZIRLO samples.

After the autoclaving of the NCD-coated ZIRLO samples, carbides were detected in the ZrO₂ layer and in the Zr alloy (i.e., beneath the oxide layer). In conclusion, after the autoclave tests, the Zr surfaces of the NCD-coated ZIRLO samples were significantly affected by the presence of the NCD layer, and the effects manifested as a higher concentration of carbides and a lower concentration of oxygen. Carbides were also found in the underlying Zr alloy.

Raman spectroscopy, scanning electron microscopy, and energy-dispersive spectroscopy. The Raman spectra of the surfaces of NCD-coated ZIRLO tubes before and after exposure to hot water (360 °C) for 6 days, 15 days and 30 days are shown in Fig. 4. The spectrum of the as-deposited NCD layer showed a sharp 1332 cm⁻¹ peak originating from diamond along with peaks attributed to non-diamond phases. The broad band visible at 1400–1550 cm⁻¹ is a signature of amorphous carbon located within the grain boundaries, the band visible at ~1580 cm⁻¹ was assigned to graphite, and the ~1620 cm⁻¹ peak was attributed to the presence of “graphite-like” disordered carbon. After 6 days of autoclave exposure to hot water (360 °C), the 1350 cm⁻¹ peak became visible in the spectrum, thus indicating the partial transformation of graphite into a disordered phase. With the further increase of the hot water exposure time (to 15 and 30 days), the Raman spectra of the NCD layers showed an increase in intensity and a broadening of the amorphous-carbon-related band (1400–1550 cm⁻¹) and of the graphite and disordered graphite (1350 cm⁻¹) peaks; these observations indicated an increasing amount

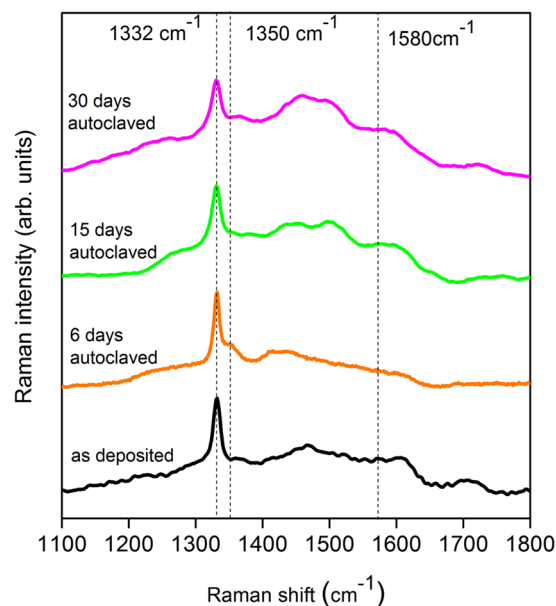


Figure 4. Measured 488 nm Raman spectra of 300 nm thick NCD layers on ZIRLO tubes, as deposited and after 6, 15 and 30 days of exposure to hot water at 360 °C. The 1332 cm^{-1} peak is typical of diamond. The broad band visible at 1400–1550 cm^{-1} is a signature of amorphous carbon located within the grain boundaries, the band at $\sim 1580 \text{ cm}^{-1}$ was assigned to graphite, and the $\sim 1620 \text{ cm}^{-1}$ peak was attributed to the presence of “graphite-like” disordered carbon.

of “disorganized” carbon in the layers along with a partial transformation of sp^3 carbon into the sp^2 phase^{17, 18, 35}. The Raman spectroscopy results also confirmed that the NCD layers on ZIRLO withstood exposure to hot steam (900–1100 °C) for 1 h without exhibiting significant changes.

SEM revealed no important changes in the thicknesses of NCD layers subjected to hot water (360 °C) autoclaving (Fig. 5). Moreover, no microstructural changes were found in 300 nm NCD films processed in hot water for 30 days (Fig. 6).

The compositional effects of processing in hot steam (4 days at 400 °C) were studied by means of EDS in focused ion beam (FIB)-milled trenches. In the case of unprotected ZIRLO, the surface contained $18 \pm 1 \text{ at.}\% \text{ O}$, the oxidized ZrO_2 layer contained $33 \pm 2 \text{ at.}\% \text{ O}$, and the bulk alloy contained $6.4 \pm 0.5 \text{ at.}\% \text{ O}$. A sample protected with a 300 nm NCD layer contained $15 \pm 1 \text{ at.}\% \text{ O}$ at the surface, $19 \pm 1 \text{ at.}\% \text{ O}$ in the oxidized ZrO_2 layer, and $6.2 \pm 0.5 \text{ at.}\% \text{ O}$ in the bulk alloy (Table S4). The thickness of the oxidized zone in the unprotected ZIRLO sample after treatment was $2.16 \pm 0.05 \mu\text{m}$. For the NCD-coated ZIRLO, this thickness was decreased to $1.7 \pm 0.05 \mu\text{m}$.

These results showed that the NCD layer suppressed the formation of the oxide layer after exposure to hot steam; i.e., the oxidized layer grew more rapidly on unprotected ZIRLO.

In addition, Raman spectroscopy and SEM confirmed that the outer surfaces of tube samples were more effectively coated with high-quality 300 nm NCD layers (thicker and more homogeneous NCD films and a larger relative amount of sp^3 -hybridized C), as compared with the inner surfaces of the tubes (an estimated 40% of the inner surface was covered with a thinner NCD film of only 80 to 120 nm in thickness) (Fig. S3).

Secondary ion mass spectrometry. SIMS is notable among chemical-analytical methods in that it combines high sensitivity and distinguishing capabilities with the capacity to analyze all elements and isotopes in the periodic table²³. We used SIMS to determine the changes in the C depth profile of a 300 nm NCD-coated ZIRLO tube before and after 4 days of exposure to 400 °C hot steam. The SIMS data showed that after 4 days at 400 °C in hot steam, a large amount of C was contained in the ZrO_2 layer formed beneath the protective NCD layer. The exposure to hot steam clearly resulted in the diffusion of carbon into the ZrO_2 layer to a depth larger than $1.5 \mu\text{m}$ (Fig. 7a). In a reference NCD-coated ZIRLO sample (not exposed to hot steam), the majority of the carbon atoms were contained within the thickness of the NCD layer itself (Fig. 7b). The depth profiles of C and O are in units of counts/s and labelled in the graphs.

Capacitance measurements and NanoESCA analysis. Capacitance measurements were performed on uncoated ZIRLO tubes before and after hot steam exposure (400 °C for 4 days) and on 300 nm NCD-coated ZIRLO tubes exposed to the same hot steam conditions. The types and densities of the defects in the surface films were determined (Table S5). Because a balance must be established between the metal and semiconductor, there cannot be any electrochemical potential difference between the materials in contact; i.e., the Fermi levels must coincide between the metal and semiconductor. The nature of the electric field at the ZrO_2/Zr interface depends on the semiconductor type (donor/acceptor densities) and markedly influences oxygen transport through the oxide/metal interface.

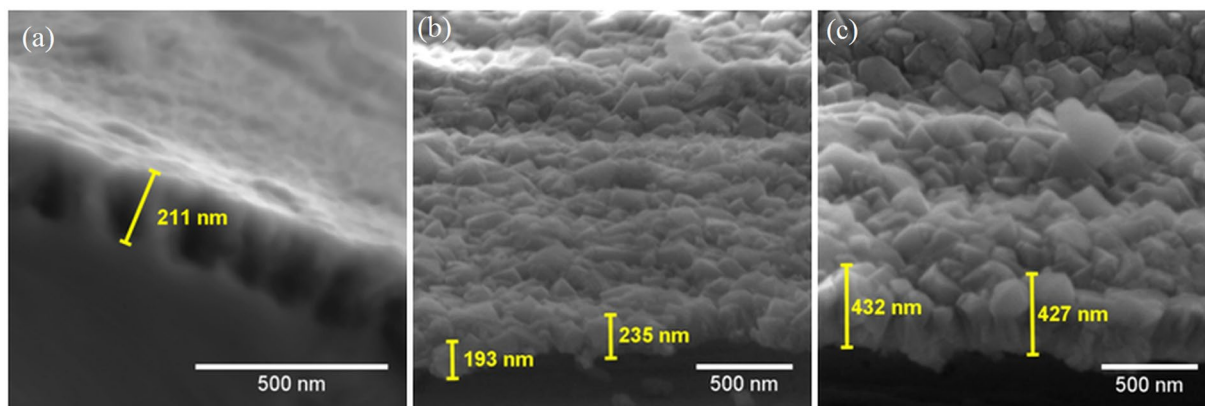


Figure 5. Secondary electron micrographs of NCD layer. (a) Thickness of 300 nm before 30 days of exposure to 360 °C hot water. (b) Thickness of 300 nm after 30 days of exposure to 360 °C hot water. (c) Thickness of 500 nm after 15 days of exposure to 360 °C hot water. No important change in the NCD layer thickness was detected, thus confirming the high durability of the layer.

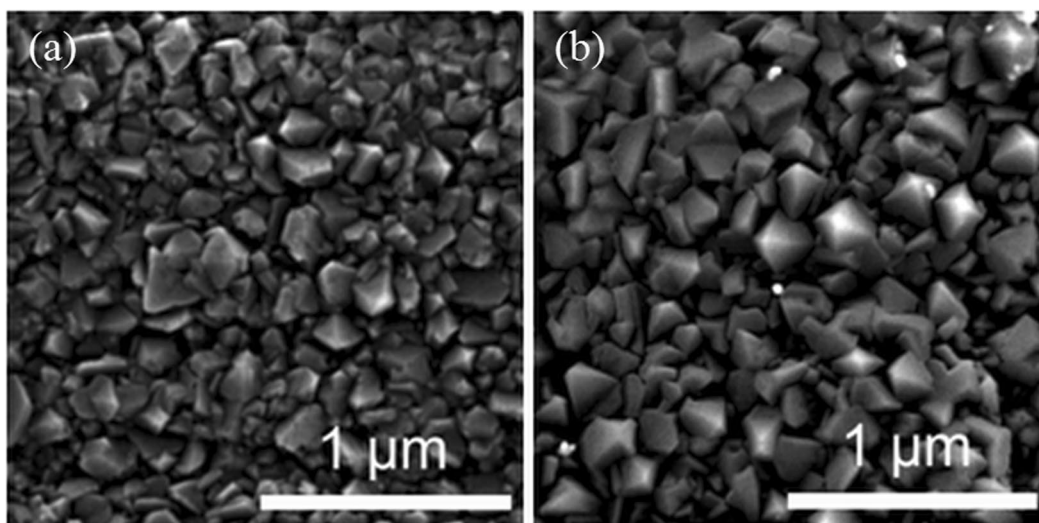


Figure 6. Secondary electron micrographs of the initial surface of a Zr alloy sample covered with 300 nm thick NCD (left) and the surface after 30 days of exposure to 360 °C hot water (right). No microstructural changes were observed in the hot-water-processed NCD film.

The impedance spectra of samples exposed to hot steam (4 days at 400 °C) (Fig. S4) showed a predominant capacitance contribution from the zirconium oxide corrosion layer over a very broad frequency range, from 10^6 Hz to 10^0 Hz. A slightly higher extent of impedance dispersion was found (both the phase angle and the slope of $\log |Z|$ vs. $\log f$ were lower) for the zirconium oxide formed on the NCD-coated samples. The impedance spectra were fitted by using an equivalent circuit model (see Methods). The dashed lines denote the linear slope regions used to calculate the densities of defects (additional donors/acceptors). As expected, the surface layers of hot-steam-processed ZIRLO both with and without NCD protective coatings exhibited semiconductive behavior.

The observed impedance dispersion in the high-frequency range showed no signs of the characteristic response of the NCD coating. The impedance response was dominated by the composite and relatively uniform effect of the carbon-enriched oxide (as a result of the diffusion of carbon into the oxide, as found in the SIMS analysis) and by remnants of the NCD coating. This finding indicated a possible change in the effective dielectric constant from a value of 23 (ZrO_2) to values between 23 and 6–9 (values typical of diamond layers) (Table S5).

In Fig. 8, Mott-Schottky plots of uncoated and NCD-coated ZIRLO samples after 4 days of exposure to 400 °C steam are presented. Only positive slopes of the Mott-Schottky plots were recorded in the case of uncoated ZIRLO samples. Therefore, the oxide films on uncoated and hot-steam-treated ZIRLO were found to exhibit solely n-type semiconductive behavior. This result was consistent with observations of pure zirconium²² and of Zr-Nb²³ and Zr-Sn alloys^{10–14, 24}. The results of the doping density analysis are presented in Table 2, where N_A and N_D denote the acceptor and donor densities, respectively. A high donor density (characteristic of an n-type semiconductor) was found for the uncoated ZIRLO both before and after hot steam exposure, whereas the NCD-coated ZIRLO

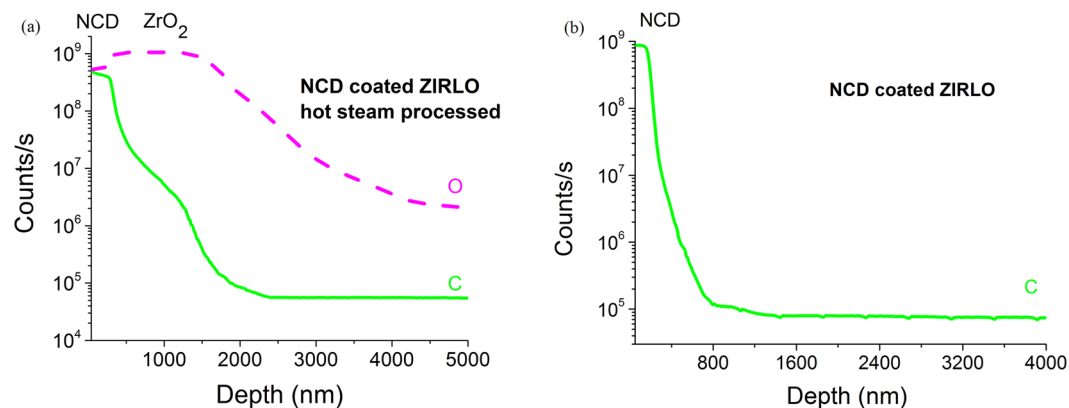


Figure 7. SIMS data showing that after 4 days of hot steam exposure at 400 °C, the ZrO₂ layer in 300 nm NCD-coated ZIRLO contained C to a depth bigger than 1.5 μm (a), whereas in non-exposed NCD-coated ZIRLO, the majority of the carbon was contained only within the thin (0.4 μm) NCD layer (b). The depth profiles of C and O are in units of counts/s and labelled in the graphs.

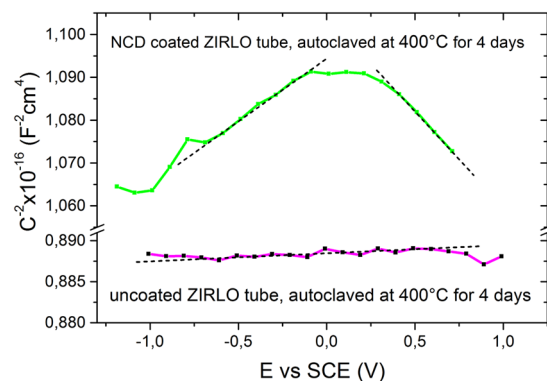


Figure 8. Mott-Schottky plots for NCD-coated and uncoated ZIRLO alloy samples after 4 days in 400 °C steam. The dashed lines denote the linear slope regions used to calculate the densities of defects (additional donors/acceptors). Both the zirconium oxide and the NCD layer clearly exhibited semiconductive behavior.

Sample	N _A [cm ⁻³]	N _D [cm ⁻³]
ZIRLO	—	4 × 10 ²⁰
ZIRLO, 4 days at 400 °C	—	2.3 × 10 ¹⁸
ZIRLO with 300 nm NCD, 4 days at 400 °C	4.4 × 10 ¹⁶	2–3 × 10 ¹⁶

Table 2. Acceptor and donor densities obtained from the Mott-Schottky plots for uncoated ZIRLO before and after hot steam exposure and for NCD-coated ZIRLO samples after hot steam exposure. The uncoated ZIRLO exhibited n-type semiconductive behavior, whereas the NCD-protected ZIRLO after hot steam exposure exhibited mixed p- and n-type semiconductive behavior.

samples after hot steam exposure showed both p-type (acceptor-containing) and n-type semiconductive behavior (Table 2).

The work function values obtained with the NanoESCA system support the results of the capacitance measurements. Typical Ultraviolet Photoemission Spectroscopy (UPS) spectra used for work function determination are presented in Fig. S5. Compared with standard ZrO₂^{28–30}, uncoated ZIRLO samples exposed to hot steam for 4 days at 400 °C were found to have a relatively low ZrO₂ work function of 2.0 eV, thus indicating an elevated position of the Fermi level. The Fermi level moves up in the presence of donors, and a high level of donors was indeed detected (Table 2). By contrast, for NCD-coated ZIRLO samples exposed to the same conditions, we observed a higher value of the surface ZrO₂ work function, 4.0 eV (Fig. S5). This result suggested the presence of acceptors, thereby implying p-type semiconductivity, i.e., a position of the Fermi level that is closer to the valence band. The results presented in Table 2 are well consistent with such an interpretation.

Discussion

In this work, a new anticorrosion strategy for Zr nuclear fuel cladding tubes and plates was presented and explained. Protective NCD layers were deposited on the surfaces of ZIRLO nuclear fuel cladding samples and ZIRLO plates by using an MW-LA-PECVD apparatus. A wide range of tests and analyses demonstrated the ability of such NCD layers to protect ZIRLO against corrosion in water-cooled nuclear reactor environments.

These NCD layers were shown to be stable and to exhibit strong adhesion to ZIRLO surfaces. Because of NCD's known high Young's modulus²⁷, NCD protective layers were able to withstand volume expansion during heating without any fundamental impairment of their integrity (as shown via SEM imaging and Raman spectroscopy).

After long-term processing (for up to 195 days) in 360 °C hot water (in accordance with ASTM standard procedures)²¹, a larger relative weight gain was found for ZIRLO samples with unprotected surfaces than for NCD-coated samples. The relative weight gain of the NCD-coated ZIRLO samples was decreased by 35–55%. This decrease was attributed to the restricted oxidation and hydrogen uptake of the NCD-protected samples¹². NCD layers were also found to protect ZIRLO surfaces against H uptake: the average hydrogen concentration was markedly greater for uncoated samples. For high-temperature hot steam processing (1100 °C, 1200 °C), the uptake of hydrogen into the unprotected material was an order of magnitude higher than that indicated by the hydrogen concentrations in the NCD-protected samples.

We also confirmed that, after hot steam processing, the surface ZrO₂ layers of NCD-coated ZIRLO tubes were thinner than the corresponding ZrO₂ layers in unprotected ZIRLO tubes subjected to the same treatment (as demonstrated via optical microscopy, SIMS, SEM, and capacitance measurements).

Thicker (700 nm and 500 nm) NCD layers provided stronger protection of ZIRLO plates and tubes against oxidation than thinner (300 nm) NCD layers. The best protective effect was achieved by 700 nm NCD coatings on ZIRLO plates: the surface oxidation of these samples after hot water processing (360 °C, from 20 days to 40 days) was decreased by more than 50%. The higher protective efficacy achieved by the NCD coatings for ZIRLO plates compared with ZIRLO tubes was attributed to the inner surfaces of the tubes not being fully covered with NCD, whereas in the case of ZIRLO plates mounted vertically in the deposition chamber, all surfaces were covered with homogeneous NCD layers¹⁵. Notably, the MW-LA-PECVD apparatus, if scaled up as necessary, would be capable of homogeneously coating the full lengths of nuclear rods.

Both the native oxide film on ZIRLO and the oxide formed after 4 days of exposure to 400 °C hot steam exhibited n-type semiconductivity in an approximately 2 μm thick layer. In contrast to unprotected ZIRLO tubes, NCD-protected ZIRLO samples exposed to the same conditions (400 °C hot steam) formed an oxide layer that was thinner by 0.4 μm and showed mixed p- and n-type semiconductivity (capacitance measurements and nano-ESCA). This effect was correlated with the penetration of carbon into the ZrO₂ layer (XPS and SIMS).

We tested the ability of NCD layers to protect the Zr alloy against corrosion over a wide range of environmental parameters: temperatures from 360 °C (hot water, ASTM standard procedures)²¹ to 1200 °C (hot steam) and times ranging from 20 minutes in 1200 °C hot steam up to 195 days in 360 °C hot water. The tested thicknesses of the NCD layers were 300, 500 and 700 nm, and the NCD layers were applied to both ZIRLO plates and ZIRLO tubes. However, the main contribution of this work lies in providing a detailed explanation of the anticorrosive mechanism of NCD. The surface-protective materials that have previously been tested for use on Zr alloys, have been more or less unsuccessful^{5–7}, and typically homogeneous. By contrast, the anticorrosive effect of NCD, which is a heterogeneous material (containing both graphite and diamond), was found to be very significant, and, notably, an NCD layer protects ZIRLO against corrosion in a unique way. In this work, we demonstrated and explained the complex mechanism of the surface protection provided by an NCD layer on ZIRLO against H and O uptake. This protection occurs at three basic levels: 1. the NCD protects the ZIRLO surface from directly interacting with water molecules; 2. carbon atoms penetrate into the ZIRLO from the NCD, thus creating carbides and becoming incorporated into ZrO₂, thereby making conditions less favorable for subsequent O and H uptake; and 3. the carbon from the NCD changes the electrical properties of the ZrO₂ and creates less favorable conditions for Zr oxidation at the ZrO₂/Zr interface. These aspects of the protective mechanism are discussed in greater detail below:

Aspect 1, the stable NCD layer prevents the Zr alloy from directly interacting with water. The composition of NCD is not homogeneous - the NCD layers at the ZIRLO/NCD interfaces contained relatively large amounts of sp²-hybridized C, whereas the surfaces of all NCD layers were formed almost exclusively of hard and inert diamond¹⁷. The NCD layer at ZIRLO/NCD interfaces, where the ratio of grain boundaries to grains is higher, consists of a higher level of sp²-hybridized C. Mainly from sp²-hybridized C at the ZIRLO/NCD interface C penetrates into the underlying layers. On the contrary, the surface of NCD, where crystalline grains are fully formed, consists of practically only hard and inert diamond¹⁷ and therefore forms a strong barrier between the water and ZIRLO. Because of its composition and the conditions of its deposition, such an NCD layer is able to withstand volume changes due to thermal expansion and therefore does not suffer from delamination^{15–17}.

Aspect 2, during NCD growth and hot steam processing, carbon from the NCD layer penetrates into the underlying material, thus creating carbides, mainly in the zirconium oxide layer and also at the ZrO₂/Zr interface (Fig. S6). In this manner, carbon changes the original material such that conditions become less favorable for the penetration of oxygen and hydrogen through the ZIRLO surface layer.

Aspect 3, the penetrating carbon causes the n-type semiconductivity of the original ZrO₂ layer to change to a mixed n- and p-type semiconductivity, which also affects the Zr oxidation conditions. Under the typical conditions of hot steam nuclear reactors, the Zr oxide film grows with a large number of defects that cause the ZrO₂ to exhibit n-type semiconductivity^{11–14,22}. In the contact region between the metal and the semiconductor, a potential difference arises because of the redistribution of charges (Figs S6 and S7). The electric field thus established can markedly affect the transport of charge carriers through the ZrO₂/metal interface. The presence of impurity atoms in the oxide region affects not only the type of conductivity - electron or hole - but also the difference in chemical potentials and the electric field distribution near the contact region with the oxide film^{11,12}.

For unprotected ZIRLO with an n-type semiconductive surface layer, O anions originating from the dissociation of water ($2\text{O}^{2-} + 4\text{H}^+ \rightarrow 2\text{H}_2\text{O}$) pass redundant electron(s) through the n-type semiconductive ZrO_2/Zr alloy interface, thus enabling these oxygens to directly interact with/oxidize the zirconium (Figs S6 and S7)^{11–13}. This process occurs alongside a process in which Zr atoms lose electrons at the ZrO_2/Zr interface and subsequently interact with O^{2-} anions, thus also producing ZrO_2 ^{10,13}. The electric field established at the semiconductor/metal interface (Fig. S7) depends on the type of semiconductivity (n or p); that is, the type of semiconductivity defines the nature of the possible charge transport through the ZrO_2/Zr interface and results in different conditions for Zr oxidation^{10,11,24}. The mixed n- and p-type semiconductivity of the ZrO_2 that forms in NCD-protected ZIRLO changes the charge distribution, thereby decreasing the electric field in the ZrO_2 layer and making conditions less favorable for Zr oxidation.

Our results have substantial relevance for various applications. At high temperatures (1100 °C), the investigated NCD layers may fully serve as passive elements for nuclear safety. Also very important is these layers' effective protection of Zr alloys against oxidation and hydration under standard operating conditions (360 °C). The corrosion of Zr alloys degrades their ability to satisfy criteria for fuel cladding operability, thus leading to the need to replace rods containing nuclear fuel, owing to Zr alloy surface degradation. Better protection of fuel rod surfaces against corrosion would allow for the prolongation of nuclear fuel usage. We found that the oxidation of NCD-coated ZIRLO surfaces after more than 100 days in 360 °C hot water was significantly decreased (35–55%) compared with that of unprotected ZIRLO processed under the same conditions. The NCD-protected ZIRLO alloys also exhibited lower hydrogen concentrations than the unprotected samples under all investigated conditions; in particular, for high-temperature steam exposure (at 1100 °C for 1 hour, i.e., accident conditions), the NCD-protected ZIRLO samples showed much lower hydrogen uptake than unprotected ZIRLO samples.

Radiation tolerance of NCD layers grown in the MW-LA-PECVD apparatus as important parameter for application in nuclear reactors was simulated and published in our previous work¹⁶. We have studied¹⁶ resistivity of NCD layer as a set of nanodiamond grains and sp^2 hybridized C against radiation damage. The behavior of NCD coated Zr alloy in a neutron flux environment was simulated by Fe ion beam irradiation of the complex material (Fe^{2+} , 3 MeV, room temperature, fluency of $1.95 \times 10^{16} \text{ cm}^{-2}$). Heavy ions bombardments have been widely used to simulate neutron damage of various materials³⁶ and in our specific case no significant changes in structural integrity of NCD layer were found¹⁶. It should be noted that radiation damage strongly depends on radiation dose and also on specific material setting (i.e. monocrystalline or polycrystalline diamond, sp^3 C phase)^{16,19,20}.

It should be emphasized that NCD layer prevents the Zr alloy from directly interacting with water environment. Beside that, carbon from NCD layer penetrates into the underlying material and changes its properties, such that uptake of oxygen and hydrogen into Zr material is significantly decreased. Protective NCD layers can prolong the lifetime of nuclear cladding and, consequently, enhance nuclear fuel burnup. The combination of NCD coatings with other materials may be a very promising step toward achieving the effective protection of Zr alloys against corrosion under exposure to hot steam or hot water. According to tests conducted at the Halden Material Testing Reactor (Norway), NCD-coated ZIRLO claddings with properly grown NCD films are a possible candidate for Accident Tolerant Fuel in commercially operated reactors.

Experimental methods

Growth of NCD. ZIRLO fuel cladding tubes (25 mm in length and 10 mm in diameter) and ZIRLO plates (20 mm × 20 mm × 0.1 mm) were immersed (covering the internal and external surfaces of the tubes and both sides of the plates) in a colloidal solution of diamond nanoparticles (NanoAmando). The diamond nanoparticles acted as seeds and therefore as nucleation sites for NCD layer growth. Each ZIRLO sample was then coated with a homogeneous NCD layer grown using a MW-LA-PECVD apparatus (Fig. S1) under the following conditions: a gas mixture of $\text{H}_2 + \text{CH}_4 + \text{CO}_2$, a process pressure of <1 mbar, a microwave power of $2 \times 3 \text{ kW}$, and a temperature of approximately 600 °C. Because of the diffuse nature of plasma at low process pressures, the growth of NCD layers was achieved over the entire outer circumference of ZIRLO tubes mounted horizontally in the deposition chamber. However, the inner surfaces were only partially coated. This lack of internal coverage is further discussed above with respect to the interpretation of the results. In the case of ZIRLO plates mounted vertically in the deposition chamber, both surfaces were covered with NCD layers. NCD layers of 200–300 nm (labeled as 300 nm), 400–500 nm (labeled as 500 nm) and 600–700 nm (labeled as 700 nm) were produced. Optical microscopy, Raman spectroscopy and SEM were used to confirm the NCD layer coverage of the ZIRLO. Notably, the MW-LA-PECVD apparatus could be scaled up such that it would be capable of coating the full lengths of nuclear rods.

It should be emphasized that the coverage of the inner portions of the tubes can be avoided by sealing both tube ends before the NCD layer deposition. The NCD layer then covers only the outer surface of the tube. NCD coated tube samples for Halden Material Testing Reactor (Norway) were made in this way//coated just on the outer surface.

Sample exposure to nuclear reactor environments under normal and accident conditions. To simulate the long-term protective capabilities of NCD layers under normal conditions in a nuclear reactor, NCD-coated and reference uncoated ZIRLO samples were subjected to a series of high-temperature autoclave water tests. In accordance with ASTM standard procedures²¹, the samples were exposed for 6, 15, 20, 30, 40, 90, 120, 150, 170 and 195 days in hot water (360 °C) at a pressure of 16 MPa, close to the conditions found in the primary circuit of a PWR, at the Westinghouse facilities in Pittsburgh, USA. No additional chemicals were used in the autoclave water.

To simulate the protective capabilities of NCD layers against hot steam under normal and accident conditions in a nuclear reactor, NCD-coated and reference uncoated ZIRLO samples were subjected to a series of high-temperature steam tests. The samples (tubes or plates) were placed in a silica glass tube reactor, which was placed inside a furnace. The samples were heated to the required temperature and for the required duration (400 °C/4 days at 15 MPa and less than 10 ppb of oxygen, 900 °C/1 h, 1100 °C/1 h and 1200 °C/20 min) in an inert

argon atmosphere at atmospheric pressure. All steam exposures were performed isothermally. After hot steam processing, the steam/water flow was switched off after the required time, and the sample was slowly cooled down under an argon atmosphere.

XPS analysis. XPS measurements were performed using an ESCA Probe P (Omicron Nanotechnology) with a primary X-ray source of monochromatized radiation from an Al anode (1486.7 eV). The constant analyzer energy (CAE) mode was used, at pass energies of 50 eV for overview spectra and 30 or 20 eV for detailed spectra. Charge compensation was achieved by using an electron gun at very low electron energies (between 1 eV and 2.5 eV) to protect the sample. Measurements of copper and calibration constants derived from these spectra were used for intensity calibration. The full widths at half maximum of the components used for the analysis of line details were based on experimental experience with the spectra of carbon and silver and were consistent with the capabilities of the instruments used. Spectral evaluation was conducted using CASA XPS software; the area of the peaks after calibration and a database of relative sensitivity factors were used for the determination of elemental concentrations. Chemical species were identified using XPS databanks. An ion gun (ISE5) connected to the preparation chamber was operated with argon ions, typically at an energy of 5 keV.

Mechanical and tribological measurements. The analysis of the mechanical and tribological properties of the samples was performed using a fully calibrated NanoTest instrument equipped with diamond indenters at room temperature, operating in load-controlled mode. A three-sided Berkovich indenter was used in nanoindentation experiments to evaluate the indentation hardness, elastic modulus and creep. Nanoindentation was performed at a peak load of 1 mN, with both the loading and unloading rates set to 0.5 mN/s. This relatively low load ensured, in the case of the NCD films, a maximum penetration depth of approximately 10% of the layer thickness to ensure that the calculated values of the mechanical properties could be regarded as layer dominated. Standard analysis procedures were used to calculate the indentation hardness and the decreased elastic modulus from at least 10 independent measurements for each sample³³. Creep experiments with a dwell period of 300 s at a load of 200 mN were performed to explore the composite response of the film/ZIRLO system to constant loading. To quantify the deformation tendencies of the NCD layers and the ZIRLO samples before and after hot water/steam exposure under a constant indentation load, the parameter *P* introduced by Goodall and Clyne was used³¹. This parameter is defined as the product of the slope of the steady-state part of the creep curve, in our case 150–300 s, and the increase in depth at the end of the constant-load period. For a higher value of *P*, higher deformation is expected to occur during constant-load creep³².

The scratch resistance of the uncoated and NCD-coated ZIRLO samples was tested using a sphero-conical Rockwell indenter with a nominal radius of 10 μm. Progressive scratch tests up to a maximum load of 500 mN were performed in a 3-step procedure consisting of initial topography measurements followed by scratch and final topography measurements. The topography measurements were performed over the entire scratch length at a low load of 0.02 mN to avoid wear. During the scratch procedure, the applied topographic load was initially constant over the first 50 μm and then ramped to the maximum load at a constant loading rate of 13.8 mN/s. All scans were performed at a scan speed of 10 μm/s over a total scan length of 450 μm. Evaluation of the scratch tests was performed on the basis of the indenter on-load and depth records and analysis of the residual scratch tracks using a confocal laser scanning microscope (Olympus LEXT 3000).

Thermogravimetry, mass spectrometry and optical microscopy of the metallographic cross sections of samples. Thermogravimetry measurements were performed at elevated temperatures between 900 and 1100 °C. The samples were placed on an alumina holder in a NETZSCH thermobalance (model STA 409). Argon was used as an inert cover gas. Steam exposures were performed isothermally, without any changes in the steam or cover gas flow rates. All high-temperature oxidations were performed under an argon flow rate of 3 l/h and a steam flow rate of 3 g/h. The overall weight gain (w_g), which is a commonly used quantity to describe the corrosion of a zirconium alloy in a water-steam environment, was determined by measuring the sample's weight before and after oxidation. This weight was normalized with respect to the total exposed surface area of the sample to compensate for different sample sizes. The units used (mg/dm²) are commonly used in engineering practice and calculations. The sample surface area was calculated from the sample dimensions (length and inner and outer diameters) measured before steam exposure. The equivalent cladding reacted (ECR) (in %) for two-sided oxidation was calculated using the following formula¹⁴:

$$ECR = \frac{87.8 w_g}{s} \quad (1)$$

where *s* is the thickness of the sample and w_g is the weight gain over the entire surface area.

Off-gas analysis was performed with a Balzers GAM 300 quadrupole mass spectrometer. The hydrogen flow rate was calculated using the measured concentrations of argon and hydrogen, and the argon flow rate was measured with a volumetric flowmeter. Overall hydrogen production was calculated as the integral of the hydrogen flow rate. Hydrogen production was normalized to the sample surface area to compensate for different sample sizes.

Cross sections were acquired from the central parts of samples processed under 1000 °C hot steam by using an optical microscope. The samples were hot pressed into electrically conductive transparent resin (Bakelite), which is suitable for sample analyses via optical microscopy. The samples were ground using an automatic polishing device with a polishing head with individual contact pressure. The contact pressures were chosen according to the temperature at which each sample was exposed. Polishing was performed by using the same polishing device with an individual contact pressure of 35 N for all types of exposures. A classic canvas and a colloidal mixture of SiC (Colloidal Silica Polishing Suspension) from MasterMet were used for polishing. The samples were observed using an optical microscope after each polish.

SEM. The surface morphologies of the NCD layers were analyzed by using a Tescan FERA 3 scanning electron microscope. To minimize the interaction volume during imaging, the accelerating voltage in high-resolution mode was kept in the range of 2–5 kV. EDS composition analysis was performed using an EDAX Octane Super 60 mm² detector with an acceleration voltage of 5 kV for elemental analysis. The structures were opened using a Xe-FIB.

Raman spectroscopy. To determine the NCD layer composition (sp² and sp³-hybridized carbon), the deposited layers were characterized with Raman spectroscopy performed at room temperature using a Renishaw InVia Raman Microscope under the following conditions: a laser excitation wavelength of 488 nm (25 mW), ×50 Olympus objective, 65 μm slits, spot focus, and a grating of 2400 lines/mm. Spectra were acquired at various points across the samples to probe the homogeneity of the deposited NCD layers.

SIMS. SIMS measurements were performed in depth profiling mode with a Cameca IMS 7 f magnetic sector instrument. A Cs⁺ primary ion beam with an impact energy of 15 keV, a current of 20 nA and an impact angle of ~23° from the surface normal was raster scanned over an area of 100 μm × 100 μm, thus resulting in a sputter rate of ~1.4 nm/s. The depth scale of the SIMS craters was calibrated using a stylus profilometer. The instrument was operated at a low mass resolving power of M/ΔM ~400. Standard precautions were taken to limit the distortions of the SIMS depth profile data caused by crater edge effects. Secondary ions were detected in single-ion counting mode using an electron multiplier or, for high count rates, using a Faraday cup and an electrometer amplifier. An electron beam in self-compensation mode was used for charge compensation during the analysis. The vacuum pressure in the analysis chamber during the measurement was approximately 1 × 10⁻⁹ mbar. Negatively charged secondary ions were monitored.

Hydrogen concentration measurements. The amount of hydrogen dissolved in the ZIRLO after steam exposure (at either a low temperature simulating operating conditions or a high temperature simulating accident conditions) was determined with a G8 GALILEO analyzer. This analyzer operates on the basis of the inert gas fusion principle, which requires the fusion of the sample material in a graphite crucible at high temperatures. The concentration of the outgoing hydrogen is subsequently measured with a mass spectrometer. No correction for an oxide layer was applied; consequently, for heavily oxidized samples from thermogravimetric experiments, the measured value of the hydrogen concentration does not exactly reflect the actual concentration in the sample.

Capacitance measurements. Impedance spectra and the dependence of capacitance on potential (Mott-Schottky plots) were measured in a 3-electrode cell at room temperature in 0.5 M K₂SO₄ and a borate buffer (pH = 9.2), respectively. A saturated calomel electrode was used as the reference electrode, and the NCD-coated and uncoated ZIRLO tubes and plates before and after oxidation for 4 days in 400 °C steam were used as the working electrodes. A platinum mesh coaxial electrode served as the counter electrode. Included in the measurement setup was a Reference 600 potentiostat (Gamry). Impedance data were measured after the stabilization of the open-circuit potential for 1 h. The impedance spectra were measured in the frequency range from 10⁶ Hz to 10⁻² or 10⁻³ Hz, using a 5 mV perturbation signal. Polarization was applied in successive steps of 100 mV in the anodic direction over the potential range of -1 V to +1 V. The amplitude of the perturbation signal was 5 mV, and the frequency was 1 kHz. Under the assumption of a serial connection between the solution resistance and electrode capacitance at high frequencies, the capacitance was calculated from the relation:

$$C = (-Z_i 2 \pi f)^{-1} \quad (2)$$

where Z_i is the imaginary part of the impedance, and f is the frequency. The impedance spectra were fitted by using the equivalent circuit model depicted in Fig. S8. An RC* parallel combination was used to express the response of a surface layer (NCD and/or oxide) and an Rf - Cdl parallel combination in series to RC*, describing faradaic resistance and double-layer capacitance effects.

In the RC* term, R represents the layer resistance, and C* is the complex capacitance term introduced by Jonscher³⁷ to describe the impedance dispersion induced by a non-ideal dielectric response. The impedance of a Jonscher element can be expressed as follows:

$$C^* = C_{\text{inf}} + \frac{1}{Q(j\omega)^n} \quad (3)$$

where C* is a complex capacitance; Q is a constant related to the dielectric dispersion; the exponent n is the dispersion index, which represents the extent of capacitance dispersion (for an ideal capacitance, n = 1); j is the imaginary unit; and ω is the angular frequency. C_{inf} is defined as the capacitance value at infinite frequency. C_{inf} is independent of frequency and can be directly related to the dielectric layer thickness by the following expression for a flat capacitor:

$$\delta = \frac{A \varepsilon_r \varepsilon_0}{C_{\text{inf}}} \quad (4)$$

where ε₀ is the permittivity of vacuum (8.854 × 10⁻¹⁴ F/cm), ε_r is the relative permittivity of the layer, and A is the area. In a Mott-Schottky analysis, the impedance of the electrode-electrolyte interface is measured at a high frequency as a function of the imposed potential. The capacitance values are obtained from the imaginary part of the impedance:

$$C = -(\omega Z'')^{-1} \quad (5)$$

The interfacial capacitance C measured at high frequency can be described as a series combination of a capacitive contribution from the surface layers, C_{surf} , which includes the oxide- and NCD-layer responses; a contribution from the space charge region developed in the defective barrier layers in the NCD layer and/or the oxide layer, C_{sc}^{22} ; and a contribution from the Helmholtz layer at the film-electrolyte interface, C_H :

$$\frac{1}{C} = \frac{1}{C_{surf}} + \frac{1}{C_{SC}} + \frac{1}{C_H} \quad (6)$$

In the case of high-frequency measurements, the Helmholtz capacitance term can be neglected ($C_H \gg C_{ox}$, C_{sc}), and the dielectric response term is independent of the potential. The relationship between the measured capacitance and the potential can be expressed using Mott-Schottky theory for the case of n-type conductivity as follows:

$$\frac{1}{C^2} = \frac{1}{C_{surf}^2} + \frac{2}{\epsilon_r \epsilon_0 q N_D} \left(V - V_{fb} - \frac{kT}{q} \right) \quad (7)$$

Here, ϵ_r is the dielectric constant of the surface film (in this study $\epsilon_r = 23$ was used for an oxide film and $\epsilon_r = 10^{-17}$ was used for an NCD-coated sample after a 400 °C hot steam oxidation test), ϵ_0 is the permittivity of vacuum, N_D is the donor density (cm^{-3}), q is the elementary charge, V is the applied potential, V_{fb} is the flat-band potential, k is the Boltzmann constant, and T is the absolute temperature.

The bulk surface film capacitance term is independent of voltage and can cause a shift in the flat-band potential value (the intercept of the linear part of the Mott-Schottky plot when extrapolated to zero capacitance). It does not influence the slope of the linear part of the Mott-Schottky plot, from which the donor density is determined²³.

XPS, UPS and work function analysis with a NanoESCA system. Uncoated and NCD-coated ZIRLO samples after hot steam tests were subjected to analyses of their work functions and surface potentials. For this purpose, a NanoESCA (Oxford Instruments Omicron Nanoscience) photoemission spectrometer based on a Photoelectron Emission Microscopy (PEEM) column and a double hemispherical imaging energy filter was used. This apparatus enables XPS, UPS and PEEM measurements and analyses using various excitation sources: monochromatic Al $K\alpha_{1,2}$ X-rays, an He discharge lamp (FOCUS HIS 13) and an Hg lamp. The valence band spectra for the determination of the Fermi level and the valence band maximum were acquired via XPS. Work function mapping was performed via PEEM using an Hg lamp. Furthermore, the work function values were also probed by obtaining UPS spectra. The work function of each sample was extracted from the low-kinetic-energy cut-off of the UPS spectrum. The samples were briefly Ar sputtered to remove surface contamination.

References

- Hirano, M. *et al.* Insights from review and analysis of the Fukushima Dai-ichi accident. *J. Nucl. Sci. Technol.* **49**, 1–17 (2012).
- Was, G. S. *Fundamentals Of Radiation Materials Science: Metals And Alloys*. (Springer, 2007).
- Högberg, L. Root causes and impacts of severe accidents at large nuclear power plants. *Ambio* **42**, 267–284 (2013).
- Puls, M. P. Review of the thermodynamic basis for models of delayed hydride cracking rate in zirconium alloys. *J. Nucl. Mater.* **393**, 350–367 (2009).
- Jin, D. *et al.* A study of the zirconium alloy protection by Cr_3C_2 -NiCr coating for nuclear reactor application. *Surf. Coat. Technol.* **287**, 55–60 (2016).
- Zhong, W. *et al.* Performance of iron-chromium-aluminum alloy surface coatings on Zircaloy 2 under high-temperature steam and normal BWR operating conditions. *J. Nucl. Mater.* **470**, 327–338 (2016).
- Steinbrück, M., Vér, N. & Große, M. Oxidation of advanced zirconium cladding alloys in steam at temperatures in the range of 600–1200 °C. *Oxid. Met.* **76**, 215–232 (2011).
- Beaumont, J. S., Mellor, M. P., Villa, M. & Joyce, M. J. High-intensity power-resolved radiation imaging of an operational nuclear reactor. *Nat. Commun.* **6**, 8592, doi:10.1038/ncomms9592 (2015).
- Banerjee, D. *et al.* Metal-organic framework with optimally selective xenon adsorption and separation. *Nat. Commun.* **7**, 11831, doi:10.1038/ncomms11831 (2016).
- Hutchinson, B. & Lehtinen, B. A theory of the resistance of Zircaloy to uniform corrosion. *J. Nucl. Mater.* **217**, 243–249 (1994).
- Rudling, P. & Wikmark, G. A unified model of Zircaloy BWR corrosion and hydriding. *J. Nucl. Mater.* **265**, 44–59 (1999).
- Motta, A. T., Couet, A. & Comstock, R. J. Corrosion of zirconium alloys used for nuclear fuel cladding. *Annu. Rev. Mater. Res.* **45**, 311–343 (2015).
- Likhanskii, V. V., Evdokimov, I. A. Review of theoretical conceptions on regimes of oxidation and hydrogen pickup in Zr-alloys. *7. International conference on WWER fuel performance, modelling and experimental support; Albena (Bulgaria); 17–21 Sep 2007* http://www.iaea.org/inis/collection/NCLCollectionStore/_Public/39/079/39079731.pdf (2008).
- Billone, M., Yan, Y., Burtseva, T. & Daum, R. Cladding Embrittlement During Postulated Loss-of-Coolant Accidents (NUREG/CR-6967). <https://www.nrc.gov/docs/ML0821/ML082130389.pdf> (2008).
- Fendrych, F. *et al.* Growth and characterization of nanodiamond layers prepared using the plasma-enhanced linear antennas microwave CVD system. *J. Phys. D: Appl. Phys.* **43**, 374018–374022 (2010).
- Kratochvílová, I. *et al.* Nanosized polycrystalline diamond cladding for surface protection of zirconium nuclear fuel tubes. *J. Mater. Process. Technol.* **214**, 2600–2605 (2014).
- Ashcheulov, P. *et al.* Thin nanocrystalline diamond films protecting zirconium alloys surfaces: from technology to layer analysis and application in nuclear facilities. *Appl. Surf. Sci.* **359**, 621–628 (2015).
- Škoda, R., Škarohlíd, J., Kratochvílová, I., Taylor, A., Fendrych, F. Czech Technical University in Prague Faculty of Mechanical Engineering, Institute of Physics AS CR. Layer protecting the surface of zirconium alloys used in nuclear reactors. Czech patent 305059 (2015).
- Karkin, A. E. *et al.* Neutron irradiation effects in chemical-vapor-deposited diamond. *Physical Review B* **78**, 033204–0033207 (2008).
- Vance, E. R. X-ray study of neutron irradiated diamonds. *J. Phys. C: Solid St. Phys.* **4**, 257–262 (1971).

21. Standard test method for corrosion testing of products of zirconium, hafnium, and their alloys in water at 680 °f (360 °C) or in steam at 750 °f (400 °C), ASTM G2/G2M-06 e1, <https://www.astm.org/Standards/G2.htm> (201) (2011).
22. Chen, Y., Urquidi-Macdonald, M. & Macdonald, D. D. The electrochemistry of zirconium in aqueous solutions at elevated temperatures and pressures. *J. Nucl. Mater.* **348**, 133–147 (2006).
23. Krausová, A. *et al.* *In-situ* electrochemical study of Zr1Nb alloy corrosion in high temperature Li⁺ containing water. *J. Nucl. Mater.* **467**, 302–310 (2015).
24. Ferreira, N. G., Silva, L. L. G., Corat, E. J., Trava-Airoldi, V. J. & Iha, K. Electrochemical characterization on semiconductors p-type CVD diamond electrodes. *Braz. J. Phys.* **29**, 760–763 (1999).
25. Benninghoven, A., Rüdener, F. G. & Werner, H. W. *Secondary Ion Mass Spectrometry: Basic Concepts, Instrumental Aspects, Applications and Trends*. (John Wiley, 1987).
26. Meisterjahn, P., Hoppe, H. W. & Schultze, J. W. Electrochemical and XPS measurements on thin oxide films on zirconium. *J. Electroanal. Chem.* **217**, 159–185 (1987).
27. Williams, O. A. *et al.* High young's modulus in ultra thin nanocrystalline diamond. *Chem. Phys. Lett.* **495**, 84–89 (2010).
28. Chakraborty, S. *et al.* Leakage current characteristics and the energy band diagram of Al/ZrO₂/Si_{0.3}Ge_{0.7} hetero-MIS structures. *Semicond. Sci. Tech.* **21**, 467–472 (2006).
29. Sayan, S. *et al.* Valence and conduction band offsets of a ZrO₂/SiO_xN_y/n-Si CMOS gate stack: A combined photoemission and inverse photoemission study. *Phys Status Solidi B* **241**, 2246–2252 (2004).
30. Schlaf, R., Murata, H. & Kafafi, Z. H. Work function measurements on indium tin oxide films. *J. Electron Spectrosc.* **120**, 149–154 (2001).
31. Goodall, R. & Clyne, T. W. A critical appraisal of the extraction of creep parameters from nanoindentation data obtained at room temperature. *Acta Mater.* **54**, 5489–5499 (2006).
32. Čtvrtlík, R., Al-Haik, M. S. & Kulikovskiy, V. Mechanical properties of amorphous silicon carbonitride thin films at elevated temperatures. *J. Mater. Sci.* **50**, 1553–1564 (2015).
33. Oliver, W. C. An improved technique for determining hardness and elastic modulus using load and displacement sensing indentation experiments. *J. Mater. Res.* **7**, 1564–1583 (1992).
34. Stehlik, S. *et al.* High-yield fabrication and properties of 1.4 nm nanodiamonds with narrow size distribution. *Scientific Rep.* **6**, 38419, doi:10.1038/srep38419 (2016).
35. Ferrari, A. C. & Robertson, J. Resonant Raman spectroscopy of disordered, amorphous, and diamondlike carbon. *Phys. Rev. B* **64**, 754141–754413 (2001).
36. Gary, S. W. *Fundamentals Of Radiation Materials Science: Metals And Alloys* (Springer, 2007).
37. Jonscher, A. K. Physical basis of dielectric loss. *Nature* **253**, 717–719 (1975).

Acknowledgements

Special thanks to Patrik Foral and Michal Šimoník from Westinghouse Electric Czech Republic s.r.o. for their cooperation and to Ladislav Klimša and Jarmila Remiášová from the Institute of Physics AS CR. This work was supported in part by the MEYS CR FUNBIO projects CZ.2.16/3.1.00/21568, LO1409 and LM2015088 (laboratory maintenance), by the Czech Science Foundation (15-05095S and 16-03085S), by the SUSEN Project CZ.1.05/2.1.00/03.0108 (ERDF), by the Technology Agency of the Czech Republic (projects TA04020156, CANUT - TE01020455, and COST CA15107), and by Projects No. LO1305 and LQ1603 (Research for SUSEN) of the Ministry of Education, Youth and Sports of the Czech Republic. Petr Ashcheulov expresses gratitude for the financial support from the Czech Academy of Sciences, awarded as part of the PPLZ Program for postdoctoral researchers.

Author Contributions

J. Škarohlíd: thermogravimetry, mass spectrometry analysis. P. Ashcheulov: growth of nanocrystalline diamond layers, Raman spectroscopy. R. Škoda: writing of part of the manuscript text, thermogravimetry. A. Taylor: writing of part of the manuscript text and optimization and growth of diamond films. R. Čtvrtlík: mechanical and tribological measurements. J. Tomáščík: mechanical and tribological measurements. F. Fendrych: writing of part of the manuscript text, participation in CVD apparatus construction. J. Kopeček: SEM and EDS analysis. V. Cháb: NanoESCA measurements, data interpretation. S. Cichoň: NanoESCA measurements. P. Sajdl: XPS measurements. J. Macák: capacitance measurements. Peng Xu: handling of samples after hot water processing. J. M. Partezana: weight gains of samples after hot water processing. J. Lorinčík: SIMS measurements, data interpretation. J. Prehradná: handling of samples after hot water processing. M. Steinbrück: metallographic analysis of the samples. I. Kratochvílová: writing of the main manuscript text.

Additional Information

Supplementary information accompanies this paper at doi:10.1038/s41598-017-06923-4

Competing Interests: The authors declare that they have no competing interests.

Publisher's note: Springer Nature remains neutral with regard to jurisdictional claims in published maps and institutional affiliations.



Open Access This article is licensed under a Creative Commons Attribution 4.0 International License, which permits use, sharing, adaptation, distribution and reproduction in any medium or format, as long as you give appropriate credit to the original author(s) and the source, provide a link to the Creative Commons license, and indicate if changes were made. The images or other third party material in this article are included in the article's Creative Commons license, unless indicated otherwise in a credit line to the material. If material is not included in the article's Creative Commons license and your intended use is not permitted by statutory regulation or exceeds the permitted use, you will need to obtain permission directly from the copyright holder. To view a copy of this license, visit <http://creativecommons.org/licenses/by/4.0/>.

© The Author(s) 2017

List of abbreviations

ATF	Accident Tolerant Fuel
BWR	Boiling Water Reactor
DBA	Design Based Accident
DHC	Delayed Hydride Cracking
DNB	Departure from Nucleate Boiling
dpa	displacement per atom
ECCS	Emergency Core Cooling System
ECR	Equivalent Cladding Reacted
EDS	Energy Dispersive x-ray Spectroscopy
HPUF	Hydrogen Pick-Up Fraction
HTO	High Temperature Oxidation
HU	Hydrogen Uptake
IAM-AWP	Institut für Angewandte Materialien - Angewandte Werkstoffphysik
IASCC	Irradiation assisted stress corrosion cracking
IGF	Inert Gas Fusion
KIT	Karlsruhe Institute of Technology
LOCA	Loss of Coolant Accident
PCD	Polycrystalline Diamond
PCI	Pellet-Cladding Interaction
PCMI	Pellet-Cladding Mechanical Interaction
PEEM	PhotoElectron Emission Microscopy
PWR	Pressurized Water Reactor
RBMK	Reaktor Bolšoj Moščnosti Kanalnyj
RHRS	Residual Heat Removal System
RPV	Reactor Pressure Vessel
SEM	Scanning Electron Microscopy
SIMS	Secondary Ion Mass Spectrometry
TAMU	Texas A&M University

TG	Thermogravimetry
UPS	Ultraviolet photoelectron spectroscopy
VVER	Vodo-vodnyj energetičeskyj reaktor
XPS	X-ray Photoelectron Spectroscopy
XRD	X-Ray Diffraction
Zry-2	Zircaloy-2
Zry-4	Zircaloy-4